UNIVERSITY OF CAGLIARI

PHD DEGREE IN
Electronic and Computer Engineering
Cycle XXXII
IND-IND/32

Design of systems and components for high-speed electric propulsion systems

Author: Andrea FLORIS

PhD Course Coordinator: Prof. Alessandro Giua
Supervisor: Prof. Alfonso Damiano
Co-Supervisor: Dr. Alessandro Serpi

Academic Year 2018 – 2019

Abstract

This PhD dissertation presents the modelling and design of a novel High Speed (HS) Electric Propulsion System (EPS) for automotive application. In particular, Chapter I presents a comparison among different EPS configurations, which are designed by combining different Permanent Magnet Synchronous Machines (PMSMs) with the corresponding most suitable transmission system; this is done in order to investigate the competitiveness of HS-EPS for automotive applications.

Subsequently, the design of a novel ferrite-based HS-PMSM suitable for automotive application is presented in Chapter II. The design has been carried out through a novel multi-parameter analytical design procedure, which has been developed with the aim of achieving a preliminary machine design that considers both design targets and constraints. This preliminary design has been then validated through accurate and extensive finite element analyses, which regard both mechanical and electromagnetic performances.

In order to guarantee appropriate coupling between the designed HS-PMSM and vehicle wheels, the design and optimization of a novel coaxial Magnetic Gear Transmission (MaGT) is presented in Chapter III. In particular, a single-stage MaGT is designed at first in accordance with mechanical and magnetic analytical models. However, as far as a very high gear ratio is required (more than 20), the design of a double-stage MaGT has been carried out, which addresses some of the issues arising from the single-stage solution. A comparison in terms of performances and sizes between the two designed MaGTs is thus presented and discussed: the results obtained through the analytical models are validated by means of accurate finite element analyses. Subsequently, a further optimization of the double-stage MaGT has been carried out, which aims at reducing the harmonic content of the magnetic flux density. A comparative study between the two double stage MaGTs is presented and discussed, especially with reference to core losses and temperature distribution, highlighting the improved performances achieved by the optimized configuration.

Outline

Introduction

The increasing number of Internal Combustion Engine (ICE) vehicle is causing issues concerning environment and fossil fuel resources. In order to solve these problems, rigorous standards on vehicle emission and efficiency have been imposed. One of the most promising solutions is certainly the hybridization of the ICE power train, which could significantly increase the efficiency of the vehicles. This solution is represented by Hybrid Electric Vehicles (HEVs), which are in fact dual-powered vehicles: they are equipped with both an electric machine and a combustion engine and the former usually allows ICE to operate at maximum efficiency. There are multiple hybrid power-train topologies designed for these types of vehicles, each of which present inherent advantages and drawbacks. Alternatively to HEV, another promising solutions for the upcoming future is the development of cleaner and more efficient cars, among which full Electric Vehicles (EVs) [1].

The most important component of an EV is the Electric Propulsion System (EPS), which is made up mainly of an Energy Storage System (ESS), an electrical drive and a Transmission System (TS). Focusing on the ESS, electrochemical batteries are the most popular solutions, especially those based on Lithium technologies. Regarding the electrical drive, different Electrical Motors (EMs) are widely employed in commercial EVs, namely Permanent Magnet Synchronous Machines (PMSMs) and induction machines [2]. Whereas different TSs can be employed, as revealed by the technical literature [4]–[6]

, whose choice may affect the overall EPS efficiency significantly [6]. Among the different kinds of mechanical gear transmission systems usually employed, Single-Gear Transmission (SGT) is the most used solution due to its simple configuration. Furthermore, it is well suited for electrical drives characterized by wide Constant-Power Speed Region (CPSR) [7]. Alternatively, Multi-Gear Transmission (MuGT) can be employed, which, however, entails higher weights, volumes and costs. Another choice consists of Continuously Variable Transmission (CVT), which has been used successfully in automotive applications. However, CVT is generally characterized by low efficiency at low speed and increased system complexity compared to the other solutions previously mentioned [8].

A very promising solution for future EVs is represented by High-Speed EPS (HS-EPS) characterized by a High-Speed Electrical Machine (HS-EM) coupled with a Magnetic Gear Transmission (MaGT), which has been presented recently in the literature [9], [10]. Regarding HS-EMs, they have been used for a long time due to their numerous advantages, among which high power density and efficiency, reduced size, weights and overall costs [11], [12]. However, the need of reducing the very high-speed values of HS-EM for matching those required by vehicle wheels represent a critical task: in this regard, an MaGT system presents gear ratios and efficiency higher than conventional mechanical transmission systems. For these reasons, the integrated design of HS-EM with MaGT could enables compactness and lightness of the whole EPS [13].

In this scenario, this PhD dissertation presents the modelling and design of a novel HS-EPS for automotive application. In particular, Chapter I presents a comparison among different EPS configurations, designed by combining different PMSMs with the corresponding most suitable TSs [14]; this is done in order to investigate the competitiveness of HS-EPS for automotive applications. All the EPS solutions there considered have been tested by means of a simulation study, which is performed in MATLAB-Simulink. Particularly, an efficiency assessment has been carried out referring to three driving cycles in order to highlight the most suitable EPS configuration over different driving conditions.

Subsequently, in light of the results obtained, the design of a novel ferrite-based HS-PMSM suitable for automotive application is presented in Chapter II [15]. The design has been carried out through a novel multi-parameter analytical design procedure, which has been developed with the aim of achieving a preliminary machine design that takes into account both design targets and constraints; the former have been set in accordance with application requirements, whereas operating constraints are related mainly to high-speed operation and PM demagnetization issues. The proposed design approach has been validated through extensive simulation studies, which have been performed by means of Finite Element Analyses (FEAs) that regard both mechanical and electromagnetic aspects.

Subsequently, in order to guarantee appropriate coupling between the designed HS-PMSM and vehicle wheels, the design and optimization of a novel coaxial MaGT suitable for this specific application is presented in Chapter III. In particular, a single-stage MaGT is designed at first, by using an optimization function that minimizes the MaGT active volume in accordance with its mechanical and magnetic models. However, as far as a very high gear ratio is required (more than 1:20), MaGT may be still inadequate, even by resorting to coaxial configuration. This is because the maximum MaGT input torque decreases as the gear ratio increases [16]. Therefore, the design of a double-stage MaGT has been carried out, which addresses some of the issues arising from the single-stage solution. In a double-stage coaxial MaGT, two coaxial MaGT are mounted coaxially so that the external rotor of the inner MaGT is also the internal rotor of the outer MaGT. This configuration enables a compact system, by limiting the gear ratio of each stage and, thus, increasing the input torque and reducing the overall volume. A comparison in terms of performances and dimensions between the two designed MaGTs is thus presented and discussed; in particular, the results obtained through the analytical models are validated by means of accurate finite element analyses using the Solidworks and FEMM software. Then, a further optimization on the double-stage MaGT has been carried out, which aims at reducing the harmonic content of the magnetic flux density. In this regard, a detailed analysis of the magnetic flux density distribution has been carried out, whose outcomes are used to optimize the double-stage MaGT configuration previously designed. A comparison study between the two different MaGTs configuration is thus presented and discussed; this regards mainly core losses and temperature distribution in each part of the MaGT, which are evaluated by means of finite element analysis (FEMM software). The comparison reveals the effectiveness of the optimized configuration.

I Electric Propulsion System

I.1 EPS overview

A schematic representation of an Electric Propulsion System (EPS) is shown in Figure I.1. It is supplied by an Energy Storage System (ESS), which has to deliver a proper amount of energy in order to guarantee an adequate vehicle driving range. The ESS is interfaced with the Electric Motor (EM) through a number of power electronic converters. The EM transmitted the mechanical torque to the traction wheels by means of a Transmission System (TS), which has to adapt the EM rotational speed to the wheel speed. Referring to the vehicle traction characteristics depicted in Figure I.2, the EPS has to be designed in accordance with vehicle target performances, among which maximum acceleration, speed and gradeability [1]. Particularly, at low vehicle speeds, the traction effort is generally upper bounded by tyre-ground contact issues. As the speed increases, power increases until the vehicle reaches its base speed V_b. Above V_b, traction effort decreases, while propulsion power is kept constant and equal to the rated one. Consequently, the maximum speed V_{max} is reached when the traction effort equals the overall resistance force, as highlighted in Figure I.2.

It is worth noting that V_b is generally quite lower than V_{max}, entailing wide Constant-Power Speed Range (CPSR). Therefore, suitable combinations of EM and TS must be chosen in order to match both traction effort and power requirements.

Figure I.1 – Schematic representation of an electric propulsion system.

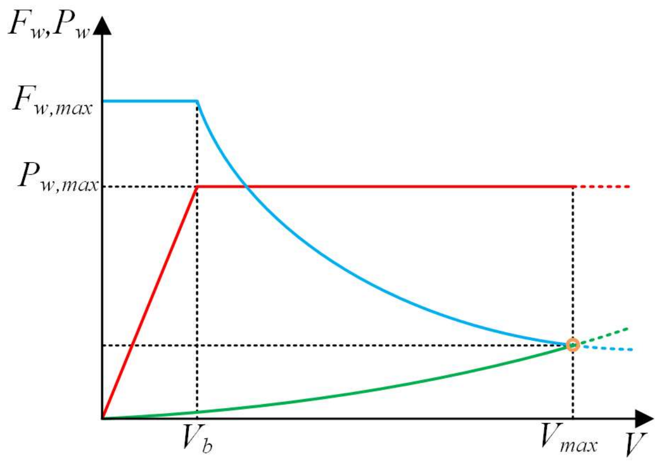

Figure I.2 - Vehicle traction effort (cyan) and power (red) characteristics with vehicle speed, together with the overall resistance force (green).

Focusing on the EM, two solutions can be employed for satisfying the propulsion requirements: the first one consists of choosing an EM with a wide CPSR in order to match vehicle traction characteristics to the maximum extent. This solution benefits from simplified and highly efficient TS, i.e. fixed-gear, but it generally introduces several issues regarding EM design, control and efficiency. Alternatively, EM with narrow CPSR can be used, which can generally operate at higher efficiency. However, this solution requires more complex and lower efficient TS [17].

Therefore, based on the previous considerations, different TS can be chosen in accordance with EM inherent features. Consequently, a brief review of TS used in EPS is presented in the following section. Subsequently, four different EPSs characterized by different EM and/or TS have been designed and tested in order to assess their performances over different driving cycles.

I.2 Transmission systems

I.2.1 Single-gear transmission

The Single-Gear Transmission (SGT) is the simplest and most frequently used TS for Electric Vehicles (EVs). It presents a fixed gear ratio, which is defined as:

$$\tau = \frac{\omega_m}{\omega_w} = \frac{\omega_m r_w}{V} \tag{III.1}$$

in which ω_m and ω_w are the EM and wheel rotational speed respectively, V is the vehicle speed and r_w is the wheel radius. Referring to (III.1), τ can be set in accordance with maximum traction effort and/or maximum speed. Vehicle and motor speeds are proportional to each other, as shown in Figure I.3. Hence, since the gear ratio is constant, the traction characteristic has to match that of the EM; for this reason, the employment of an SGT generally occurs jointly with EM with wide CPSR.

I.2.2 Multi-gear transmission

The Multi-Gear Transmission (MuGT) allows the discrete variation of the gear ratio depending on the vehicle speed. MuGT is made up of several gears, whose selection occurs manually or automatically in accordance with propulsion requirements. Particularly, the first gear ratio is chosen as:

$$\tau_1 = \frac{\omega_{m.max} r_w}{V_{1,max}} \tag{III.2}$$

where $V_{1,max}$ is the maximum vehicle speed for the first gear and $\omega_{m,max}$ is the maximum EM speed. The other gear ratios should be defined so that the EM always operates within a given speed range, i.e. between $\omega_{m,min}$ and $\omega_{m,max}$, as shown in Figure I.4. Particularly, $\omega_{m,min}$ is generally chosen higher than the EM rated speed in order to ensure a wide CPSR of the vehicle. Once the EM speed range is set, the gear ratios of MuGT can be defined by using the following relationship:

$$\tau_k = \tau_{k-1} \frac{\omega_{m,\min}}{\omega_{m,\max}} = \tau_1 \left(\frac{\omega_{m,min}}{\omega_{m,\mathrm{m}max}} \right)^{k-1} \quad , \ k = 1,...,n \tag{III.3}$$

in which n is the number of the gears.

I.2.3 Continuously variable transmission

The Continuously Variable Transmission (CVT) is an automatic TS that is able to change the gear ratio seamlessly within a given range [τ_{min}, τ_{max}]. As a result, the EM operates at a constant speed when the EV is within a defined speed range [$V_{v,i}$,$V_{v,f}$], as shown in Figure I.5.

Focusing on the design procedure, τ_{min} and τ_{max} can be determined in accordance with (III.2) and (III.3) as:

$$\tau_{\min} = \frac{\omega_{m,v}\, r_w}{V_{v,i}} \;,\; \tau_{\max} = \frac{\omega_{m,max}\, r_w}{V_{max}} \tag{III.4}$$

where $\omega_{m,v}$ is the EM constant speed value, which is chosen in accordance with the EM characteristic in order to maximize its efficiency. The main advantage of CVT consists of maximizing EM efficiency over a given vehicle speed range. However, this TS is rarely used for EV due to its complexity and low efficiency.

I.2.4 Transmission systems for high-speed applications

When high gear ratios are required, special TSs are needed. Although this issue can be addressed by series-connecting a number of conventional systems that guarantee a subsequent reduction of the rotational speed, this solution increases the TS losses and the power train volume and weight. Alternatively, in order to limit the TS overall volume, planetary gear transmissions can be adopted, which enable higher gear ratios compared to conventional solutions. However, planetary gears exhibit low efficiency when high gear ratio is concerned.

A very promising solution for EPS that employs high-speed EM, especially if High-Speed Permanent Magnet Synchronous Machine (HS-PMSM) is adopted, is represented by Magnetic-Gear Transmission (MaGT). It is a contactless TS, characterized by very high efficiency, high reliability and low maintenance. MaGT is generally made up of a number of magnetic rings that are properly coupled in order to achieve the desired gear ratio, which can be calculated with the same procedure employed for the SGT. However, in this configuration, very high gear ratio can be achieved, making MaGT. Moreover, the MaGT may be integrated within the HS-PMSM, enabling the design of compact and light EPS (the so-called geared motors).

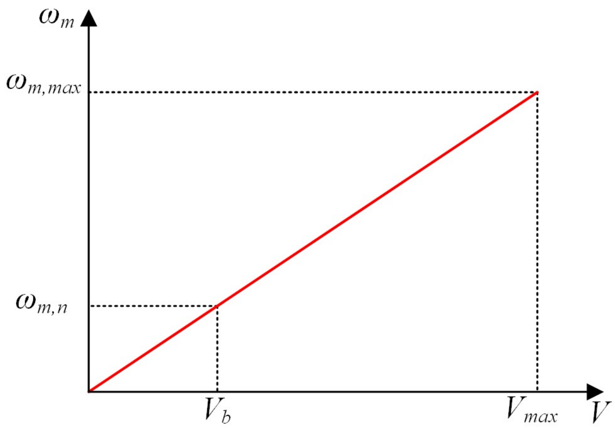

Figure I.3 - Motor rotational speed evolution with vehicle speed for a SGT and MaGT.

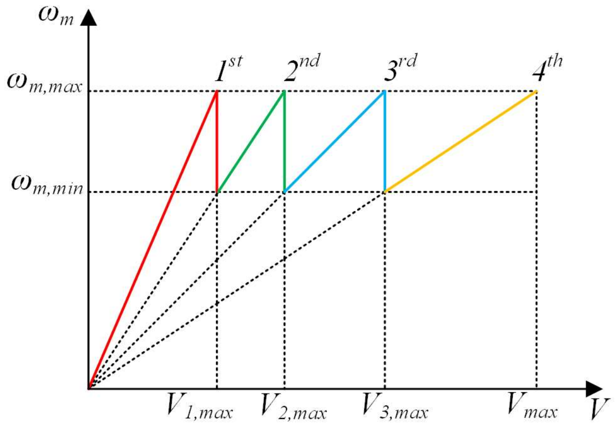

Figure I.4 - Motor rotational speed evolution with vehicle speed for a MuGT.

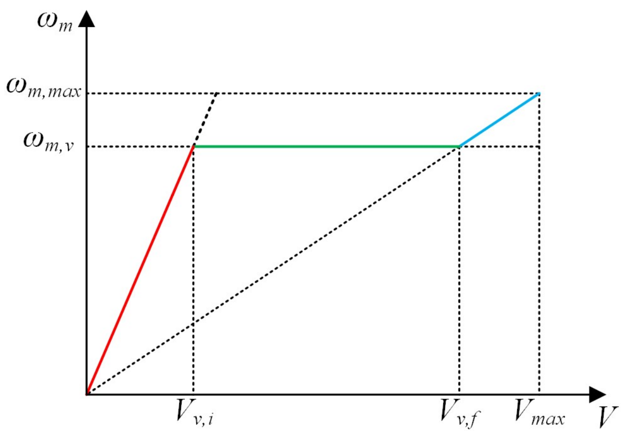

Figure I.5 - Motor rotational speed evolution with vehicle speed for a CVT.

I.3 Simulation setup

In order to investigate the performances of different EM and/or TS solutions, different EPS configurations have been considered. Subsequently, the comparison among the EPS configurations has been carried out by numerical simulations in the MATLAB-Simulink environment. Particularly, the SimDriveline Library has been employed for modelling each EPS. The overall simulation set-up is depicted in Figure I.6 and consists of three main blocks, namely the Driver, the EPS and the Vehicle. Each of these blocks have been modelled as detailed in the following subsections.

I.3.1 Driver modelling

The driver has been modelled by means of a driving cycle and a speed controller. In this regard, three different driving cycles have been considered, which are shown in Figure I.7. The NEDC represents the standard driving cycle used for evaluating vehicle energy consumption in Europe, whereas ArtUrban and ArtRoad cycles reproduce more accurately the real driving conditions characterized by rapid accelerations and braking.

The reference speed of the vehicle imposed by each driving cycle is tracked by means of a speed controller, which provides the reference torque to the EPS through a Proportional-Integral (PI) regulator, which processes the speed error appropriately.

I.3.2 EPS modelling

The EPS has been modelled in accordance with different EM and TS solutions, which have been defined by considering the vehicle main parameters summarized in Table I.1.

Focusing on the EM at first, three different PMSMs have been considered, whose rated values are reported in Table I.2. All the PMSMs are characterized by the same rated power, but different operating speed ranges. Particularly, EM1 [2] and EM2 [8] are relatively Low-Speed PMSMs (LS-PMSMs) and they present wide and narrow CPSR respectively. Differently, EM3 [10] is a HS-PMSM characterized by a wide CPRS.

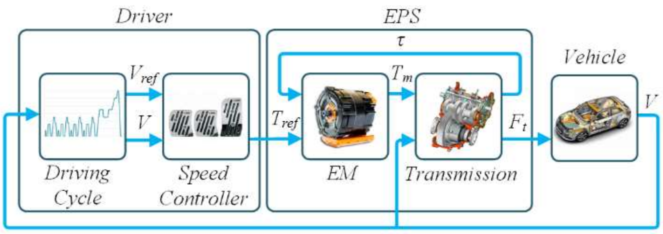

Figure I.6 - Simulation setup.

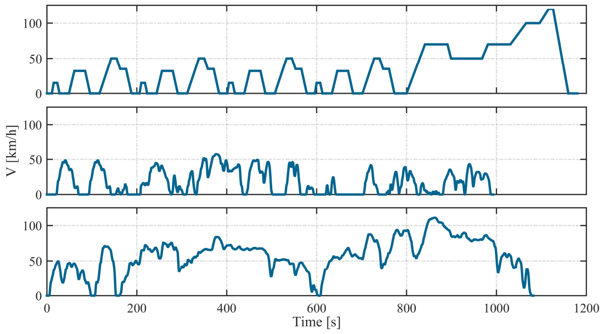

Figure I.7 - Driving cycles: NEDC (top), ArtUrban (middle) and ArtRoad (bottom).

Table I.1 - Vehicle main parameters

Parameter	***Symbol***	***Unit***	***Value***
Base speed	V_b	km/h	36.5
Design maximum speed	V_{max}	km/h	125
Maximum gradeability (@ V_b)	α_{max}		30
Vehicle mass	m_v	kg	1130
Frontal area	A_f	m^2	2.06
Drag coefficient	C_d	-	0.29
Friction coefficient	C_{roll}	-	0.006
Wheel radius	r_w	m	0.28

Table I.2 - PMSM rated and maximum values [2], [8], [10]

	Symbol	***Unit***	***EM1 [2]***	***EM2 [8]***	***EM3 [10]***
Rated Power	P_n	kW	40.3		
Rated Torque	T_n	Nm	110	110	9.5
Rated Speed	$\omega_{m,n}$	krpm	3.5	3.5	40.5
Maximum Speed	$\omega_{m,max}$	krpm	12	5	159

Table I.3 - Transmission system parameters

Parameter	***Symbol***	***Unit***	***Value***
TS1 (SGT)			
Gear ratio	τ	-	10.08
Actual maximum speed	$V_{max,case1}$	km/h	125
TS2a (4-Gear MuGT)			
1st gear ratio	τ_1	-	10.08
2nd gear ratio	τ_2	-	7.05
3rd gear ratio	τ_3	-	4.93
4th gear ratio	τ_4	-	3.45
Actual maximum speed	$V_{max,case2}$	km/h	151.8
TS2b (CVT)			
Maximum gear ratio	τ_{min}	-	10.08
Minimum gear ratio	τ_{max}	-	3.45
Constant motor speed	ω_v	rpm	3600
Actual maximum speed	$V_{max,case3}$	km/h	151.8
TS3 (MaGT + SGT)			
MaGT ratio	τ_{MaGT}	-	26
SGT ratio	τ_{SGT}	-	4.5
MaGT maximum efficiency	η_{MaGT}	%	98
Actual maximum speed	$V_{max,case4}$	km/h	143

Regarding the TS, different cases have been considered in accordance with the inherent characteristics of each EM, as pointed out in Table I.3. In particular, SGT is the most suitable solution for EM1 due to its relatively low operating speed range and wide CPSR. Whereas two different solutions are proposed for EM2 (MuGT and CVT) due to its much narrower CPSR compared to EM1. Furthermore, an MaGT combined with an SGT is suggested for EM3 due to its very high operating speed range. The parameters in Table I.3 have been calculated considering the equations reported in (I.2) in accordance with desired maximum gradeability reported in Table I.1.

Table I.4 – EPS configuration summary

Case	*Electric Motor (EM)*	*Transmission System (TS)*
1	EM1 (LS-PMSM, wide CPSR)	TS1 (SGT)
2a	EM2 (LS-PMSM, narrow CPSR)	TS2a (4-Gear MuGT)
2b	EM2 (LS-PMSM, narrow CPSR)	TS2b (CVT)
3	EM1 (HS-PMSM, wide CPSR)	TS3 (MaGT + SGT)

Table I.5 - Transmission system coefficients

Parameter	*SGT*	*MuGT*	*CVT*	*MaGT+SGT*
A_{H2}	0	0	0.0935	0
A_{H1}	0	0	-0.1871	0
A_{H0}	1	1	1.0599	1
A_{L2}	0	0	0.0068	0
A_{L1}	0	0	-0.0135	0
A_{L0}	1	1	0.9731	1
B	50	20	20	50
$\eta_{t,max}$	0.99	0.98	0.97	0.97

Therefore, four EPS configurations have been considered, as summarized in Table I.4. Each specific EPS configuration has been characterized by its own overall efficiency, which can be determined as:

$$\eta_{EPS} = \eta_b \, \eta_c \, \eta_m \, \eta_t \qquad \text{(III.5)}$$

where η_b, η_c, η_m and η_t are the efficiencies of ESS, power electronic converters, EM and TS respectively. Both η_b and η_c in (III.5) are assumed constant at 0.9, which should represent a reasonable and precautionary estimation. Furthermore, η_m is determined in accordance with suitable look-up tables, which have been computed based on the Maximum Torque Per Ampere control strategy (MTPA).

Regarding η_t, a number of mathematical models have been proposed in the literature [16]–[18]
, which are derived from extensive experimental analysis mainly. These models state that η_t depends on input torque significantly, and it is almost unaffected by rotational speed variations. Consequently, by neglecting the speed contribution, η_t

can be expressed simply as a function of the input torque. Therefore, in accordance with the model proposed in [8], the following expression has been considered:

$$\eta_t = k_n\left(\tau\right)\cdot k_T\left(T_m\right)\cdot\eta_{t,max} \tag{III.6}$$

where $\eta_{t,max}$ is the maximum efficiency of the TS, whereas k_n and k_T are the gear ratio and the torque coefficients, which are further expressed as:

$$k_n(\tau) = \begin{cases} A_{H2}\tau^2 + A_{H1}\tau + A_{H0} & , \ \tau < 1 \\ A_{L2}\tau^2 + A_{L1}\tau + A_{L0} & , \ \tau \geq 1 \end{cases} \tag{III.7}$$

$$k_T(T_m) = 1 - e^{-B\frac{T_m}{T_{n,m}}} \tag{III.8}$$

in which A_{Hi}, A_{Li} and B are TS coefficients that depend on the transmission topology and that are determined experimentally, whose values are reported in Table I.5. In this context, it is worth noting that the efficiency of MaGT can be assumed constant within the overall EM speed and torque ranges, as pointed out in [10].

As a result, the energy consumption over each driving cycle can be computed as:

$$\Delta E_b = \int_{traction} \frac{P_w}{\eta_{EPS}}\,dt + \int_{braking} \zeta\eta_{EPS}P_w\,dt \tag{III.9}$$

in which P_w is the mechanical power at the vehicle wheels, whereas ζ is the share of the braking power available for regenerative braking, considering a hybrid braking system, in which a mechanical and an electric braking system coexist.

I.3.3 Vehicle modelling

The vehicle dynamics concerns a complex system of equations, which have to take into account all the forces acting on the vehicle during its motion [21]. However, for energy analysis purposes, reference is generally made to a relatively simple case, namely the vehicle that climbs a straight road shown in Figure I.8. Consequently, the force balance equation can be expressed as:

$$m\delta\frac{dV}{dt} = F_t - F_r \tag{III.10}$$

in which m is the vehicle mass, δ is the mass factor and V is the vehicle speed. Whereas F_t and F_r are the traction force and the total resistance force respectively. The latter consists of several components, as highlighted in the following expression:

$$F_r = F_w + F_g + F_{roll} \tag{III.11}$$

where F_w is the aerodynamic drag, which accounts for the air resistance against the motion of the vehicle. This contribution to F_r can be thus expressed as:

$$F_w = \frac{1}{2}\rho_a A_f C_d \left(V + V_w\right)^2 \tag{III.12}$$

in which ρ_a is the air mass density, A_f is the equivalent front area of the vehicle and V_w is the wind speed. In addition, C_d is the aerodynamic drag coefficient, which depends on the vehicle shape. Still referring to (III.11), F_g and F_{roll} are the grading and rolling resistances respectively, which depend on vehicle mass m_v and the slope θ as:

$$F_g = m_v g \sin\theta \tag{III.13}$$

$$F_{roll} = mg\, C_{roll} \cos\theta \tag{III.14}$$

where g is the gravitational acceleration, while C_{roll} is the rolling resistance coefficient already shown in Table I.1. Therefore, it is worth underlining that simulations do not account for slope and wind speed, which have been set both equal to zero.

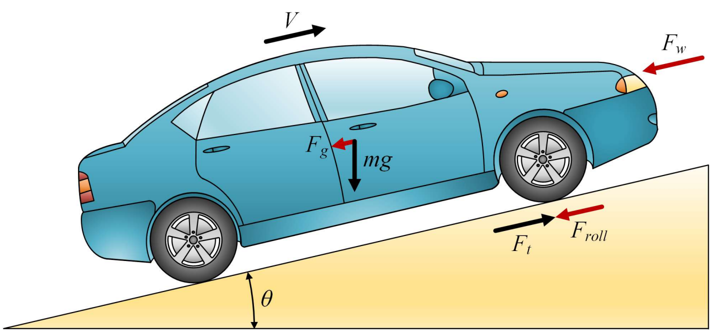

Figure I.8 - Forces acting on a vehicle climbing a straight road.

I.4 Simulation results

Simulation results achieved for each of the EPS configuration summarized in Table I.4 are presented from Figure I.9 to Figure I.11, which show the operating points of each EM on the (ω_m,T_m) plane over each driving cycle for all the cases considered for simulations. Furthermore, the overall energy consumptions are resumed in Table I.6, while the EPS overall losses are summarized in Table I.7.

Focusing on the NEDC cycle at first, it can be seen that the best performances in terms of energy consumption are achieved in *Case 3* due to the optimal trade-off between ESS+EM and TS losses. Particularly, although lower TS losses is achieved in *Case 1*, ESS+EM losses are much more relevant than in *Case 3* due to the EM low-speed ranges. Very high TS losses are achieved in *Case 2a* and, especially, in *Case 2b*, which overcome the advantages related to higher ESS+EM efficiency.

Different considerations have to be made referring to the ArtUrban driving cycle, which is characterized by a relatively low energy consumption due to its short duration and driving path. In particular, the best performances are achieved in *Case 2a* because the operating points spread within a wide torque-speed region, which corresponds to high EM2 efficiency values. Consequently, since CVT presents higher losses than MuGT, *Case 2a* prevails over *Case 2b*. The latter is disadvantageous also compared to both *Case 1* and *Case 3*.

Considerations similar to those reported for the ArtUrban driving cycle can be made also for the ArtRoad driving cycle, although some differences occur. In particular, *Case 2a* assures the best performances, but *Case 2b* slightly prevails over *Case 1*. The latter presents the worst performances due to the very poor efficiency of EM1 during these driving conditions.

In conclusion, it can be stated that *Case 2a* (LS-PMSM with narrow CPSR and MuGT) is the most suitable solution for both ArtUrban and ArtRoad, and it is also quite competitive for NEDC. Whereas *Case 2b* (LS-PMSM with narrow CPSR and CVT) seems poorly competitive over any driving condition, mainly due to the very low CVT efficiency.

Furthermore, it is worthy of note that *Case 3* (HS-PMSM with wide CPSR coupled with MaGT and SGT) is also quite competitive, especially if compared with *Case 1* (LS-PMSM with wide CPSR and SGT). Its competitiveness could be even higher if weight reduction related to the employment of HS-PMSM is considered, making this solution a valid alternative to *Case 2a* for EPS of electric vehicles.

Table I.6 - Overall energy consumption

Cycle		***Case 1 (Wh)***	***Case 1 (pu)***	***Case 2a (pu)***	***Case 2b (pu)***	***Case 3 (pu)***
NEDC	*Overall energy*	1247	1.00	1.00	1.02	0.96
	Total Losses	260	1.00	0.97	1.08	0.85
	Cycle Efficiency	79%		80%	78%	81%
ArtUrban	*Overall energy*	750	1.00	0.98	1.04	0.99
	Total Losses	94	1.00	0.85	1.36	0.94
	Cycle Efficiency	87%		89%	83%	88%
ArtRoad	*Overall energy*	2125	1.00	0.95	0.98	0.97
	Total Losses	350	1.00	0.69	0.89	0.84
	Cycle Efficiency	84%		88%	85%	86%

a)

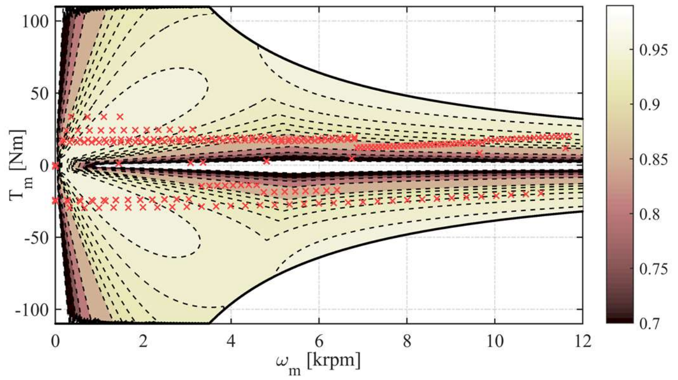

b)

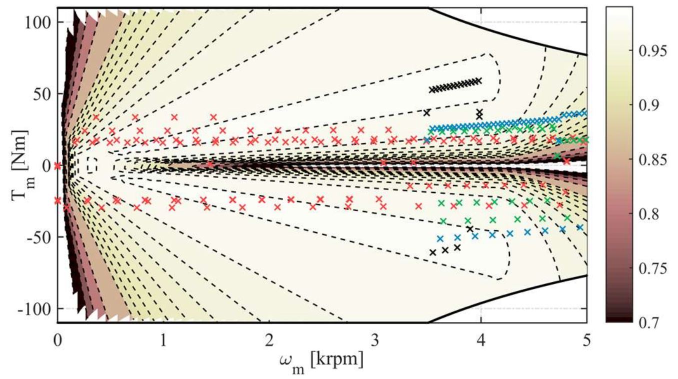

c)

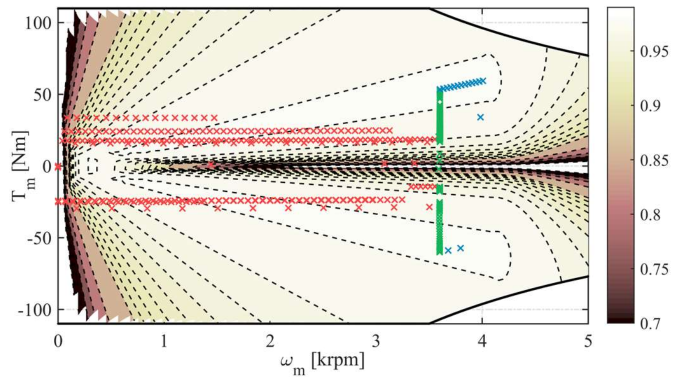

d)

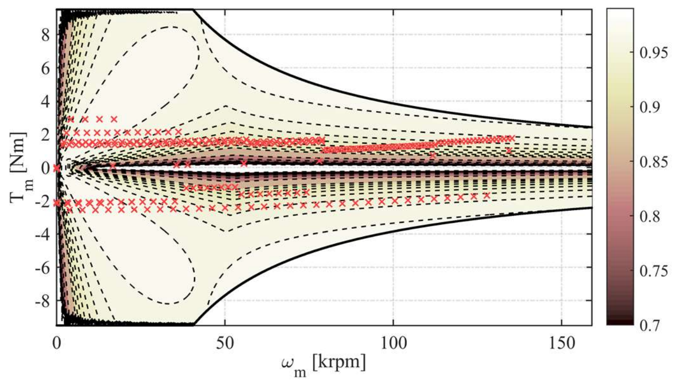

Figure I.9 - Operating points achieved over NEDC driving cycle, together with the EM efficiency map (colormap): *a) Case 1*, *b) Case 2a*: 1st (red), 2nd (green), 3rd (blu), 4th (black) gear, *c) Case 2b*: τ_{min} (red), τ (green) and τ_{max} (blu), *d) Case 3*.

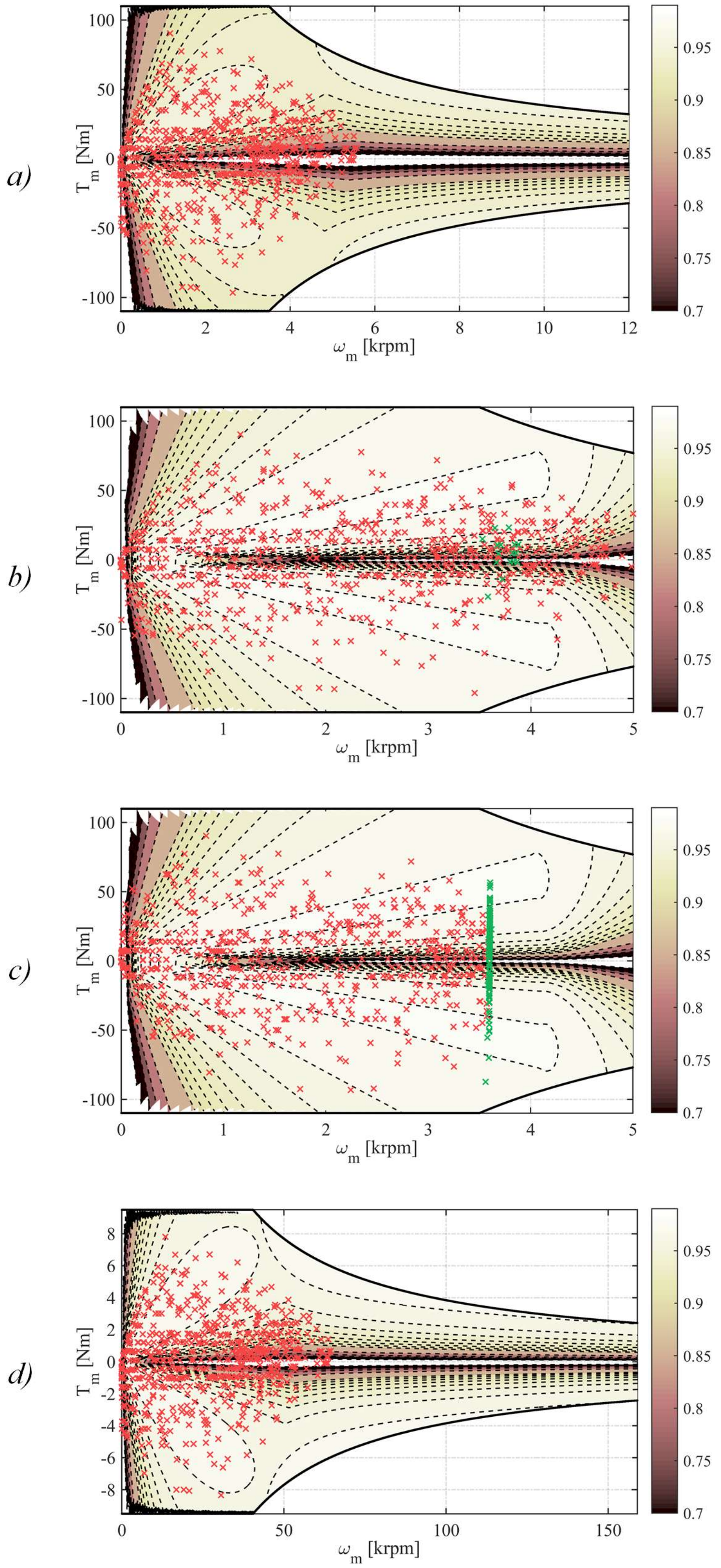

Figure I.10 - Operating points achieved over ArtUrban driving cycle, together with the EM efficiency map (colormap): *a) Case 1*, *b) Case 2a*: 1st (red), 2nd (green) gear, *c) Case 2b*: τ_{min} (red), τ (green), *d) Case 3*.

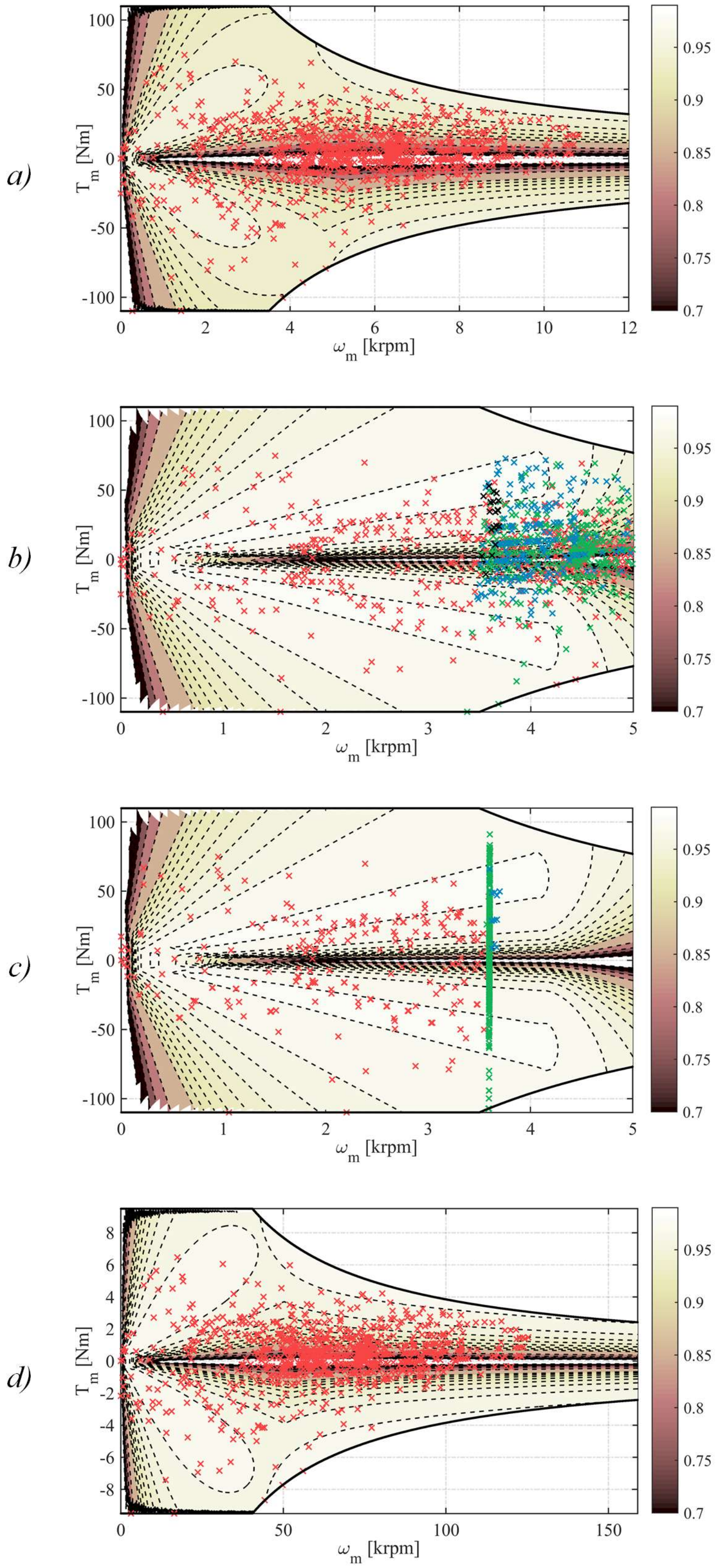

Figure I.11 - Operating points achieved over ArtRoad driving cycle, together with the EM efficiency map (colormap): *a) Case 1*, *b) Case 2a*: 1st (red), 2nd (green), 3rd (blu), 4th (black) gear, *c) Case 2b*: τ_{min} (red), τ (green) and τ_{max} (blu), *d) Case 3*

Table I.7 - EPS losses

Cycle & Case		***ESS+EM losses [Wh]***	***TS Losses [Wh]***	***Total losses [Wh]***
NEDC	*1*	196 (75.3 %)	64 (24.7 %)	260
	2a	128 (50.8 %)	124 (49.2 %)	252
	2b	67 (23.8 %)	214 (76.2 %)	281
	3	139 (62.5 %)	83 (37.5 %)	222
ArtUrban	*1*	75 (79.9 %)	19 (20.1 %)	94
	2a	36 (45.5 %)	44 (54.5 %)	80
	2b	31 (24.2 %)	97 (75.8 %)	128
	3	54 (61.4 %)	34 (38.6 %)	88
ArtRoad	*1*	281 (80.3 %)	69 (19.7 %)	350
	2a	139 (57.2 %)	104 (42.8 %)	243
	2b	88 (28.3 %)	223 (71.7 %)	311
	3	191 64.7 %	104 (35.3 %)	295

.

II High-Speed Electrical Machine

High-Speed Electrical Machines (HS-EMs) are currently employed in a wide range of applications, such as dental drills and medical surgery tools, flywheel energy storage systems, gas and oil compressors, spindles and power generation [20]–[22]. Several kinds of EMs can be considered for HS-EMs depending on the specific application, e.g. induction machines, Permanent Magnet Synchronous Machines (PMSMs) and switched reluctance machines. Among these different solutions, High-Speed PMSMs (HS-PMSMs) are very popular: they are characterized by rated speed from 10 krpm to over 200 krpm and rated power from few watts to hundreds of kilowatts, although they are employed for low-power applications mostly [23]–[26]. Furthermore, novel materials and recent improvements in power electronics and control systems are enabling a further increase of HS-PMSM performances and operating speed range [29], making them suitable also for automotive applications. Equation Chapter (Next) Section 1.

The use of HS-PMSMs in automotive applications presents several challenges that must be taken into account properly. One of these is surely the significant mechanical forces acting on the rotor due to the high rotational speed, particularly the high tensile stress due to rotation reduces the contact pressure between PMs and the rotor structure. In this regard, a surface-mounted PM configuration has been taken into account, since it enables high peripheral speeds [28]–[30]. Hence, PMs, which are usually glued to the rotor yoke in surface-mounted configurations, are contained also by mechanical sleeves [33]: these are made up of high-strength materials, such as metallic alloys or carbon fibres, in order to guarantee PMs retention, especially at high-speed operation [34].

Another challenge of using HS-PMSM for automotive applications consists of PM material: in this regard, rare-earth PMs are typically used due to their high-energy density, which limits rotor size and, thus, peripheral speed. However, there is a great concern about using rare-earth PMs due to material availability and price fluctuation issues. Consequently, the use of less rare-earth or no rare-earth PMs (ferrite PMs) is increasingly taking off, especially in a growing sector as automotive. In this regard, it is worth noting that the employment of ferrite PMs does not imply reduced HS-PMSM performances unavoidably, and it enables significant cost saving [35], [36]. However, ferrite-based HS-PMSMs still suffer from relatively low torque and power density, as well as from some critical issues related to weak residual magnetism and low coercive force.

Based on the previous considerations, the design of a HS-PMSM for a light-duty electric vehicle is presented in this chapter [1]. Therefore, mechanical and electromagnetic modelling has been considered at first, based on which the design of the HS-PMSM has been carried out by complying with both application targets and mechanical and electromagnetic constraints.

II.1 HS-PMSM modelling

The mechanical modelling of the HS-PMSM rotor is fundamental because the mechanical stress related to rotational speed is not negligible in high-speed applications, requiring the definition of appropriate mechanical constraints. These affect the HS-PMSM rotor geometry, especially the PM configuration. In this regard, PM materials generally present better mechanical properties to compression stress rather than to tensile stress [34]. Therefore, for an inner rotor HS-PMSM configuration, the surface-mounted PMs are enclosed by a mechanical sleeve in order to limit tensile stress and guarantee their retention, especially at high-speed operation [31], [37].

[1] The research activities presented in this chapter have been developed with Giuseppe Fois, a PhD student at the University of Cagliari from 2015 to 2018, who has already presented part of them in his PhD Thesis [14].

Electromagnetic modelling is also very important for HS-PMSMs, especially when ferrite PMs are concerned. This is because low residual magnetic flux density and coercive force make PM subject to potential demagnetization, which has to be avoided over any operating condition. For this purpose, the magnetic flux path has to be considered carefully, as well as the effects of stator current on the magnetic flux density distribution within PMs.

II.1.1 Mechanical model

The mechanical model of HS-PMSM has been developed referring to the rotor structure shown in Figure II.1. In particular, the rotor is made up of an inner shaft (*sh*), a rotor yoke (*yr*), a layer of ferrite PMs (*m*) and an outer sleeve (*s*); the latter is prestressed, i.e. the inner radius of the sleeve surrounding the PMs is smaller than the free outer radius of PMs due to mechanical pretension, because of the need of increasing mechanical retention of PMs.

In order to investigate mechanical stresses on HS-PMSM rotor, each rotor layer can be considered as a rotating cylinder. which represents the base geometric structure of the HS-PMSM rotor, in order to determine both radial σ_r and tangential σ_θ stresses acting on each rotor layer.

The mathematical formulation for the stress computation in a pressured rotating cylinder, based on the mechanical-elastic theory, is described in detail in Appendix (A), based on which both σ_r and σ_θ in each rotor layer can be expressed as:

$$\sigma_r(r) = c_1 r^{k-1} + c_2 r^{-k-1} - \frac{(3+\upsilon_\theta)\rho\omega^2 r^2}{9-k^2} - E_\theta\left(\frac{r(2\alpha_\theta - \alpha_r)t}{4-k^2} + \frac{(\alpha_\theta - \alpha_r)t_0}{1-k^2}\right) \quad \text{(IV.1)}$$

$$\begin{aligned}\sigma_\theta(r) = kc_1 r^{k-1} - kc_2 r^{-k-1} - \rho\omega^2 r^2\left(\frac{3(3+\upsilon_\theta)}{9-k^2} - 1\right) + \\ - E_\theta\left(\frac{2r(2\alpha_\theta - \alpha_r)t}{4-k^2} + \frac{(\alpha_\theta - \alpha_r)t_0}{1-k^2}\right)\end{aligned} \quad \text{(IV.2)}$$

where E_r and E_θ are the Young's modulus in radial and tangential direction of the cylinder material, υ_r and υ_θ are and Poisson's ratio in radial and tangential direction respectively, and α_r and α_θ are the thermal expansion coefficients in radial and tangential direction of the material. Moreover, c_1, c_2, t_o and t are constants which depend on the inner and outer cylinder pressure, on its rotational speed and temperature gradient. The expression of c_1, c_2, t_o and t are reported in the Appendix (A). Furthermore, k is defined as:

$$k = \sqrt{\frac{E_\theta}{E_r}}\ . \tag{IV.3}$$

Rearranging (IV.1) and (IV.2), referring to the different layers, the expressions of σ_r and σ_θ can be rewritten as:

$$\sigma_x^{(y)}(r) = \sigma_{x,p}^{(y)} + \sigma_{x,\omega}^{(y)} + \sigma_{x,T}^{(y)} \quad , \quad x \in \{r, \theta\} \ , \quad \mathrm{y} \in \{yr, m, s\} \tag{IV.4}$$

in which σ_r and σ_θ are function of the radial dimension and consist of three contributions mainly: $\sigma_{x,p}$ is due to the prestress procedure, $\sigma_{x,\omega}$ is caused by rotational motion and $\sigma_{x,T}$ is related to temperature gradient.

In order to determine $\sigma_r^{(y)}$ and $\sigma_\theta^{(y)}$ referring to the overall rotor structure, reference is made to Figure II.2, which highlights the main dimensions of the three rotor layers. In this regard, rotor shaft and back-iron have been considered as a single layer because their corresponding materials are very similar to each other from a mechanical point of view. Furthermore, the valuation of σ_r and σ_θ on each layer require the knowledge of the contact pressure exerted on it by the surrounding materials. Therefore, referring to Figure II.3, the following relationships can be imposed:

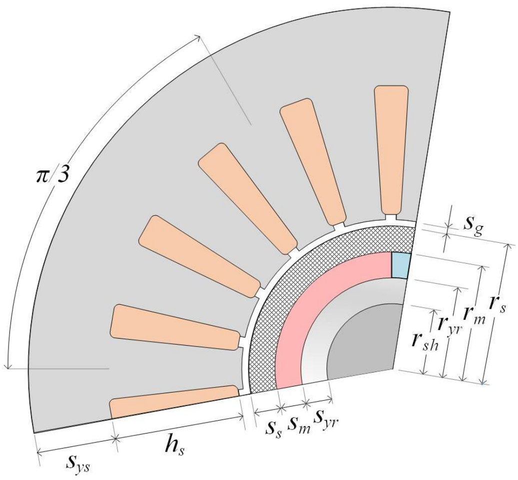

Figure II.1 - Cross section of the proposed machine geometry

$$\begin{cases} p_i^{(yr)} = 0 \\ p_o^{(yr)} = -p_i^{(m)} \end{cases}, \quad \begin{cases} p_i^{(s)} = -p_o^{(m)} \\ p_o^{(s)} = 0 \end{cases}. \tag{IV.5}$$

However, the PM contact pressures $p_i^{(m)}$ and $p_o^{(m)}$ cannot be determined from equilibrium equations since the problem is statically indeterminate. Consequently, the solution must be obtained starting from the radial displacement u_r, achieved by Hooke's law, expressed as:

$$u_r^{(y)} = \frac{r}{E_\theta^{(y)}} \left(\sigma_\theta^{(y)} - k\upsilon_r^{(y)}\sigma_r^{(y)} + E_\theta^{(y)}\alpha_\theta^{(y)}\Delta T^{(y)} \right), \qquad \mathrm{y} \in \{yr, m, s\} \tag{IV.6}$$

where ΔT is the difference between actual and reference temperatures in each rotor layer.

By imposing the radial deflection in the contact surfaces between the three cylinders shown in Figure II.2, the following equations are obtained:

$$\begin{aligned} &\left(u_r^{(s)} - u_r^{(m)} \right)\Big|_{r=r_m} = \delta \\ &\left(u_r^{(m)} - u_r^{(yr)} \right)\Big|_{r=r_{yr}} = 0 \end{aligned} \tag{IV.7}$$

in which δ is the radial interference, i.e. the difference between the outer radius of PM and the free inner radius of the sleeve, as pointed out previously and already shown in Figure II.2.

As a result, taking into account the (IV.5), the contact pressures on the PM layer ($p_i^{(m)}$ and $p_o^{(m)}$) can be computed by solving the linear system achieved by substituting (IV.4) in (IV.6) and consequently in (IV.7). Subsequently, the tangential and radial stresses σ_r and σ_θ for each layer can be achieved solving (IV.1) and (IV.2).

Mechanical modelling has to account not only for radial and tangential stress and contact pressure, but also for critical speeds in order to avoid resonance phenomena. In particular, a generic rotating shaft is characterized by several critical speeds, but only the first (minimum) critical speed ($\omega_{m,cr}$) is usually considered in the design process [29]. Therefore, the rotor first critical speed, which should not be reached in order to preserve HS-PMSM rotor integrity, can be estimated as [38]:

$$\omega_{m,cr} = \sqrt{\frac{g}{d_{st}}} \tag{IV.8}$$

in which g is gravity acceleration constant and d_{st} is the rotor static deflection, which depends on rotor layer geometry and material properties.

II.1.2 Electromagnetic model

The electromagnetic modelling has been developed by referring to the two-poles HS-PMSM configuration shown in Figure II.4. This consists of an inner rotor made up of four cylindrical layers, namely rotor shaft, back-iron, PM ring and sleeve. Whereas the outer stator consists of two layers, i.e. iron teeth and slots, which host a distributed three-phase winding, and the stator back-iron. The layer between stator and rotor is the airgap. Based on this configuration, the electromagnetic modelling can be carried out, as detailed in the following subsections.

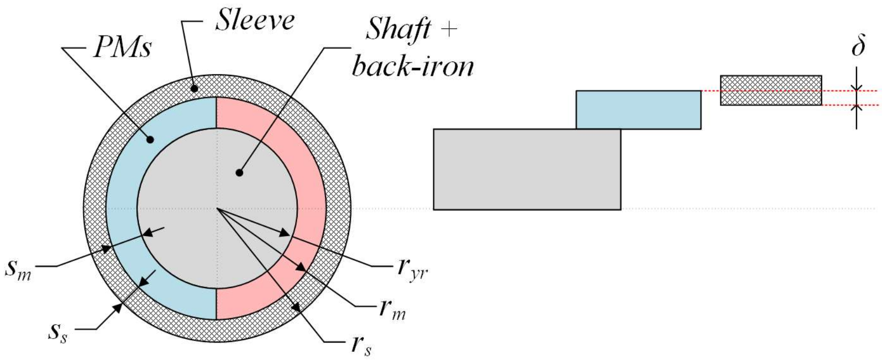

Figure II.2 - Cross section of the HS-PMSM rotor, in which δ denotes the radial interference between the PM ring and the sleeve.

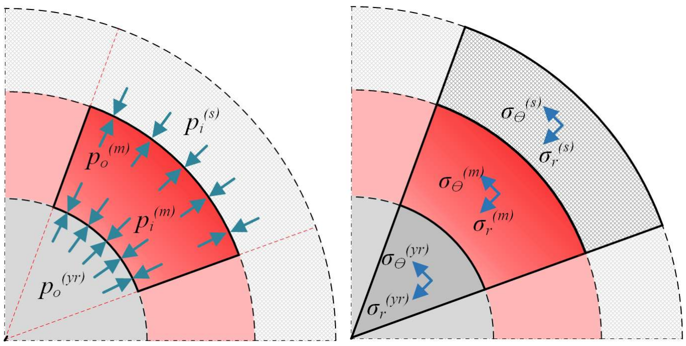

Figure II.3 – Pressure and stresses acting on some layers of the HS-PMSM rotor.

II.1.2.1 Magnetic model

Magnetic modelling of the HS-PMSM is based on the following assumptions:

- the magnetic flux density is characterized by radial component only;
- the drop of the magnetomotive force (*mmf*) over all the iron paths is negligible;
- sleeve acts as an additional airgap from an electromagnetic point of view;
- no magnetic saturation phenomenon occurs.

Hence, the application of the Ampère's Law to the main magnetic flux path depicted in Figure II.4 leads to:

$$2\int_{r_{yr}}^{r_m} \frac{B}{\mu_m} dr + 2\int_{r_m}^{r_\delta} \frac{B}{\mu_0} dr = n \cdot I_{eq} \tag{IV.9}$$

in which B denotes the magnetic flux density within PMs, sleeve and airgap, whereas μ_m is the PM magnetic permeability. Regarding r_{yr}, r_m and r_δ, they denote the outer radius of the corresponding rotor layers, as highlighted in Figure II.4. Moreover, I_{eq} and n are equivalent current and number of turns of a generic phase winding, whose product denotes the overall stator *mmf*.

Subsequently, the Gauss' Law can be applied to the closed surfaces red-highlighted in Figure II.4, leading to the following expression:

$$B(r) = B_{yr} \frac{r_{yr}}{r} \quad , \quad r \in \left[r_{yr}, r_\delta \right] \tag{IV.10}$$

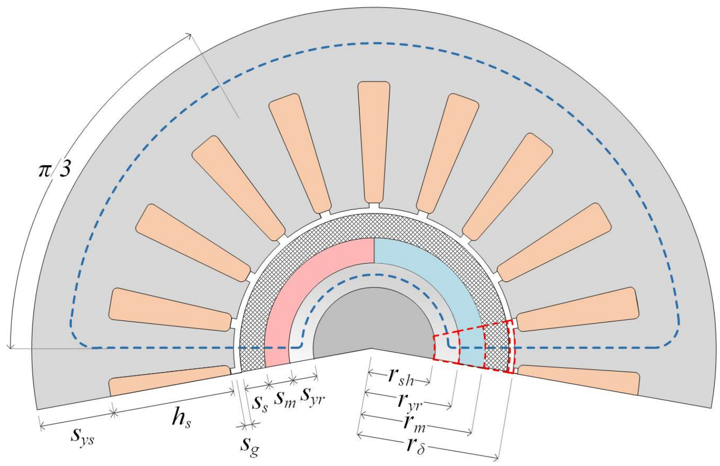

Figure II.4 - Closed magnetic flux path (blue) and surfaces (red) of HS-PMSM considered for Ampère's and Gauss' Laws implementation.

where B_{yr} is the magnetic flux density on the contact surface between PMs and the rotor back-iron. Therefore, the substitution of (IV.10) in (IV.9) leads to:

$$\frac{B_{yr}}{\mu_0} r_{eq} + H_c\, s_m = \frac{n\, I_{eq}}{2} \tag{IV.11}$$

where H_c is the PM coercive force, while r_{eq} is defined as:

$$r_{eq} = r_{yr} \left(\frac{\mu_0}{\mu_m} \ln\left(1 + \frac{s_m}{r_{yr}}\right) + \ln\left(1 + \frac{s_s + s_g}{r_{yr} + s_m}\right) \right) \tag{IV.12}$$

in which s_m, s_s and s_g denote the thickness of PMs, sleeve and airgap respectively. Hence, based on (IV.11), it is possible to identify the contributions of PMs ($B_{yr}^{(m)}$) and of stator *mmf* ($B_{yr}^{(i)}$) to the overall magnetic flux density as:

$$B_{yr}^{(m)} = -\mu_0 H_c \frac{s_m}{r_{eq}}, \quad B_{yr}^{(i)} = \mu_0 \frac{n\, I_{eq}}{2 r_{eq}} \ . \tag{IV.13}$$

Therefore, a suitable relationship between these two magnetic flux densities can be imposed in order to prevent PM demagnetization; particularly, $B_{yr}^{(i)}$ should not exceed a given share of $B_{yr}^{(m)}$ in accordance with:

$$B_{yr}^{(i)} = \alpha B_{yr}^{(m)} \tag{IV.14}$$

where the α coefficient has to be chosen within (0,1) properly. In conclusion, by substituting (IV.13) in (IV.14), the relationship between PM thickness, coercive force and stator *mmf* is achieved as:

$$n \cdot I_{eq} = -\alpha \cdot 2 H_c\, s_m \ . \tag{IV.15}$$

II.1.2.2 Electrical model

In order to achieve the HS-PMSM electrical model, some further assumptions are imposed:

- the magnetic flux density is square-shaped due to PM radial magnetization;
- the three-phase winding is distributed appropriately, i.e. each phase is distributed uniformly over an angular sector of π/3 per pole;
- a conventional current commutation control approach is considered.

As a result, the proposed HS-PMSM configuration is characterized by trapezoidal-shaped back-emf and its rated power is thus expressed as:

$$P = 2E_n \cdot I_n \tag{IV.16}$$

where E_n is the back-emf magnitude and I_n is phase current magnitude. These can be further expressed as:

$$E_n = p\,\omega_{m,n}\Lambda \;\;,\;\; I_n = \frac{I_{eq}}{2} \tag{IV.17}$$

in which p denotes the pole pairs, $\omega_{m,n}$ is the rotor rated speed and Λ is the magnetic flux linkage due to PMs only. The latter can be computed as:

$$\Lambda = 2nl_i r_{yr} B_{yr}^{(m)} \tag{IV.18}$$

in which r_{yr} denotes the outer radius of the rotor back-iron and l_i is the machine active axial length. as well. Therefore, by substituting (IV.13) and (IV.17) in (IV.16), the rated power can be expressed as:

$$P = -\mu_0 H_c s_m \frac{r_{yr}}{r_{eq}} p\omega_{m,n} \cdot 2l_i \cdot nI_{eq}\ . \tag{IV.19}$$

Consequently, by combining (IV.19) with (IV.15), the following relationship is achieved:

$$P = 4\mu_0 \frac{r_{yr}}{r_{eq}} p\omega_{m,n} \cdot l_i \cdot \alpha \cdot \left(H_c s_m\right)^2\ . \tag{IV.20}$$

In conclusion, based on (IV.20), it is possible to define HS-PMSM main dimensions in accordance with design specifications (H_c, α) and targets (P, $\omega_{m,n}$). In this context, it is worth noting the machine layer thicknesses should be chosen properly in order to comply also with mechanical constraints, namely the thicknesses of rotor layers should assure PM retention at any speed and temperature value within their corresponding operating ranges, as detailed extensively in the following section.

II.2 HS-PMSM design

II.2.1 Design targets

The HS-PMSM to be designed should be characterized by rated power and speed equal to 40 kW and 30 krpm respectively, so that the rated torque should be equal to about 12.7 Nm. These values have been chosen by considering a light duty EV. In addition, in order to be suitable for automotive applications, a wide CPSR is foreseen. Hence, the maximum speed ($\omega_{m,max}$) is set to 100 krpm, which requires that the HS-PMSM is coupled to a MaGT and a SGT characterized by a gear ratio of approximately 20 and 4, respectively. Due to the very high-speed operation, the number of magnetic poles has been set to the minimum possible value (2).

Regarding winding configuration, a three-phase distributed winding characterized by 3 slots per pole per phase has been chosen in order to assure a good trapezoidal shaped back-emfs. while the DC-link voltage has been imposed equal to 720 V in accordance with typical values occurring and foreseen for EVs [39], [40], as well as with HS-PMSM control needs. All the HS-PMSM design targets are summarized in Table II.1.

Given the targets above-mentioned, the design of the HS-PMSM has been developed referring to the machine structure shown in Figure II.1 and Figure II.4 and to the mathematical modelling presented in the previous sections, all the symbols of which are defined in Table II.2. Particularly, the electromagnetic and mechanical modelling described previously have been combined appropriately in order to develop a fast and effective analytical design procedure.

This is employed for designing a preliminary HS-PMSM configuration with the aim of minimizing HS-PMSM active volume by satisfying both mechanical and electromagnetic constraints simultaneously. Design constraints are detailed in the following sections, together with some analytical results.

II.2.2 Design constraints

Considering mechanical constraints at first, these consist of achieving proper values of both contact pressures and radial and tangential stress at any operating condition. Particularly, rotor design must ensure PMs retention at any speed as:

$$p_i^{(m)} > 0, \quad p_o^{(m)} > 0 \,. \tag{IV.21}$$

Furthermore, in order to avoid mechanical failure, the tangential and radial stress on the different layers must be lower than the maximum allowable value of the corresponding material ($\sigma^{(y)}{}_{r,max}$ and $\sigma^{(y)}{}_{\theta,max}$), as pointed out by:

$$\left|\sigma_x^{(y)}\right| < \left|s_f \sigma_{x,max}^{(y)}\right| \quad , \quad x \in \{r,\theta\} \ , \quad \mathrm{y} \in \{yr, m, s\} \tag{IV.22}$$

in which s_f is the safe coefficient, which should be chosen appropriately.

Table II.1 – HS-PMSM Design Targets

Description	***Symbol***	***Unit***	***Value***
Rated power	P_n	kW	40
Rated speed	$\omega_{m,n}$	krpm	30
Maximum speed	$\omega_{m,max}$	krpm	100
Rated torque	T_e	Nm	12.73
Pole pairs	p	-	1
DC-link voltage	V_{dc}	V	720
Magnetic ratio	α	-	0.7

Table II.2 – HS-PMSM nomenclature

Variable	***Symbol***
Shaft radius	r_{sh}
Outer rotor iron radius	r_{yr}
Outer magnet radius	r_m
Outer sleeve radius	r_s
Rotor yoke thickness	s_{yr}
PM thickness	s_m
Sleeve thickness	s_s
Air-gap	s_g
Stator outer radius	r_{st}
Stator yoke	s_{ys}
Slot height	h_s
Active length	l_i

Table II.3 - Materials properties

Description	***Symbol***	***Unit***	***Value***
Sleeve (CFRP 60%)			
Specific mass density	$\rho^{(s)}$	kg/m^3	1500
Radial young modulus	$E^{(s)}{}_r$	MPa	150000
Tangential young modulus	$E^{(s)}{}_\theta$	MPa	10000
Radial poisson ratio	$\upsilon^{(s)}{}_r$	-	0.34
Tangential poisson ratio	$\upsilon^{(s)}{}_\theta$	-	0.02
Tansile radial maximum stress	$\sigma^{(s)}{}_{r,max\_t}$	MPa	10
Compression radial maximum stress	$\sigma^{(s)}{}_{r,max\_c}$	MPa	200
Tansile tangential maximum stress	$\sigma^{(s)}{}_{\theta,max\_t}$	MPa	2400
Compression tangential maximum stress	$\sigma^{(s)}{}_{\theta,max\_c}$	MPa	1200
Rotor and Stator Cores (M235-35A) [41]			
Specific mass density	$\rho^{(yr)}$	kg/m^3	7600
Radial young modulus	$E^{(yr)}$	MPa	185000
Radial poisson ratio	$\upsilon^{(yr)}$	-	0.30
Maximum stress	$\sigma^{(yr)}{}_{max}$	MPa	700
Permanent Magnets (Ferrite) [42]			
Specific mass density	$\rho^{(m)}$	kg/m^3	5000
Radial young modulus	$E^{(m)}$	MPa	180000
Radial poisson ratio	$\upsilon^{(m)}$	-	0.28
Tensile maximum stress	$\sigma^{(m)}{}_{max\_t}$	MPa	60
Compression maximum stress	$\sigma^{(m)}{}_{max\_c}$	MPa	600
Remanence	$B_r{}^{(m)}$	T	0.4

Additionally, in order to avoid resonance phenomena, the critical speed must be reasonably higher than the HS-PMSM maximum speed. This is because HS-PMSM has to be mechanically able to reach an overspeed at least 10% (even 20%) more than the maximum operating speed. Consequently, the following relationship has to be considered:

$$\omega_{cr} \gg \omega_{m,\max} . \tag{IV.23}$$

Based on all the previous considerations, appropriate PM, sleeve and rotor yoke materials have been chosen, whose main properties and mechanical maximal stresses are reported in Table II.3, in which s_f is the safe coefficient, which should be chosen appropriately.

In particular, a Carbon Fibre Reinforced Polymer (CFRP) has been selected due to its high maximum tensile and compression tangential stress ($\sigma^{(s)}{}_{\theta,max\_t}$, $\sigma^{(s)}{}_{\theta,max\_c}$) and low mass density ($\rho^{(s)}$), which both ease the satisfaction of mechanical constraints.

Regarding electromagnetic constraints, a maximum α value is imposed in order to prevent PM demagnetization. Consequently, based on (IV.20), the following inequality is achieved:

$$\frac{r_{eq}}{r_{yr}}\frac{P}{4\mu_0\, p\omega_{m,n}\cdot l_i\left(H_c s_m\right)^2}\le\alpha_{max}\,. \tag{IV.24}$$

In addition, the back-emf magnitude is upper bounded as:

$$2E_n\le\gamma\cdot V_{dc} \tag{IV.25}$$

in which V_{dc} is the DC-link voltage and γ is an a-dimensional coefficient lower than one. The latter should account for additional voltage drops and also for preserving HS-PMSM dynamic performances at any speed. Consequently, by properly combining (IV.13), (IV.16) and (IV.17) with (IV.25), the number of turns of each phase winding can be chosen in accordance with:

$$n\le-\frac{\gamma\cdot V_{dc}\cdot\alpha\cdot\left(s_m\cdot H_c\right)}{2P}. \tag{IV.26}$$

II.2.3 Multi-parameter design procedure

The design of the HS-PMSM must account for both mechanical and electromagnetic aspects; this task is not trivial for the analytical calculation because of the large number of parameters involved. In addition, many of them affect both mechanical and electromagnetic aspects, which cannot be thus managed separately. Consequently, a fast and analytical multi-parameter design procedure has been developed in order to achieve a suitable preliminary HS-PMSM design by optimizing a given cost function.

The proposed procedure starts from a large HS-PMSM "population", namely a number of HS-PMSM configurations have been considered. Each HS-PMSM configuration is represented by a multi-parameter array, which consists of both tuneable and derived parameters, as pointed out in Table II.4. The tuneable parameters vary independently from each other within appropriate ranges and by appropriate steps, while derived parameters depend on tuneable parameters in accordance with mechanical and/or electromagnetic model introduced in the previous sections. The procedure first rejects all the HS-PMSM configurations that do not comply with the design constraints; as a result, the set of allowable HS-PMSM configurations is determined (*X*), as highlighted in Figure II.5. Subsequently, in order to identify a specific HS-PMSM configuration among all those belonging to *X*, an optimization criterion must be defined. In this regard, considering the application for which the HS-PMSM is designed (light duty EV), the minimization of the active volume (V_{act}) is imposed as:

$$V_{act} = \min_{r_m, s_m, s_s, \delta, l_i} \left\{ \pi r_{st}^2 \cdot l_i \right\} \tag{IV.27}$$

where r_{st} is the stator outer radius and l_i has been already defined (machine active axial length).

Table II.4 - HS-PMSM configuration parameters

	Parameters	***symbol***	***Unit***
Tuneable	*Inner magnet radius*	r_m	mm
	Magnet thickness	s_m	mm
	Sleeve thickness	s_s	mm
	Sleeve interference fit	δ	mm
	Active machine length	l_i	mm
Derived	*Radial and tangential stress*	$\sigma^{(y)}{}_r$, $\sigma^{(y)}{}_\theta$	MPa
	PM contact pressure	$p_i^{(m)}$	MPa
	Rotor critical speed	ω_{cr}	krpm
	Magnetic ratio	α	-

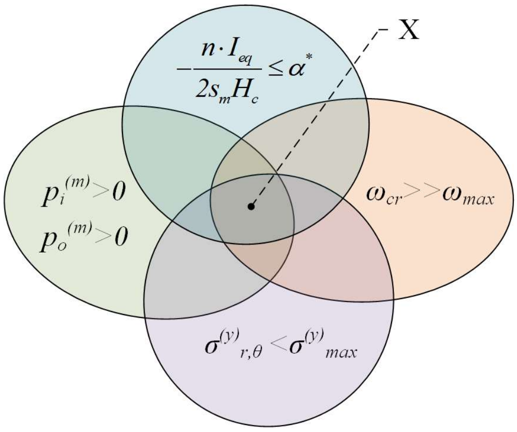

Figure II.5 - Set of allowable multi-parameter arrays determined by the proposed design procedure.

II.2.4 Design results

The main parameters of the designed HS-PMSM are summed up in Table II.5, together with its rated values. In addition, the proposed HS-PMSM with its main dimensions is reported in Figure II.6. It can be seen that a sleeve thickness of 5 mm is needed in order to satisfy the mechanical constraints with an interference δ equal to 0.3 mm. The mechanical radial and tangential stress (σ_r and σ_θ) acting on the rotor at the maximum speed, calculated in accordance with the mechanical analytical model, is highlighted in Figure II.7 as a function of the radial displacement. As expected, both absolute values of radial and tangential stress are always lower than the maximum stress limit of the different materials (red curves in Figure II.7). In addition, the evolutions of the contact pressure between rotor yoke and PMs ($p_i^{(m)}$) with the rotor speed, which is the most critical one, is highlighted in Figure II.8: this shows that $p_i^{(m)}$ values are always greater than zero at any operating condition within the maximum target speed (100 krpm), thus guaranteeing appropriate adhesion between the PMs and rotor yoke, ensuring the torque transmission properly. Regarding the design of the HS-PMSM stator, reference is made to phase windings, which requires choosing a wire size that guarantees the same performances over each operating condition. Therefore, a wire size of 6 mm^2 has been chosen and a maximum current density of 3 A/mm^2 is imposed, leading to a configuration of 6 parallel wires for each turn.

Subsequently, the slot fill factor and the ratio between slot and tooth widths have been set both to 0.54. Hence, slot sizes have been calculated, whereas stator yoke width has been determined in order to achieve fair values of magnetic flux density, by taking into account also the necessity to minimize iron losses at high-speed operation.

Table II.5 - Machine parameters and rated values

Description	***Symbol***	***Unit***	***Value***
Rated power	P_n	kW	40
Rated speed	$\omega_{m,n}$	krpm	30
Maximum speed	$\omega_{m,max}$	krpm	100
Rated torque	T_e	Nm	12.73
Rated current	I_n	A	99.7
Pole pairs	p	[-]	1
Phase resistance	R	mΩ	15.9
Phase inductance	L	mH	82.7
Magnetic ratio	α	[-]	0.70
Radial interference	D	mm	0.3
Shaft radius	r_{sh}	mm	12.5
Rotor yoke thickness	s_{yr}	mm	11.5
PM thickness	s_m	mm	10
Sleeve thickness	s_s	mm	5
Air-gap	s_g	mm	1.5
Stator outer radius	r_{ys}	mm	134.7
Stator yoke	s_{ys}	mm	34.2
Slot height	h_s	mm	57
Active length	l_i	mm	167
Active volume	V_{act}	dm^3	9.5

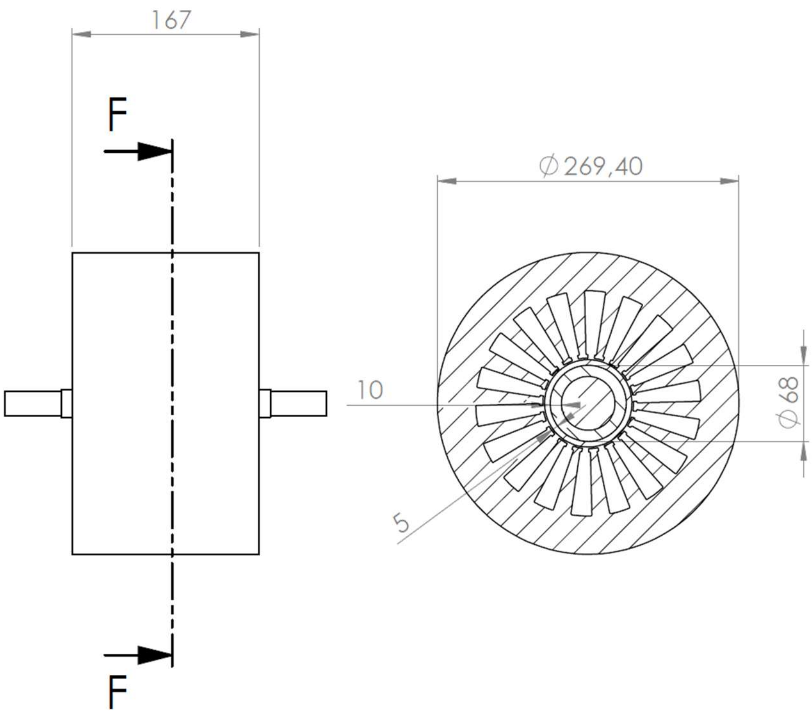

Figure II.6 – Schematic representation of the proposed HS-PMSM with its main dimensions.

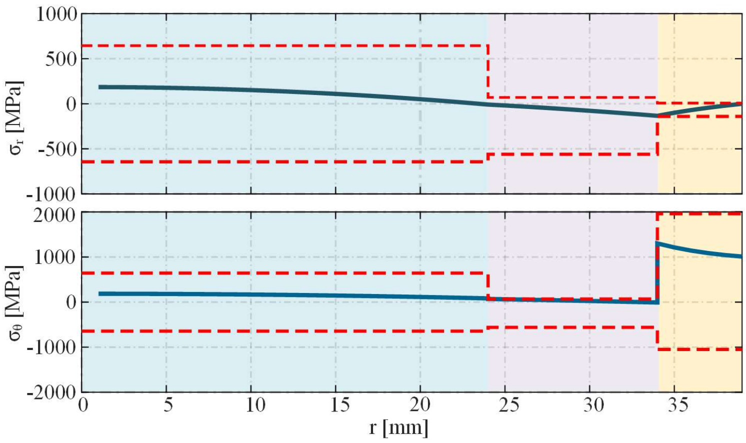

Figure II.7 - Radial (blue curve, top) and tangential stress distribution (blue curve, bottom) as a function of *r*, together with the maximum allowable stress of the materials (red dotted line): shaft + rotor yoke (blue zone), PMs (purple zone), sleeve (yellow zone).

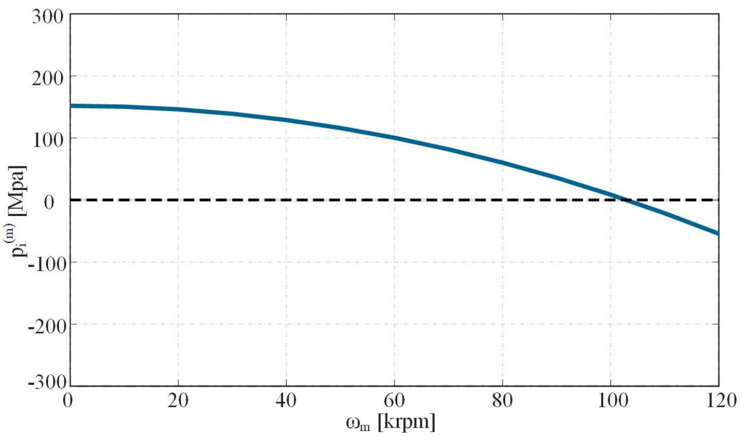

Figure II.8 - Contact pressure distribution between rotor yoke and PMs as a function of the rotational speed

II.3 Finite element analyses

In order to verify the proposed HS-PMSM configuration, extensive Finite-Element Analyses (FEAs) have been carried out by means of Solidworks and JMAG. This is done in order to corroborate the effectiveness of the proposed preliminary design procedure described in the previous sections.

The FEA simulation first regards the mechanical forces and contact pressures on the sleeve and on the PMs at first, i.e. $\sigma^{(s)}{}_{\theta}$ and $p_i^{(m)}$. Particularly, the distribution of $\sigma^{(s)}{}_{\theta}$ at $\omega_{m,max}$ is shown in Figure II.9; this reveals that $\sigma^{(s)}{}_{\theta}$ is maximum on the inner surface of the sleeve and decreases rapidly along the radial direction, as expected. The maximum tangential stress value for the sleeve is about 1300 MPa, which is much lower than the maximum tangential stress allowable by the CFRP (2400 MPa). In addition, the corresponding $p_i^{(m)}$ distribution at $\omega_{m,max}$ shown in Figure II.11 reveals that $p_i^{(m)}$ is approximately 8 MPa, thus guaranteeing appropriate adhesion between PMs and rotor yoke at any speed.

The electromagnetic FEA results at rated speed and torque are reported in Figure II.10 and Figure II.12. Particularly, the magnetic flux density distribution shown in Figure II.10 reveals quite low values compared to magnetic saturation thresholds of the iron core material (1.3 T), thus confirming the validity of the assumptions made during the electromagnetic modelling. In this context, it is worth emphasizing that Figure II.10 reveals a weak HS-PMSM magnetic exploitation. However, this is required in order to limit iron losses and back-emfs, especially at high-speed operation. The phase back-emfs evolutions depicted in Figure II.12 highlight good trapezoidal shapes, quite similar to the ideal ones, and their magnitudes comply with the voltage constraint imposed by (IV.25). In addition, Figure II.12 shows also the electromagnetic torque evolution at rated speed, which is achieved by supplying the HS-PMSM in accordance with a three-phase-on control approach [43]. These results point out the presence of a limited torque ripple (about 5%), revealing the effectiveness of the proposed HS-PMSM design. In addition, the chosen control approach enables good HS-PMSM performances in terms of maximum torque at rated speed (1.43 pu) and wide CPSR (from 30 krpm to 100 krpm), as well as no demagnetization issues at any speed, as highlighted in Figure II.13 and Figure II.14.

The good matching between analytical and FEA results are highlighted in Table II.6, although some differences occur on electromagnetic aspects. Particularly, magnetic flux densities achieved by FEA are lower than expected, leading to reduced torque and power. This can be justified mainly by the fact that the analytical procedure does not account for the iron contributions to the magnetic flux path, thus leading to an overestimation of the magnetic flux density. Consequently, if magnetic saturation occurs (which is not the case of the proposed HS-PMSM), the design procedure needs to be modified accordingly. However, it is worth emphasizing that the proposed analytical design procedure has been developed for preliminary design purposes only. Consequently, these differences do not undermine the proposed approach, which enables a rapid and effective HS-PMSM preliminary design.

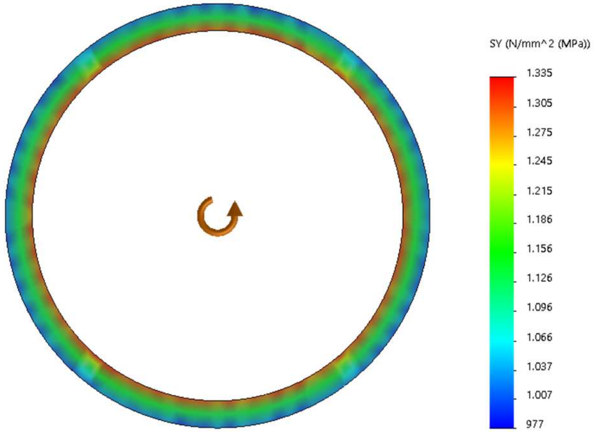

Figure II.9 - Tangential stress on the inner surface of the sleeve at $\omega_{m,max}$.

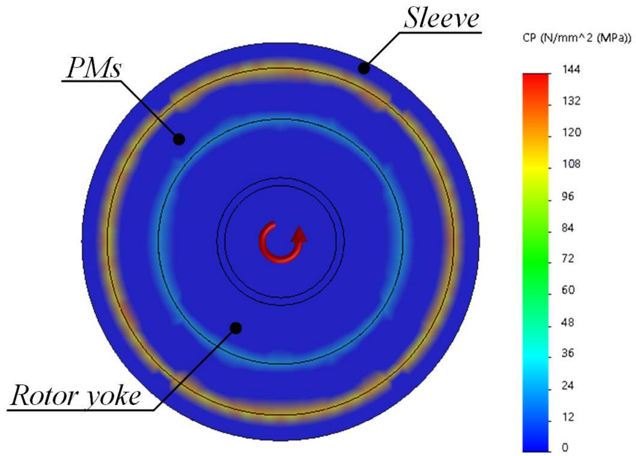

Figure II.11 - Contact pressure on the rotor surfaces at $\omega_{m,max}$.

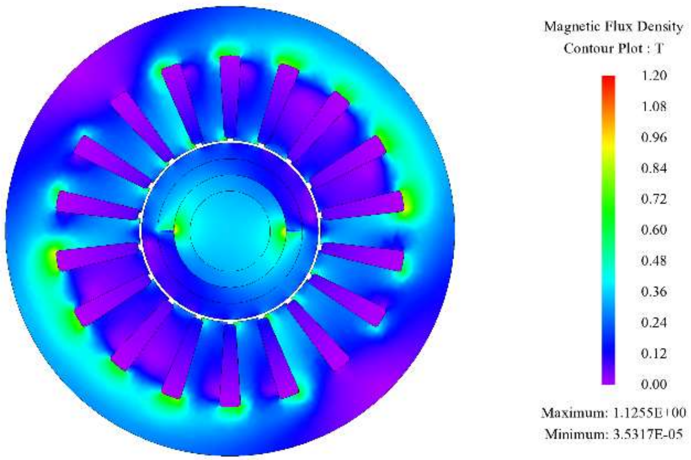

Figure II.10 - Magnetic flux density at ω_m = 30 krpm and T_e = 12.56 Nm.

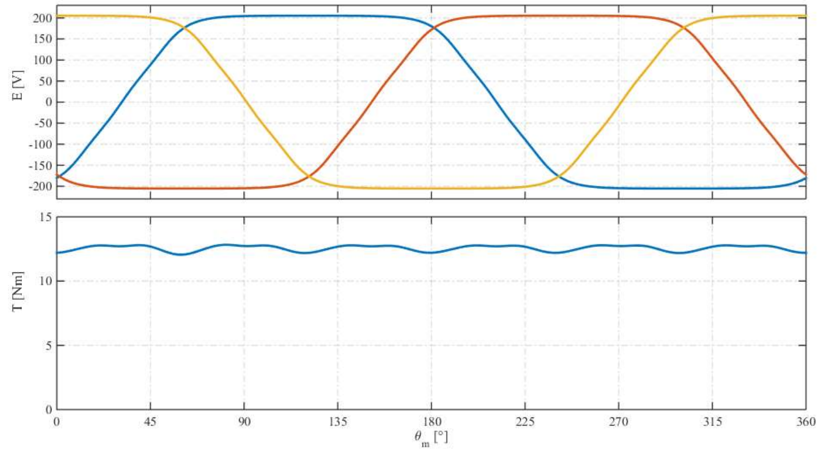

Figure II.12 - Phase back-emfs (on the top) and torque (on the bottom) at ω_m = 30 krpm.

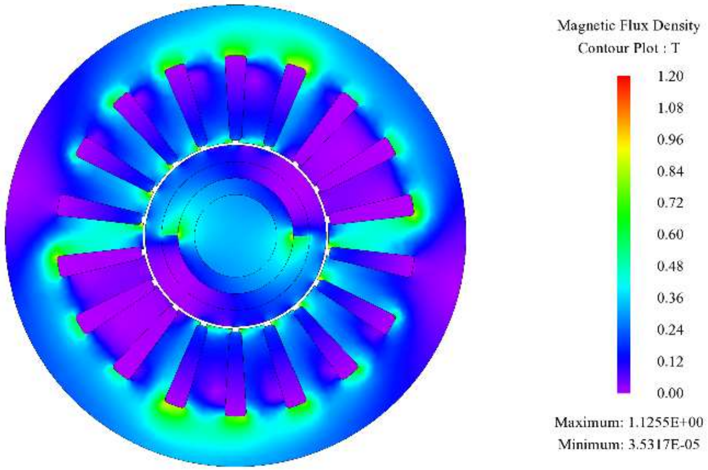

Figure II.13 - Magnetic flux density at ω_m = 30 krpm and T_e = 17.92 Nm.

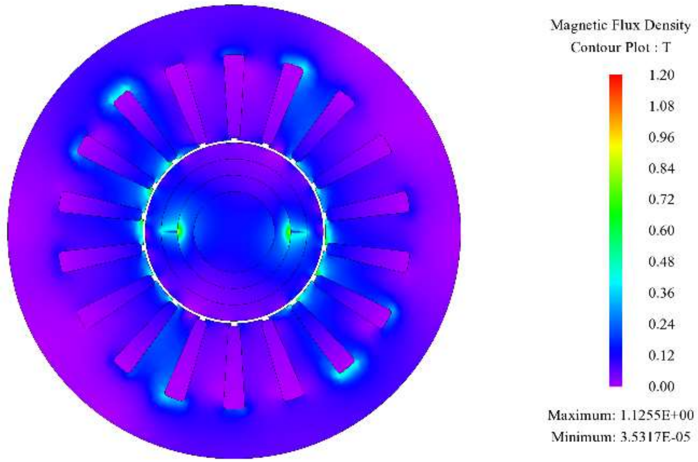

Figure II.14 - Magnetic flux density at ω_m = 100 krpm and T_e = 3.

Table II.6 - Analytical and FEA results

	Unit	***Analytics***	***FEA***
P_n	kW	40.0	39.45
T_e	Nm	12.73	12.56
E	V	204	205.4
$\bar{B}_m$	T	0.254	0.249
$\tilde{B}_m$	T	0.178	0.164
A	[-]	0.70	0.66
$\sigma^{(s)}_\theta$ *@100 krpm*	MPa	1302	1307
$p_i^{(m)}$ *@100 krpm*	MPa	8.6	7.0

III Magnetic Gear Transmission System

Magnetic Gear Transmission (MaGT) systems present some advantages compared to mechanical gear transmission systems, such as reduced maintenance, increased reliability and reduced acoustic noise [42]–[45] . Basically, MaGT can be grouped in two main classes: converter topology and field-modulated topology [9], [48], [49]. The former is derived from mechanical gear transmissions by simply replacing slots and teeth of the wheels with PMs, as shown in Figure III.1. However, the low exploitation of PMs for the torque transmission causes poor torque density. The second MaGT topology is based on the modulation of the magnetic field produced by two PM rotors. Therefore, all PMs can simultaneously contribute to torque transmission, guaranteeing higher torque density compared to the first category [48]–[50]. In 2001, a new configuration of MaGT belonging to the second topology was proposed [53], which is called coaxial MaGT, an example of which is shown in Figure III.2. It consists of two rotors that host the PMs, which are displaced in accordance with different numbers of pole pairs. Furthermore, a stationary ring made-up of ferromagnetic pole pieces is interposed between rotors; it has the task of modulating the magnetic field produced by the two PM distributions. The two rotors and the ferromagnetic ring are separated from each other by two air gaps, creating a contactless system. In this configuration, all the PMs contribute simultaneously to torque transmission, enabling very high theoretical torque densities, even above 100 kNm/m^3 [54], [55].

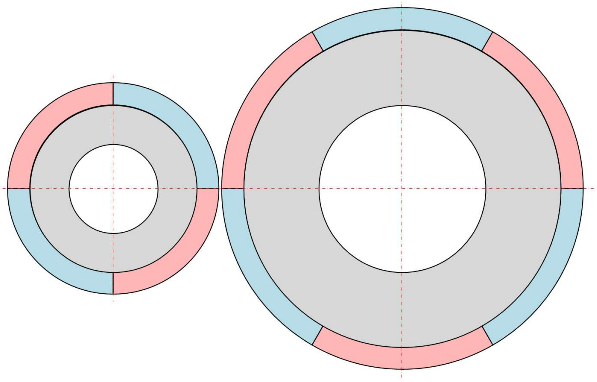

Figure III.1 - Schematic configuration of MaGT converter topology.

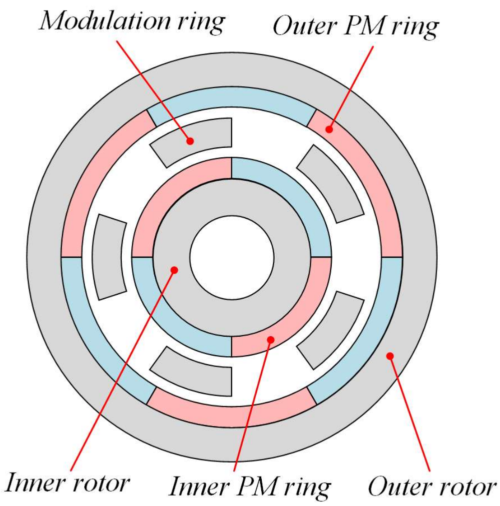

Figure III.2 - Schematic configuration of MaGT field-modulated topology called coaxial MaGT.

III.1 MaGT operating principle

Referring to the general configuration of coaxial MaGT, shown in Figure III.2, in which the name of the different main parts are reported, the magnetomotive forces produced by inner and outer PM rotors (F_i and F_o) can be assumed as square-shaped spatial distributions, as shown in Figure III.3. In particular, α_i and α_o denote the pole arc to pole pitch ratio of the inner and outer rotors respectively, while p_i and p_o are the number of PM pole-pairs of the inner and outer rotor. Furthermore, the magnetic permeance Γ generated by the locally fixed pole pieces can be considered as that shown in Figure III.4, where θ represents the modulation ring angle, β is the pole arc to pole pitch ratio of the modulation ring, and N_s is the number of ferromagnetic pole pieces. Therefore, the Fourier series expansions of F_i, F_o and Γ can be expressed as:

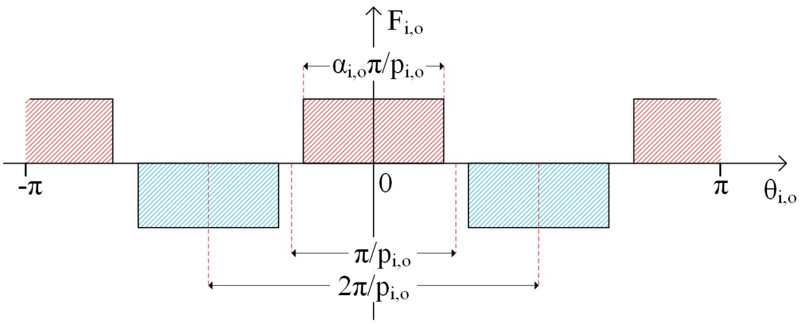

Figure III.3 - Magnetomotive forces produced by inner and outer PM rotors.

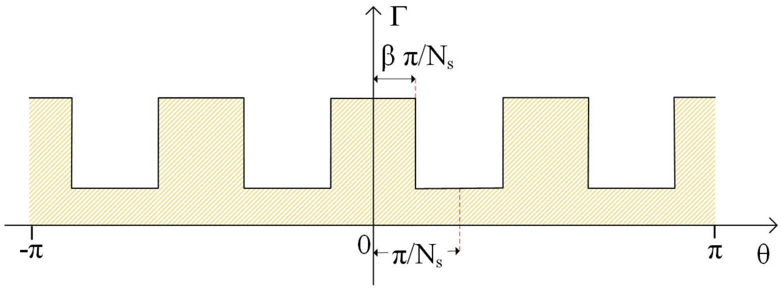

Figure III.4 - Magnetic permeance due to the modulation ring.

$$F_i(\theta_i) = \sum_{n=1}^{\infty} a_n \cos(p_i n \theta_i) \tag{V.1}$$

$$F_o(\theta_o) = \sum_{k=1}^{\infty} b_k \cos(p_o k \theta_o) \tag{V.2}$$

$$\Gamma(\theta) = c_0 + \sum_{h=1}^{\infty} c_h \cos(N_s h \theta) \tag{V.3}$$

in which a_n, b_k, c_0 and c_h represent the Fourier coefficients, which depend on α_i, α_o, and β. Considering the rotational speed of the two rotors, a coordinate transformation can be applied:

$$\theta_i = \theta - \omega_i t \tag{V.4}$$

$$\theta_o = \theta - \omega_o t \tag{V.5}$$

where ω_i and ω_o are the rotational speeds of the inner and outer rotor, while θ_i and θ_o represent the angular variables referred to inner and outer rotor reference frame respectively. Thus, (V.1) and (V.2) can be rewritten as:

$$F_i(\theta)=\sum_{n=1}^{\infty}a_n\cos\left(p_i n\left(\theta-\omega_i t\right)\right) \tag{V.6}$$

$$F_o(\theta)=\sum_{k=1}^{\infty}b_k\cos\left(p_o k\left(\theta-\omega_o t\right)\right). \tag{V.7}$$

By neglecting the outer PM rotor at first, the magnetic flux density distribution can be expressed as the product between the magnetomotive force generated by the inner PM rotor and the magnetic permeance as:

$$B_i(\theta)=F_i(\theta)\cdot\Gamma(\theta). \tag{V.8}$$

Further elaborating (V.8) yields:

$$\begin{aligned}B_i(\theta)&=c_0\sum_{n=1}^{\infty}a_n\cos\left(p_i n\left(\theta-\omega_i t\right)\right)+\\&+\sum_{j=\pm1}\sum_{h=1}^{\infty}\sum_{n=1}^{\infty}\frac{a_n c_h}{2}\cos\left(\left(jp_i n+N_s h\right)\left(\theta-\frac{jp_i n}{jp_i n+N_s h}\cdot\omega_i t\right)\right)\end{aligned}. \tag{V.9}$$

Equation (V.9) can be split as:

$$B_i=B_{f\_i}+B_{m\_i} \tag{V.10}$$

where:

$$B_{f\_i}=c_0\left(\sum_{n=1}^{\infty}a_n\cos\left(p_i n\left(\theta-\omega_i t\right)\right)\right) \tag{V.11}$$

$$B_{m\_i}=\sum_{j=\pm1}\sum_{n=1}^{\infty}\sum_{h=1}^{\infty}\frac{a_n c_h}{2}\cos\left(\left(jp_i n+N_s h\right)\left(\theta-\frac{jp_i n}{jp_i n+N_s h}\cdot\omega_1\,\mathrm{t}\right)\right). \tag{V.12}$$

From (V.10), it can be seen that the magnetic flux density distribution consists of two main contributions: a fundamental part (B_{f_i}) and a modulated part (B_{m_i}). The harmonic components of B_{f_i} are proportional to F_i through c_0, thus they depend on the harmonic content of the magnetomotive force produced by the inner PM rotor. Furthermore, B_{f_i} exhibits exactly the same speed and pole pair numbers of F_i, namely ω_i and np_i.

Different considerations apply for B_{m_i}, which is due to the variable magnetic permeance of the ferromagnetic pole pieces, which modulates F_i properly. In particular, B_{m_i} presents different frequencies than F_i, which can be obtained from (V.12) as:

$$\omega_{B_{m\_i}} = \frac{jp_i n}{jp_i n + N_s h} \cdot \omega_1 . \tag{V.13}$$

Furthermore, from (V.12), the numbers of pole pairs of B_{m_i} are given by:

$$p_{B_{m\_i}} = jp_i n + N_s h \tag{V.14}$$

Similar considerations hold for the magnetic flux density distribution due to the outer PM rotor (B_o), which can be achieved by neglecting the inner PM rotor and repeating the same procedure above-mentioned:

$$B_o(\theta) = F_o(\theta) \cdot \Gamma(\theta) . \tag{V.15}$$

Consequently, both B_{f_o} and B_{m_o} can be achieved as:

$$B_{f\_o} = c_0 \left(\sum_{k=1}^{\infty} b_k \cos\left(p_o k \left(\theta - \omega_o t \right) \right) \right) \tag{V.16}$$

$$B_{m\_o} = \sum_{j=\pm 1} \sum_{k=1}^{\infty} \sum_{h=1}^{\infty} \frac{b_k c_h}{2} \cos\left(\left(jp_o k + N_s h \right) \left(\theta - \frac{jp_o k \cdot \omega_o \, \mathrm{t}}{jp_o k + N_s h} \right) \right). \tag{V.17}$$

Furthermore, frequencies and pole pair numbers of $B_{m,o}$ can be obtained as:

$$\omega_{B_{m\_o}} = \frac{jp_o k}{jp_o k + N_s h} \cdot \omega_o \tag{V.18}$$

$$p_{B_{m\_o}} = jp_o k + N_s h . \tag{V.19}$$

Considering the effects of both inner and outer PM rotors simultaneously, it is necessary to guarantee a proper interaction between their magnetic flux densities with the aim of transmitting a constant torque. Consequently, the harmonic components of the fundamental part of B_i (B_{f_i}) must interact with the harmonic components of the modulated part of B_o (B_{m_o}) and vice versa. As a result, frequencies and numbers of pole pairs of B_{f_i} and $B_{m,o}$ and of B_{m_i} and $B_{f,o}$ must be the same. This is guaranteed by the following relationship between p_i, p_o and N_s:

$$p_o = N_s \pm p_i . \tag{V.20}$$

In conclusion, the relationship between inner and outer rotor speeds (ω_i and ω_o) can be obtained from (V.13) and (V.18) as:

$$\omega_o = \frac{\pm p_i}{p_o}\omega_i = \pm\frac{1}{G}\omega_i \tag{V.21}$$

where G denotes the gear ratio of the MaGT. The minus sign in (V.21) means that the two rotors may rotate even in opposite directions.

III.2 Coaxial MaGT modelling

Different aspects must be taken into account during the MaGT design stage, as for the HS-PMSM discussed in the previous chapter. In particular, magnetic and mechanical models are both fundamental for the design of a MaGT. The magnetic model allows the determination of the magnetic flux density distribution in the air gap regions, based on which it is possible to determine the magnetic torque transmitted among the rotors, also accounting for MaGT geometry and material characteristics. Furthermore, in high-speed applications, also the mechanical model is fundamental because of the mechanical stresses related to the high rotational speed. Therefore, appropriate mechanical constraints have to be introduced, which influence the rotor geometry and the PM configuration. In particular, PMs on the inner MaGT rotor should be enclosed by a mechanical sleeve in order to limit tensile stress and guarantee their retention at any speed, as occurring for the HS-PMSM rotor described in the previous chapter [31].

III.2.1 Magnetic model

In order to estimate the MaGT performance and torque, an accurate knowledge of the magnetic flux density distribution in the air gap regions is needed. This can be achieved by analytical, semi-analytical or numerical method by the support of FEA. The numerical method allows obtaining accurate results by considering the non-linearities of magnetic materials. However, this method is generally time consuming and difficult to use in the design stage because it should require a preliminary knowledge of geometric parameters [56]. For this reason, analytical methods are generally preferred, especially for a preliminary estimation of MaGT performances and for the subsequent design optimization.

A number of analytical approaches for computing magnetic flux density distribution and torque in slotted electrical machines can be found in the literature [54], [57], [58], in which the Laplace and Poisson's equations are solved in each subdomain of the machine in order to obtained the solution using appropriate boundary conditions. These equations are expressed respectively as:

$$\frac{\partial^2 A_x}{\partial r^2}+\frac{1}{r}\frac{\partial A_x}{\partial r}+\frac{1}{r^2}\frac{\partial^2 A_x}{\partial \theta^2}=0 \qquad x\in\{II, III\_j, IV\} \tag{V.22}$$

$$\frac{\partial^2 A_x}{\partial r^2}+\frac{1}{r}\frac{\partial A_x}{\partial r}+\frac{1}{r^2}\frac{\partial^2 A_x}{\partial \theta^2}=\frac{\mu_0}{r}\frac{\partial M_r}{\partial \theta} \qquad x\in\{I, V\} \tag{V.23}$$

where A is the magnetic potential vector, μ_0 is the permeability of the vacuum and M_r is the radial magnetization of the magnet.

Therefore, the MaGT magnetic model has been developed referring to a coaxial MaGT represented in pseudo polar coordinate system, as shown in Figure III.5. The MaGT domain is partitioned into five regions, i.e. the inner and outer PM rings (Region I and Region V), the inner and outer air gaps (Region II and Region IV) and N_s slots interposed within the modulation pole-pieces (Region III_j). The analytical model is established by magnetic potential vector in two-dimensional polar coordinate plane. As a result, the following expressions are achieved:

$$\begin{aligned} A_{I,V}(r,\theta)=&\sum_{n=1}^{\infty}\left(A_n^{I,V}\frac{P_n(r,R_{1,5})}{P_n(R_{2,6},R_{1,5})}+X_{n\_i,o}(r)\cos(n\varphi_{i,o})\right)\cos(n\theta)+\\ &+\sum_{n=1}^{\infty}\left(C_n^{I,V}\frac{P_n(r,R_{1,5})}{P_n(R_{2,6},R_{1,5})}+X_{n\_i,o}(r)\sin(n\varphi_{i,o})\right)\sin(n\theta) \end{aligned} \tag{V.24}$$

$$\begin{aligned} A_{II,IV}(r,\theta)=A_0^{I,IV}&+\sum_{n=1}^{\infty}\left(\begin{array}{l} A_n^{I,IV}\dfrac{R_{2,4}}{n}\dfrac{P_n(r,R_{3,5})}{E_n(R_{2,4},R_{3,5})}+\\ \qquad +B_n^{II,IV}\dfrac{R_{3,5}}{n}\dfrac{P_n(r,R_{2,4})}{E_n(R_{3,5},R_{2,4})}\end{array}\right)\cos(n\theta)+\\ &+\sum_{n=1}^{\infty}\left(\begin{array}{l} C_n^{II,IV}\dfrac{R_{2,4}}{n}\dfrac{P_n(r,R_{3,5})}{E_n(R_{2,4},R_{3,5})}+\\ \qquad +D_n^{II,IV}\dfrac{R_{3,5}}{n}\dfrac{P_n(r,R_{2,4})}{E_n(R_{3,5},R_{2,4})}\end{array}\right)\sin(n\theta) \end{aligned} \tag{V.25}$$

$$A_{III\_j} = A_0^{III\_j} + B_0^{III\_j} \ln r + \sum_{k=1}^{\infty} \begin{pmatrix} A_0^{III\_j} \dfrac{E_{k\pi/\beta}(r, R_4)}{E_{k\pi/\beta}(R_3, R_4)} + \\ -B_0^{III\_j} \dfrac{E_{k\pi/\beta}(r, R_4)}{E_{k\pi/\beta}(R_3, R_4)} \end{pmatrix} \cdot \cos\left(\frac{k\pi}{\beta}(\theta - \theta_j)\right) \quad \text{(V.26)}$$

in which the following notations is adopted for the sake of clarity:

$$\begin{aligned} P_w(u,v) &= \left(\frac{u}{v}\right)^w + \left(\frac{v}{u}\right)^w \\ E_w(u,v) &= \left(\frac{u}{v}\right)^w - \left(\frac{v}{u}\right)^w \end{aligned} . \quad \text{(V.27)}$$

Furthermore, n and k are positive integers, $\varphi_{i,o}$ is the angular displacement of the PM inner/outer polar axis referred to the reference position, as shown in Figure III.5, and $A^{I,IV}{}_n$, $C^{I,IV}{}_n$, $A^{II,IV}{}_n$, $B^{II,IV}{}_n$, $C^{II,IV}{}_n$, $D^{II,IV}{}_n$, $A^{III\_j}{}_0$, $B^{III\_j}{}_0$, $A^{III\_j}{}_k$, $B^{III\_j}{}_k$ are coefficients determined in accordance with appropriate boundary conditions, as fully detailed in Appendix (B). Moreover, θ_j is the angular position of the j-th slot, whose expression is reported in Appendix (B), as well as the expression of X_{n_i}, X_{n_o} and M_r.

Once the magnetic vector potentials in each subdomain have been determined, the radial and tangential flux density distribution in the two air-gap regions (Region II and Region IV) can be derived as:

$$B_{r\_II,IV} = \frac{1}{r}\frac{\partial A_{II,IV}}{\partial \theta}, \quad B_{\theta\_II,IV} = -\frac{\partial A_{II,IV}}{\partial r} . \quad \text{(V.28)}$$

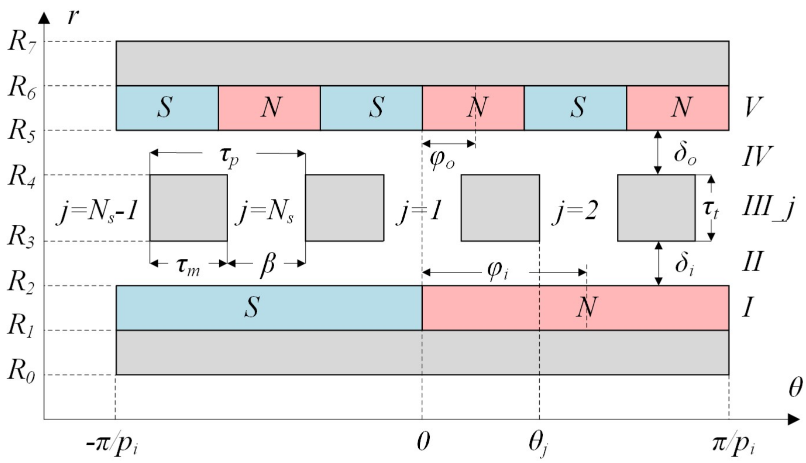

Figure III.5 - Analytical model of a coaxial MaGT in the pseudo polar coordinate system, where r and θ denote radial and angular displacement respectively.

The radial and tangential component of the magnetic flux density in these regions are:

$$B_{r\_II,IV}\left(r,\theta\right)=-\sum_{n=1}^{\infty}\left(\begin{array}{l}A_n^{II,IV}\dfrac{R_{2,4}}{r}\dfrac{P_n\left(r,R_{3,5}\right)}{E_n\left(R_{2,4},R_{3,5}\right)}+\\ \qquad +B_n^{II,IV}\dfrac{R_{3,5}}{r}\dfrac{P_n\left(r,R_{2,4}\right)}{E_n\left(R_{3,5},R_{2,4}\right)}\end{array}\right)\sin\left(n\theta\right)+ \\ +\sum_{n=1}^{\infty}\left(\begin{array}{l}C_n^{II,IV}\dfrac{R_{2,4}}{r}\dfrac{P_n\left(r,R_{3,5}\right)}{E_n\left(R_{2,4},R_{3,5}\right)}+\\ \qquad +D_n^{II,IV}\dfrac{R_{3,5}}{r}\dfrac{P_n\left(r,R_{2,4}\right)}{E_n\left(R_{3,5},R_{2,4}\right)}\end{array}\right)\cos\left(n\theta\right) \tag{V.29}$$

$$B_{\theta\_II,IV}\left(r,\theta\right)=-\sum_{n=1}^{\infty}\left(\begin{array}{l}A_n^{II,IV}\dfrac{R_{2,4}}{r}\dfrac{E_n\left(r,R_{3,5}\right)}{E_n\left(R_{2,4},R_{3,5}\right)}+\\ \qquad +B_n^{II,IV}\dfrac{R_{3,5}}{r}\dfrac{E_n\left(r,R_{2,4}\right)}{E_n\left(R_{3,5},R_{2,4}\right)}\end{array}\right)\cos\left(n\theta\right)+ \\ -\sum_{n=1}^{\infty}\left(\begin{array}{l}C_n^{II,IV}\dfrac{R_{2,4}}{r}\dfrac{E_n\left(r,R_{3,5}\right)}{E_n\left(R_{2,4},R_{3,5}\right)}+\\ \qquad +D_n^{II,IV}\dfrac{R_{3,5}}{r}\dfrac{E_n\left(r,R_{2,4}\right)}{E_n\left(R_{3,5},R_{2,4}\right)}\end{array}\right)\sin\left(n\theta\right). \tag{V.30}$$

Finally, the magnetic torque developed by the inner and outer rotor is achieved by using the Maxwell's stress tensor:

$$T_i=\frac{LR^2{}_{e\_i}}{\mu_0}\int_0^{2\pi}B_{r\_II}\left(r,\theta\right)\cdot B_{\theta\_II}\left(r,\theta\right)\cdot d\theta \tag{V.31}$$

$$T_o=\frac{LR^2{}_{e\_o}}{\mu_0}\int_0^{2\pi}B_{r\_IV}\left(r,\theta\right)\cdot B_{\theta\_IV}\left(r,\theta\right)\cdot d\theta \tag{V.32}$$

where R_{e_i} and R_{e_o} represents the mean radius in each air gap subdomain and L is the axial active length of the MaGT.

III.2.2 Mechanical model

The mechanical model of the MaGT has been developed referring to the inner rotor structure shown in Figure III.6. In particular, the rotor is made up of a rotor yoke (*yr*), a layer of ferrite PMs (m) and an outer sleeve (s). The sleeve is prestressed, meaning that its inner free radius is smaller than the free outer radius of PMs due to mechanical pretension; this is done due to the need of increasing mechanical retention of PMs. Since the rotor structure is the same adopted in subsection (II.1.1) for the HS-PMSM design, similar equations have been taken into account. Consequently, reference can be made to the mechanical modelling of a generic cylinder, which represents the base geometric structure of the MaGT rotor, in order to determine both radial and tangential stresses acting on each rotor layer. Hence, the following equations can be considered:

$$\sigma_r(r) = c_1 r^{k-1} + c_2 r^{-k-1} - \frac{(3+\upsilon_\theta)\rho\omega^2 r^2}{9-k^2} - E_\theta\left(\frac{r(2\alpha_\theta-\alpha_r)t}{4-k^2} + \frac{(\alpha_\theta-\alpha_r)t_0}{1-k^2}\right) \tag{V.33}$$

$$\begin{aligned}\sigma_\theta(r) = kc_1 r^{k-1} - kc_2 r^{-k-1} - \rho\omega^2 r^2\left(\frac{3(3+\upsilon_\theta)}{9-k^2} - 1\right) + \\ - E_\theta\left(\frac{2r(2\alpha_\theta-\alpha_r)t}{4-k^2} + \frac{(\alpha_\theta-\alpha_r)t_0}{1-k^2}\right)\end{aligned} \tag{V.34}$$

where υ_r and υ_θ are and Poisson's ratio in radial and tangential direction respectively, and α_r and α_θ are the thermal expansion coefficients in radial and tangential direction of the material. Moreover, c_1, c_2, t_o and t are constants which depend on the inner and outer cylinder pressure, on its rotational speed and temperature gradient. The expressions of c_1, c_2, t_o and t are reported in the Appendix (A). Furthermore, k is defined as:

$$k = \sqrt{\frac{E_\theta}{E_r}} \tag{V.35}$$

in which E_r and E_θ are the Young's modulus in radial and tangential direction of the cylinder material, as previously defined in subsection (II.1.1).

Subsequently, the valuation of σ_r and σ_θ on each layer require the knowledge of the pressure exerted on its contact surfaces by the surrounding materials. The solution must be obtained starting from the rotor layer radial displacement u_r defined by Hooke's law, which is expressed as:

$$u_r^{(y)} = \frac{r}{E_\theta^{(y)}}\left(\sigma_\theta^{(y)} - k\upsilon_r^{(y)}\sigma_r^{(y)} + E_\theta^{(y)}\alpha_\theta^{(y)}\Delta T^{(y)}\right), \qquad \mathrm{y} \in \{yr, m, s\} \tag{V.36}$$

where ΔT is the difference between actual and reference temperatures in each rotor layer. Consequently, the contact pressures on the PM layer can be computed by solving the following linear system:

$$\begin{aligned} \left(u_r^{(s)} - u_r^{(m)}\right)\Big|_{r=r_m} &= \delta \\ \left(u_r^{(m)} - u_r^{(yr)}\right)\Big|_{r=r_{yr}} &= 0 \end{aligned} \tag{V.37}$$

in which δ is the radial interference, i.e. the difference between the outer radius of PM and the free inner radius of the sleeve. In particular, the substitution of (V.33)-(V.36) into (V.37) makes (V.37) independent from tangential and radial stresses (σ_r and σ_θ), which can be computed later by solving (V.33) and (V.34) separately.

Mechanical modelling has to account also for critical speeds in order to avoid resonance phenomena. Therefore, the rotor first critical speed, which should not be reached in order to preserve rotor integrity, can be estimated as [38]

$$\omega_{m,cr} = \sqrt{\frac{g}{d_{st}}} \tag{V.38}$$

in which g is gravity acceleration constant and d_{st} is the rotor static deflection, which depends on rotor layer geometry and material properties.

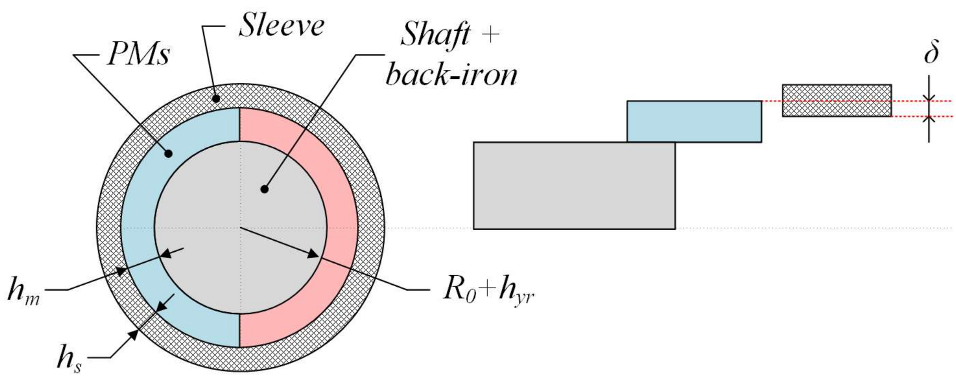

Figure III.6 - MaGT inner rotor structure, in which δ denotes the radial interference between the PM ring and the sleeve.

III.3 Coaxial MaGT design

Referring to a coaxial MaGT and considering the analytical magnetic and mechanical formulations described in the previous section, a preliminary design of a MaGT has been carried out in order to comply with all the imposed targets and constraints. In this regard, an analytical multi-parameter design procedure similar to that already developed for HS-PMSM design has been considered, which ensures an optimal MaGT design by optimizing a given cost function.

III.3.1 Design targets

The MaGT to be designed should be coupled to the ferrite-based HS-PMSM already designed in Chapter II, which is characterized by rated power and speed equal to 40 kW and 30 krpm, respectively. Consequently, the input torque of MaGT (T_i) should be at least equal to the rated torque of HS-PMSM (T_n, 12.7 Nm), as stated by the following constraint:

$$T_i \geq T_n \,. \tag{V.39}$$

In addition, the MaGT must be designed for a maximum input speed ($\omega_{i,max}$) at least equal to the maximum speed of the HS-PMSM ($\omega_{m,max}$), leading to:

$$\omega_{i,\max} \geq \omega_{m,\max} \,. \tag{V.40}$$

Therefore, in order to enable the MaGT to couple the HS-PMSM with the vehicle wheels, the gear ratio G has been estimated about 20 in order to adapt speed and torque values properly. In addition, a new ferrite-based configuration is designed, not only for limiting PM costs and availability issues, but also for their very low eddy-current losses, especially compared to NdFeB PMs.

III.3.2 Magnetic design

In order to make MaGT able to operate as a speed reducer, the two rotors must have different numbers of pole pairs and, thus, different speed values. In particular, the gear ratio G can be defined from (V.21) as:

$$G = \frac{\omega_i}{\omega_o} = \frac{p_o}{p_i}. \tag{V.41}$$

Furthermore, the synchronism between the magnetic flux densities produced by the two rotors has to be guaranteed by the ferromagnetic ring. This has the task of modulating the magnetic flux densities produced by two PM rotors so that they would be characterized by the same number of pole pairs and speed value. This goal requires satisfying (V.20), leading to:

$$p_i + p_o = N_s. \tag{V.42}$$

In addition, in order to limit the torque ripple, a suitable ripple factor k is defined in [10] as:

$$k = \frac{2p_i N_s}{LCM\left(2p_i, N_s\right)} \tag{V.43}$$

where LCM denotes the Least Common Multiple between the number of poles of the inner rotor and the pole-pieces. The lowest possible torque ripple is obtained if k equals one, which is thus the ideal case. Therefore, based on (V.43), if an even value is chosen for p_i, p_o should be odd, and vice versa. This rule enables larger LCM and, thus, lower ripple factor.

III.3.3 Mechanical design

The mechanical design has been carried in order to achieve proper values of both contact pressure and radial and tangential stress at any operating condition. Hence, appropriate PM, sleeve and rotor materials have been chosen, whose main properties and mechanical maximal stresses are reported in Table II.3, which ease the satisfaction of mechanical constraints. The latter consist of both maximum radial and tangential stresses and minimum contact pressures, as highlighted by the following expressions:

$$\left|\sigma_x^{(y)}\right| < \left|s_f \sigma_{x,max}^{(y)}\right| \quad , \quad x \in \{r, \theta\} \ , \quad \mathrm{y} \in \{yr, m, s\} \tag{V.44}$$

$$p_i^{(m)} > 0\,, \quad p_o^{(m)} > 0 \tag{V.45}$$

in which s_f is a safety coefficient and $p_i^{(m)}$ and $p_o^{(m)}$ are the most critical contact pressures, which act on the contact surfaces of the PM ring.

Referring to (V.45), it is worth noting that the contact pressure $p_i^{(m)}$ between the PM ring and the rotor yoke and achieved at $\omega_{i,max}$ should be greater enough in order to guarantee torque transmission properly. In this regard, satisfying (V.45) benefits also from the glue interposed between the PM ring and the iron yoke, whose effects have been neglected for the sake of simplicity.

In conclusion, the MaGT speed constraint can be expressed as:

$$\omega_{i,\max} \ll \omega_{cr} \tag{V.46}$$

in which ω_{cr} is the first critical speed of the MaGT inner rotor.

III.3.4 Multi-parameter design procedure

In order to identify a specific MaGT configuration among all those that comply with the design constraints previously mentioned, a multi-parameter design procedure similar to that used for designing the HS-PMSM in the previous chapter has been developed. It starts from a multi-parameter array, which consists of both tuneable and derived parameters, as pointed out in Table III.1. The tuneable parameters vary independently from each other within appropriate ranges, while derived parameters depend on tuneable ones in accordance with mechanical and/or magnetic model introduced in the previous sections.

The first step of the proposed procedure consists of considering all the multi-parameter arrays that comply with $k = 1$ and (V.42). Subsequently, the design procedure rejects all the MaGT configurations that do not comply with (V.39) and (V.40) and, then, with (V.44), (V.45) and (V.46). As a result, the most suitable multi-parameter array is finally chosen among the remaining configurations by adopting the following optimization criterion:

$$x = x^* \,, \quad f(x^*) = \min_{x \in X}\left\{ f\left(x\right)\right\} \tag{V.47}$$

where f can be chosen differently in order to optimize different MaGT properties. In particular, considering the application for which the MaGT is designed (light duty vechile), the minimization of the active volume (V_{act}) is imposed as:

$$V_{act} = \min_{R_2, h_m, h_s, h_f, \delta, L} \left\{ \pi R_7^{\,2} \cdot L \right\} \tag{V.48}$$

Table III.1 - MaGT configuration parameters

	Parameters	symbol	Unit
Tunable	*Inner pole pairs*	p_i	-
	Outer pole pairs	p_o	-
	Inner magnet radius of inner rotor	R_2	mm
	PMs thickness	h_m	mm
	Modulation ring thickness	h_f	mm
	Sleeve thickness	h_s	mm
	Radial interference	δ	mm
	Axial length	L	mm
Derived	*Max inner rotor torque*	T_i	Nm
	Max outer rotor torque	T_o	Nm
	Tangential and radial Sleeve strength	$\sigma^{(s)}{}_{r,\theta}$	MPa
	PM contact pressure	$p_i^{(m)}$	MPa
	Rotor critical speed	ω_{cr}	krpm

III.3.5 Design results

The main parameters of the designed single-stage MaGT are summed up in Table III.2. It can be seen that a great number of outer pole pairs are necessary because of the high gear ratio required (20). Such a large value of outer pole pairs causes weak MaGT performances, especially in terms of maximum input torque density. Therefore, the minimum input torque target can be satisfied only by resorting to large radial dimension. Consequently, the mechanical stresses on the inner rotor are very high and, above all, a relatively low maximum rotational speed is achieved due to PM contact pressures issues. This is proved by Figure III.7, which shows the evolution of the contact pressure $p_i^{(m)}$ between the inner PM ring and the iron yoke with ω_i, which is more critical than $p_o^{(m)}$. In particular, a relatively low maximum operating speed (approximately 30 krpm) is achieved, which just equals HS-PMSM rated speed and, thus, is quite far from the HS-PMSM maximum speed (100 krpm). The evolutions of radial and tangential stresses in the different rotor layers with r at the maximum speed of the designed MaGT is depicted in Figure III.8, which shows that they comply with all the mechanical constraints imposed in the design stage.

Table III.2 - Single stage MaGT values

Description	***Symbol***	***Unit***	***Value***
Inner pole pairs	p_i	-	2
Outer pole pairs	p_o	-	41
Pole pieces	N_s	-	43
Gear Ratio	G	-	20.5
PMs thickness	h_m	mm	29
Modulation ring thickness	h_f	mm	80
Sleeve thickness	h_s	mm	10
Air-gap	h_g	mm	1
Radial interference	δ	mm	0.7
Axial length	L	mm	250
Shaft radius	R_0	mm	12.5
Inner iron yoke thickness	h_{yi}	mm	55
Middle iron yoke thickness	h_{ym}	mm	-
Outer iron yoke thickness	h_{yo}	mm	30
Active volume	V_{act}	dm^3	47.9

III.4 Coaxial Double-stage MaGT design

Since the designed single-stage MaGT presented in the previous section is characterized by an unsatisfactory maximum speed due to a very high gear ratio, an alternative solution must be pursued. Two or more series-connected Coaxial MaGTs could be adopted in order to guarantee a subsequent reduction of the input rotational speed. However, this solution could be unacceptable if volume and weight are strict constraints. Therefore, an alternative solution is represented by an integrated double-stage coaxial MaGT. In this configuration, a second coaxial MaGT is mounted coaxially to the first MaGT, as shown in Figure III.9, so that the outer rotor of the first stage (S1) is also the inner rotor of the second stage (S2). In this way, a first reduction of the rotational speed between inner and middle rotors is achieved, followed by a second further reduction between middle and outer rotors. As a result, the total gear ratio G_{tot} is given by the product of the single gear ratios of each stage as:

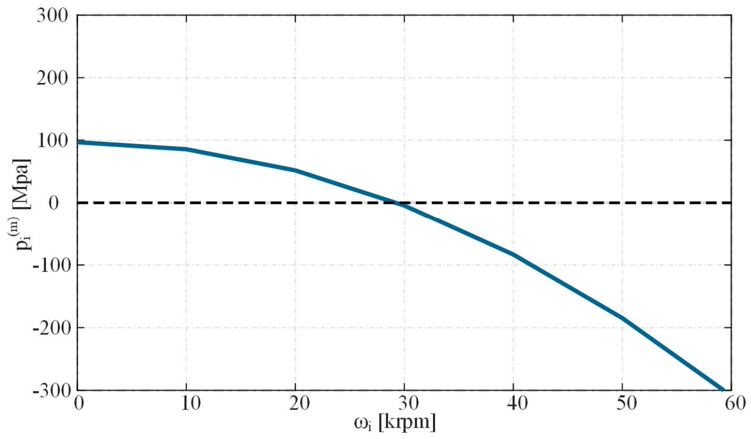

Figure III.7 – Evolution of $p_i^{(m)}$ with ω_i for the designed single-stage MaGT.

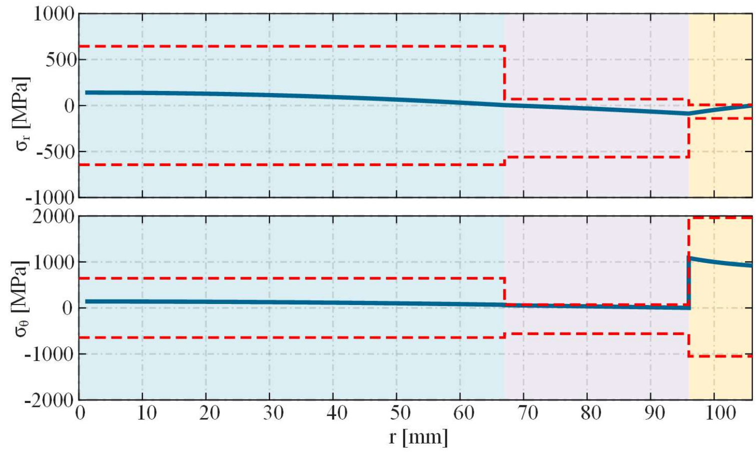

Figure III.8 - Radial (blue curve, top) and tangential stress distribution (blue curve, bottom) in the radial direction on the single stage MaGT inner rotor as a function of *r*, together with the maximum allowable stress of the materials (red dotted line): rotor yoke (blue zone), PMs (purple zone), sleeve (yellow zone).

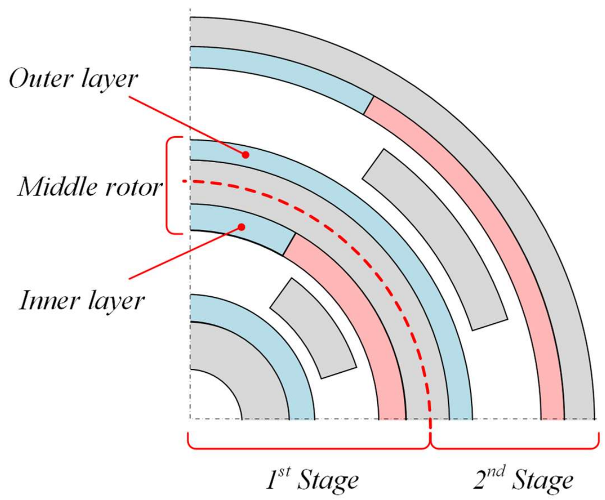

Figure III.9 – Double-stage coaxial MaGT configuration.

$$G_{tot} = G_{S1} \cdot G_{S2} = \frac{p_{o,S1}}{p_{i,S1}} \frac{p_{o,S2}}{p_{i,S2}} = \frac{\omega_{i,S1}}{\omega_c} \frac{\omega_c}{\omega_{o,S2}} \tag{V.49}$$

in which G_1 and G_2 represent S1 and S2 gear ratio respectively, ω_c is the rotational speed of the middle rotor and $p_{i/o,1/2}$ is the number of pole pairs of the inner/outer layers of S1 and S2.

III.4.1 Design results

The design of the double-stage MaGT has been accomplished by assuming infinite permeability of the ferromagnetic material; this allows S1 and S2 of the MaGT to be considered separately since the middle yoke acts as an ideal closure path for the flux density lines. While flux densities lines within the low-permeability regions of the double-stage MaGT are exactly the same as in two independent MaGTs [59]. Since the double-stage MaGT is designed for the same purpose of the single-stage MaGT (coupling to the HS-PMSM discussed in chapter II), the same targets and constraints previously discussed have been imposed. However, two different PM materials have been considered alternatively, namely NdFeB and Ferrites magnets.

First considering the MaGT S1, the same multi-parameter design procedure used for the single-stage MaGT is employed. However, instead of minimizing the active volume by (V.48), all the remaining MaGT S1 configurations that comply with all design targets and constraints have been evaluated in terms of active volume and costs, as depicted from Figure III.10 to Figure III.13.

Focusing on Figure III.10 and Figure III.11, these have been achieved by employing NdFeB PMs, considering a PM thickness variable within [2,20] mm with 2 mm step. However, as far as both volume and cost minimization are concerned, reference can be made just to Figure III.11, which highlights the Pareto frontier clearly (red dots). This consists of just 5 MaGT S1 among approximately 500 thousand of allowable solutions. Since the volume varies slightly among the 5 selected configurations (less than 4%), the configuration characterized by the minimum cost has been chosen, although it is characterized by the maximum volume.

Similar considerations apply to Figure III.12 and Figure III.13, which have been achieved by using Ferrite PMs. However, the comparison between Figure III.10 and Figure III.12 reveals that ferrite-based configurations lie within a much less plane area than NdFeB, which does not enclose low-volume and high-cost regions: this is because relatively great PM thickness are always concerned, thus the overall MaGT volume cannot be reduced below a certain threshold (approximately 10 dm^3). Additionally, much less allowable configurations are achieved by employing Ferrite PMs (approximately 10 thousand versus 500 thousand achieved by NdFeB), but which are cheaper for a given target volume: this is because the greater volumes required by ferrite-based MaGT result in a much smaller number of allowable solutions that comply with the design constraints, but the cost of Ferrite PMs is much lower than NdFeB PMs. Considering the Pareto frontier shown in Figure III.13, it consists of just 4 configurations, among which the cheapest configuration has been chosen because the volume does not change significantly among them. However, by comparing Figure III.11 to Figure III.13, Ferrite PMs lead to both increased volume and costs compared to NdFeB worst cases (+877 % and +60 % respectively); such a huge volume increase is due to weak Ferrite magnetic performance, which leads also to significant cost increase.

A similar selecting procedure can be adopted for designing the MaGT S2, leading to the overall results shown in Table III.3. The comparison between NdFeB-based and Ferrite-based MaGT reveals that the NdFeB-based configuration is characterised by a much lower volume and weight compared to the Ferrite-based configuration (4.2 dm^3 versus 27 dm^3 and 25 kg versus 150 kg respectively). As a result, the NdFeB-based MaGT achieves higher maximum speed than the ferrite-based configuration (approximately 80 krpm versus 60 krpm), as shown in Figure III.14 and Figure III.15. Furthermore, it is worth noting that, although NdFeB material is very expensive compared to Ferrite material, the NdFeB-based configuration has a lower overall cost than Ferrite-based due to the very small amount of PM material needed by the former.

The comparison between Table III.2 and Table III.3.reveals a significant decrease of the number of outer pole pairs for both the double-stage MaGTs compared to the ferrite-based single-stage solution. In particular, the double-stage Ferrite-based MaGT presents a volume greater than the double-stage NdFeB-based MaGT, but smaller than the single-stage MaGT: consequently, although the maximum speed achieved by the double-stage ferrite-based MaGT is still lower than the design target (approximately 60 krpm versus 100 krpm), it is almost doubled compared to the single-stage MaGT (approximately 30 krpm), thus revealing the enhanced performances achievable by the double-stage configuration.

Table III.3 – Double-stage MaGTs design specifications

Description	***Symbol***	***Unit***	***MaGT (NdFeB-based)***		***MaGT (Ferrite-based)***	
			S1	***S2***	***S1***	***S2***
Inner pole pairs	p_i	-	2	2	2	2
Outer pole pairs	p_o	-	9	9	9	9
Pole pieces	N_s	-	11	11	11	11
Gear Ratio	G	-	4.5	4.5	4.5	4.5
Overall Gear Ratio	G_{tot}	-	20.25		20.25	
PMs thickness	h_m	mm	4	6	18	19
Modulation ring thickness	h_f	mm	12	21	16	25
Sleeve thickness	h_s	mm	1	1	6	5
Air-gap	h_g	mm	1	1	1	1
Radial interference	δ	mm	0.2	0.2	0.4	0.4
Axial length	L	mm	100		240	
Shaft radius	R_0	mm	12.5		12.5	
Inner iron yoke thickness	h_{yi}	mm	13.5		21.5	
Middle iron yoke thickness	h_{ym}	mm	15		20	
Outer iron yoke thickness	h_{yo}	mm	15		20	
Active volume	V_{act}	dm^3	4.2		22.5	
Active cost	C_{act}	€	530		750	

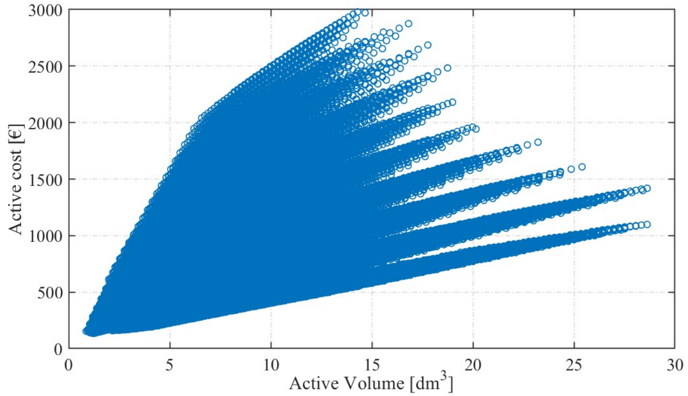

Figure III.10 - Cost-volume analysis of NdFeB-based MaGT S1 configurations.

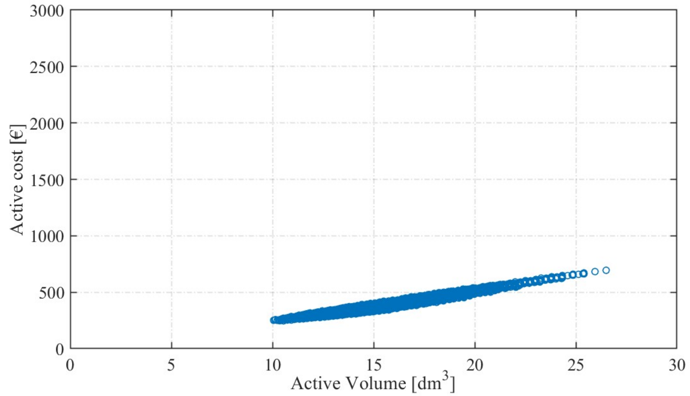

Figure III.12 - Cost-volume analysis of Ferrite-based MaGT S1 configurations.

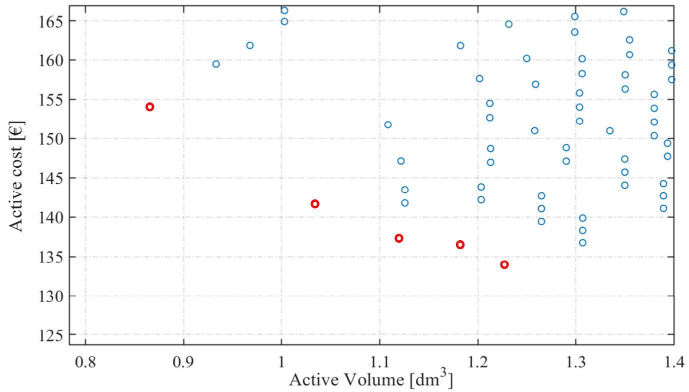

Figure III.11 - Zoomed sight of Figure III.10 which highlights the Pareto frontier (red dots).

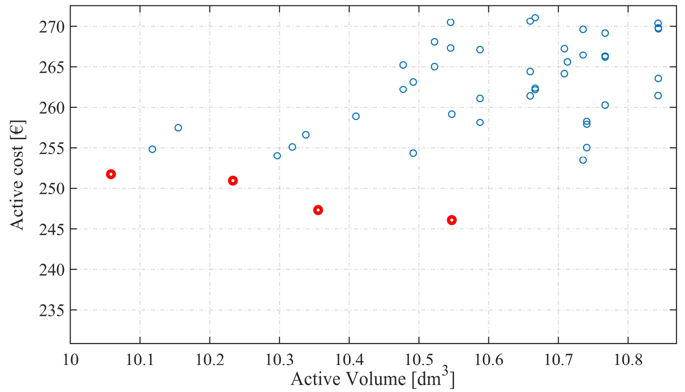

Figure III.13 - Zoomed sight of Figure III.12. which highlights the Pareto frontier (red dots).

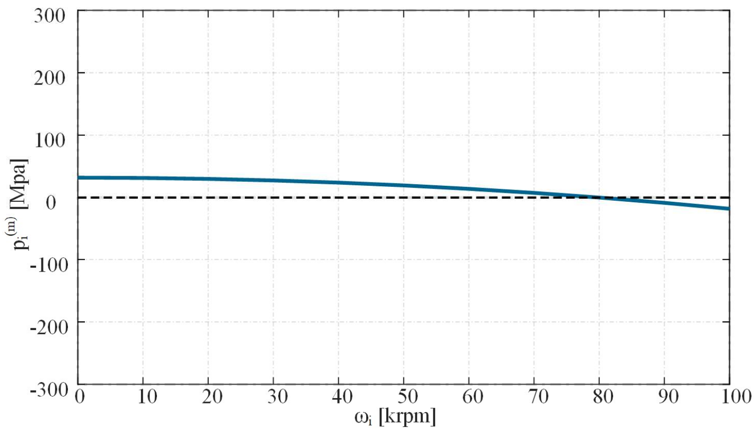

Figure III.14 - Evolution of $p_i^{(m)}$ with ω_i in the inner rotor of the double-stage NdFeB-based MaGT.

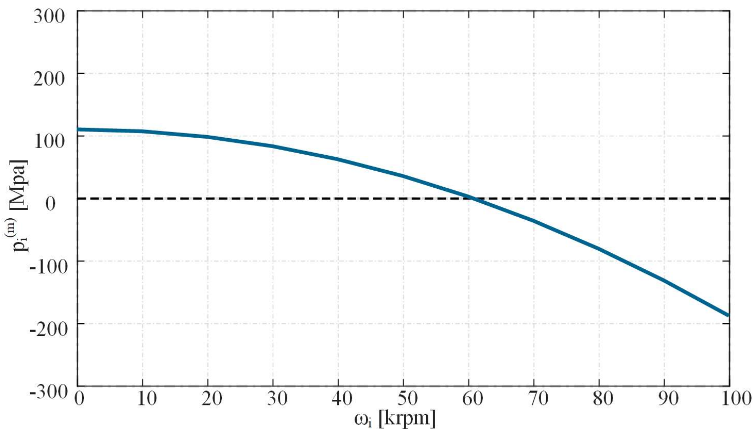

Figure III.15 - Evolution of $p_i^{(m)}$ with ω_i in the inner rotor of the double-stage ferrite-based MaGT.

III.4.2 Finite element analyses

In order to verify the preliminary design of the double-stage MaGTs, Finite-Element Analyses (FEAs) have been carried out by means of Solidworks and FEMM. The FEA simulations regard the mechanical stress acting on the inner rotor of each double-stage MaGT, particularly the tangential stress on the sleeve and the contact pressure between the PM ring and the iron yoke. In this regard, the distribution of σ_θ at maximum rotational speed is shown in Figure III.16 and Figure III.17, which highlights that σ_θ is higher on the inner surface of the sleeve, whereas it decreases rapidly along the radial direction, as expected. The maximum tangential stress value is approximately 1600 MPa for NdFeB-based MaGT and 1900 MPa for ferrite-based configuration respectively, which are much lower than the maximum stress allowable by the CFRP (2400 MPa). In addition, the corresponding contact pressures distributions shown in Figure III.18 and Figure III.19 reveals that $p_i^{(m)}$ is approximately 18 MPa for both configurations, thus guaranteeing appropriate adhesion between PMs and rotor yoke at the maximum speed and, thus, at any lower speed values.

Regarding magnetic FEA, the magnetic flux density distributions for both MaGT configurations when the torque is zero or maximum are shown in Figure III.20, Figure III.21, Figure III.22, and Figure III.23. In this regard, NdFeB-based MaGT configuration reveals excessive values of magnetic flux density (up to about 2.0 T) compared to the magnetic saturation threshold of the core material (about 1.5 T). The same does not go for the Ferrite-based MaGT configuration, which is characterized by lower magnetic flux density values, thus making the assumption of infinity permeability of ferromagnetic layers more consistent. This is highlighted also from Figure III.24 to Figure III.27, which show the analytical and FEA evolutions of the radial and tangential component of magnetic flux density in the four air gaps for both configuration when the torque is zero or maximum. In particular, some mismatches occur between radial components achieved by the analytical procedure and FEA for NdFeB-based MaGT, which determine a corresponding torque mismatch. In this regard, the torque distribution in the three rotors is shown in Figure III.28 and Figure III.29 for NdFeB-based and Ferrite-based MaGT configuration respectively. These results point out that the constraints related to the minimum input torque, which are governed by (V.39), has been satisfied for both configurations, with a mean input value of 14.5 and 15.8 Nm respectively. Furthermore, the mean output torque for the two configurations is about 290 Nm and 330 Nm, guarantying the target of the gear ratio imposed during the design step. In addition, it can be seen the presence of a limited output torque ripple achieved by the Ferrite-based MaGT (approximately 3%) because of the higher equivalent air-gap in the inner rotor of S1 and S2 (air-gap + sleeve) compared to the NdFeB-based MaGT configuration: the latter is instead characterized by a much higher output torque ripple (approximately 10%).

All the other analytical and FEA results are resumed in Table III.4. Based on these, it can be stated that very low mismatches occur for the Ferrite-based MaGT configuration, as already shown in Figure III.27, which proves the effectiveness of the analytical models presented in this thesis.

In conclusion, although the NdFeB-based MaGT configuration presents lower volume and weight compared to the Ferrite-based solution, together with lower costs and higher maximum speed available, the choice of the Ferrite-based MaGT configuration could be justified by the low values of the magnetic flux density, which prevents magnetic saturation of the core materials. In addition, NdFeB PM presents very high eddy-current losses and higher torque ripple, thus reducing efficiency and performance of the MaGT, especially at high-speed operations.

Table III.4 – Analytical and FEA results achieved for the double-stage ferrite-based MaGT

Unit		***NdFeB-based***			***Ferrite-based***		
		Analytical	***FEA***	***err %***	***Analytical***	***FEA***	***err %***
$T_{II,S1}$	*Nm*	15.06	14.47	3.9	15.18	15.83	4.1
$T_{IV,S1}$	*Nm*	67.70	71.37	5.1	68.11	70.69	3.6
$T_{II,S2}$	*Nm*	70.47	63.67	9.6	71.99	68.38	5
$T_{IV,S2}$	*Nm*	320.60	290.42	9.3	325.52	336.84	3.3
$\sigma_\theta^{(s)}$ @ω_{max}	*MPa*	1646.5	1660	0.8	1912.4	1930	0.9
$p_i^{(m)}$ @ ω_{max}	*MPa*	16.5	16	3	16.8	18	6.6

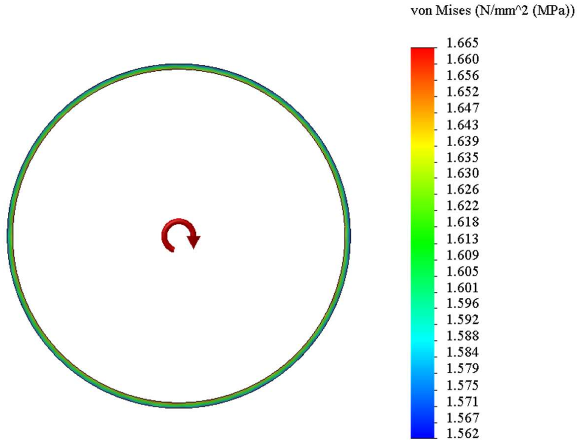

Figure III.16 - Tangential stress on the inner surface of the sleeve of the double-stage NdFeB-based MaGT at $\omega_{i,max}$.

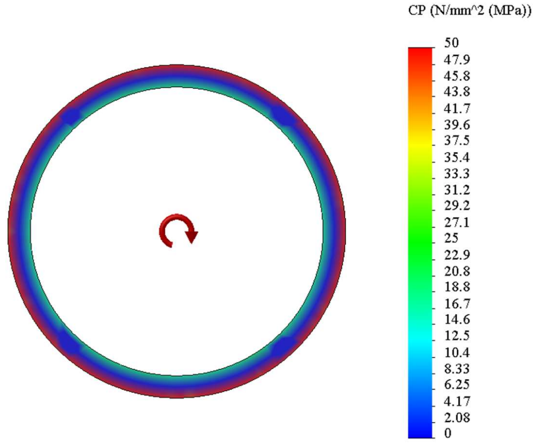

Figure III.18 - Contact pressure on the inner rotor surface of the inner PM ring of the double-stage NdFeB-based MaGT at $\omega_{i,max}$.

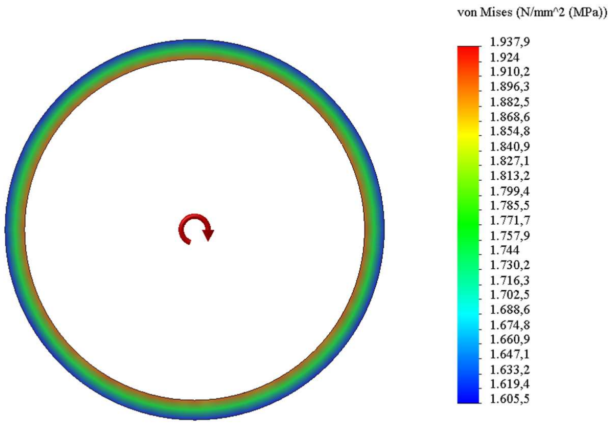

Figure III.17 - Tangential stress on the inner surface of the sleeve of the double-stage ferrite-based MaGT at $\omega_{i,max}$.

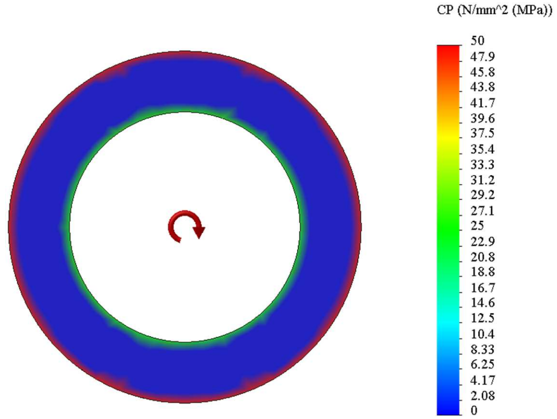

Figure III.19 - Contact pressure on the inner rotor surface of the inner PM ring of the double-stage ferrite-based MaGT at $\omega_{i,max}$.

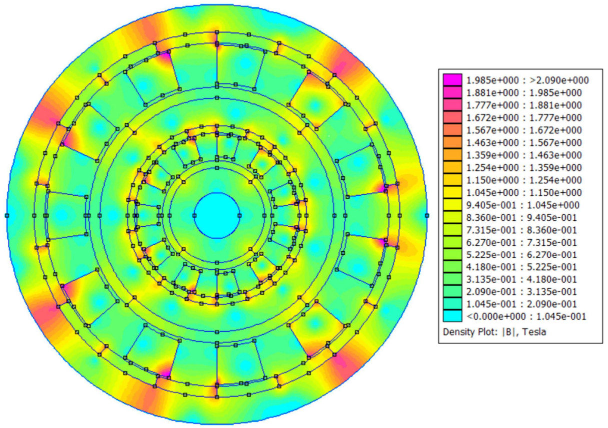

Figure III.20 - Magnetic flux density distribution of the double-stage NdFeB-based MaGT at no torque (magneto-static case).

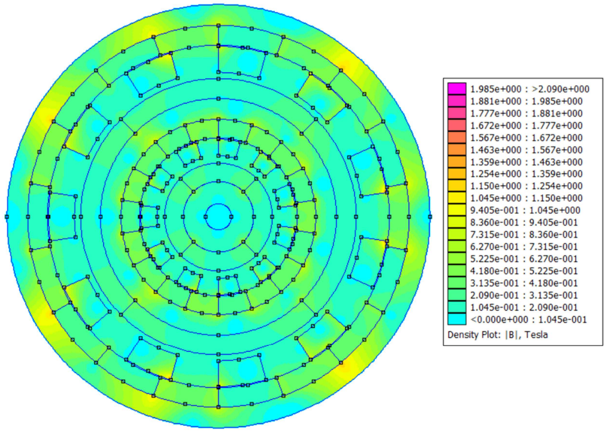

Figure III.21 - Magnetic flux density distribution of the double-stage ferrite-based MaGT at no torque (magneto-static case).

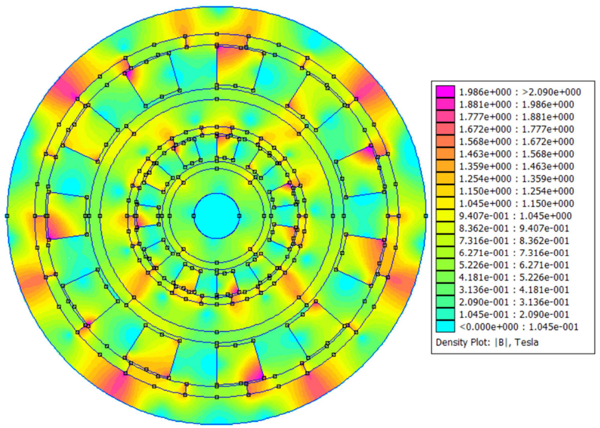

Figure III.22 - Magnetic flux density distribution of the double-stage NdFeB-based MaGT (magneto-static case) at maximum torque.

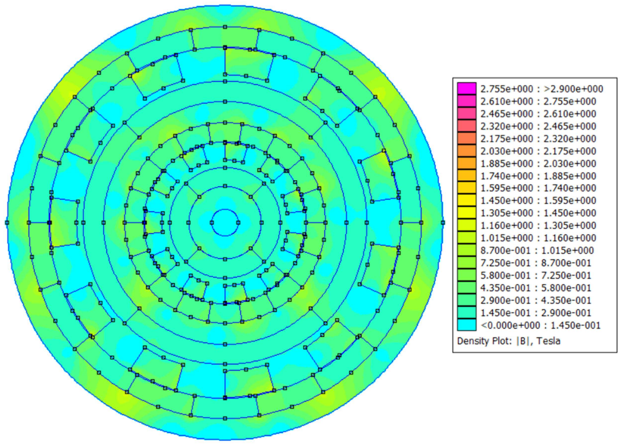

Figure III.23 - Magnetic flux density distribution of the double-stage ferrite-based MaGT (magneto-static case) at maximum torque.

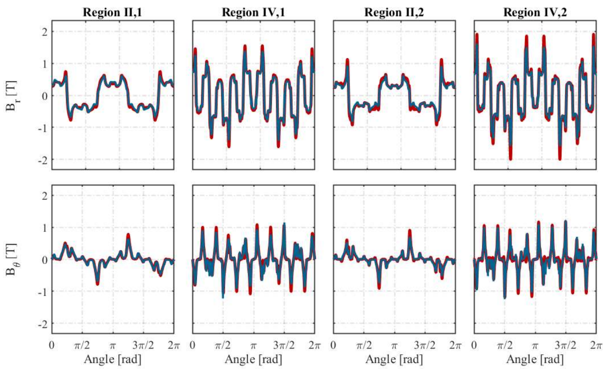

Figure III.24 - Analytical (red) and FEA (blue) evolutions of the magnetic flux density in the four air gaps of the double-stage NdFeB-based MaGT (magneto-static case) at no torque: radial (top) and tangential component (bottom).

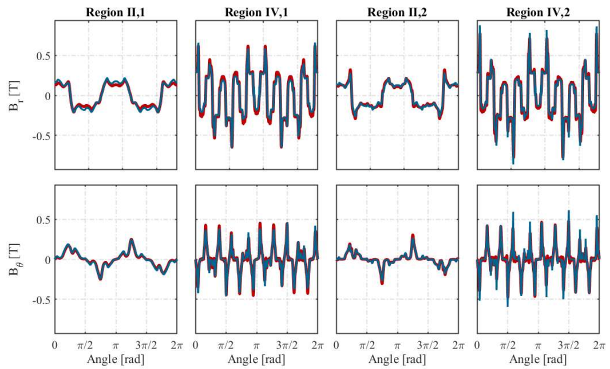

Figure III.25 - Analytical (red) and FEA (blue) evolutions of the magnetic flux density in the four air gaps of the double-stage ferrite-based MaGT (magneto-static case) at no torque: radial (top) and tangential component (bottom).

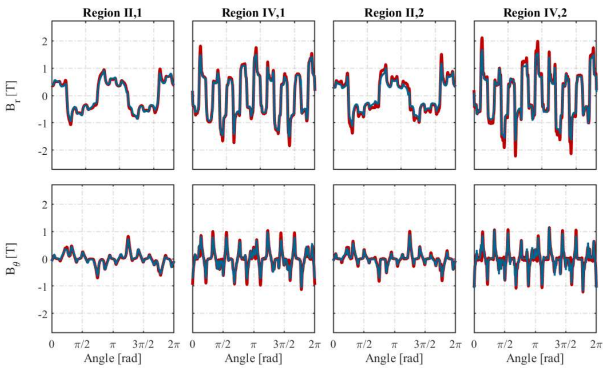

Figure III.26 - Analytical (red) and FEA (blue) evolutions of the magnetic flux density in the four air gaps of the double-stage NdFeB-based MaGT (magneto-static case) at maximum torque: radial (top) and tangential component (bottom).

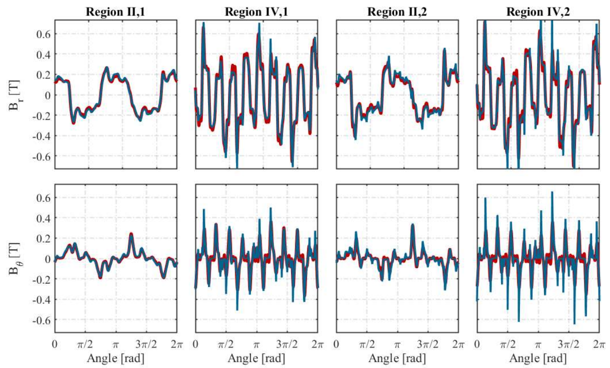

Figure III.27 - Analytical (red) and FEA (blue) evolutions of the magnetic flux density in the four air gaps of the double-stage ferrite-based MaGT (magneto-static case) at maximum torque: radial (top) and tangential component (bottom).

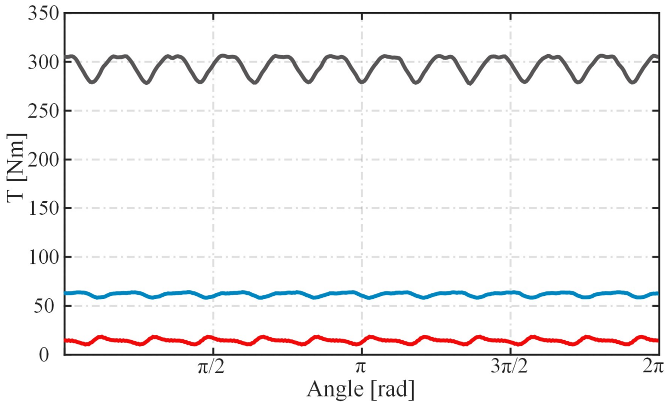

Figure III.28 - Torque distribution with the rotor position for the NdFeB-based MaGT configuration: inner rotor (red), middle rotor (blue), outer rotor (black).

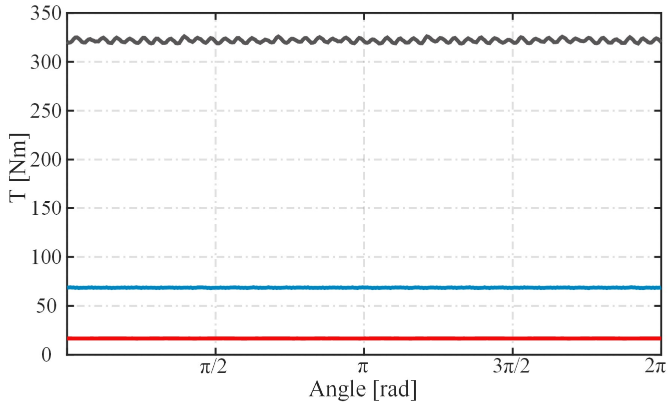

Figure III.29 - Torque distribution with the rotor positions for the Ferrite-based MaGT configuration: inner rotor (red), middle rotor (blue), outer rotor (black).

III.5 Double-stage MaGT optimization

III.5.1 Harmonic analysis of MaGT magnetic flux density distribution

For a coaxial MaGT, the torque transmission concept is based on the modulation of the magnetic flux density produced by the PMs through the ferromagnetic pole pieces interposed between the two rotors, which present different numbers of pole pairs. As a result, the overall magnetic flux density presents many harmonic components, some of which do not contribute to torque production and transmission. Furthermore, these components produce high eddy-current losses in the PMs and increased iron core losses, thus contributing to a possible PM demagnetization due to the generated heat and the resulting increased temperature. Eddy-current losses in the PMs could be reduced by using Ferrite PMs instead of NdFeB, due to their very low electrical conductivity. Furthermore, in order to reduce the iron losses, laminated iron steel for the iron parts of MaGT is generally suggested. However, in high-speed applications, in which the frequency of the magnetic flux density in the iron parts could be greater than 1 kHz, high iron losses would occur, even by using laminated steel. Based on the previous considerations, there is the need of reducing the harmonic content of the magnetic flux density of MaGT to the maximum extent, especially those components that do not give any contribution to the torque production and transmission.

In this regard, a detailed analysis that aims to identify the solutions for reducing the harmonic content of the magnetic flux density occurring in the designed double-stage ferrite-based MaGT is presented in this section. In particular, the NdFeB-based configuration analysed in the previous section has not been considered further because of the higher PM losses foreseen for that configuration. Additionally, pole arc to pole pitch ratios of the two rotors and of the modulation ring can be tuned suitably in order to reduce the harmonic content of the magnetic flux density.

Figure III.30 shows the harmonic spectrum (in per unit) of the magnetic flux density distribution in the modulation ring of the double-stage ferrite-based MaGT configuration designed in the previous section (p_i = 2, p_o = 9), which is characterized by a unity pole arc to pole pitch ratio of both inner and outer rotors ($\alpha_{i,o}$ = 1) and a pole arc to pole pitch ratio of the modulation ring (β) equal to 0.5. Particularly, Figure III.30 is achieved by considering both the contributions of the magnetomotive forces due to inner and outer PM rotors by the superposition of (V.8) and (V.15) presented in section III.1. The figure reveals several harmonic components different from the fundamentals (2nd and 9th harmonic components), some of which do not contribute to the torque transmission. In particular, the 6th, 10th, 13th, 20th and 27th harmonic components present the highest amplitude, as red-highlighted in Figure III.30.

The reduction of these undesired harmonic components can be obtained by the variation of α_i, α_o and β. In this regard, Figure III.31 highlights the evolutions of the amplitude of some of these harmonic components with α_i, α_o and β alternatively; this means that, for example, the first picture shows the variation of the 2nd, 6th and 10th harmonic component amplitudes with α_i, while α_o and β are set constant at 1 and 0.5 respectively. Similarly, the second picture shows the variation of the 13th and 20th harmonic component amplitudes with β, while α_i and α_o are both set constant at 1. The third graph instead highlights the variation of the 9th, 20th and 27th harmonic component amplitudes with α_o, while α_i and β are set constant at 1 and 0.5 respectively. Considering all these pictures, it can be noticed that a very low value of the amplitude of the 10th harmonic component is achieved for $\alpha_i = 0.80$.

Differently, when α_i is set at 0.65, a very low value of the 6th harmonic component amplitude occurs. Similar considerations can be made by varying α_o, particularly when α_o is set at 0.65, a very low amplitude of the 27th harmonic component is reached. However, it is worth noting that low values of α_i and α_o produce also a decrease of the 2nd and 9th harmonic component amplitudes, which reduces the torque transmission capability. Regarding β, its variation within 0.2 and 0.8 does not allow a high reduction of the 13th and 20th harmonic components, as still shown in Figure III.31. However, it is clear that the variation of β influences the modulation effect exerted by the ferromagnetic pole pieces; this is proved by the fact that, when β equals 0 or 1, no modulation effect is provided and, consequently, no torque transmission occurs. This can be seen in Figure III.32, in which the variation of the amplitude of the 2nd and 9th harmonic components with β is highlighted, by considering only the modulated part of B_o and B_i, namely B_{m_o} and B_{m_i}: the latter interact with the fundamental parts B_{f_i} and B_{f_o} to enable the MaGT torque, as pointed out in section III.1.

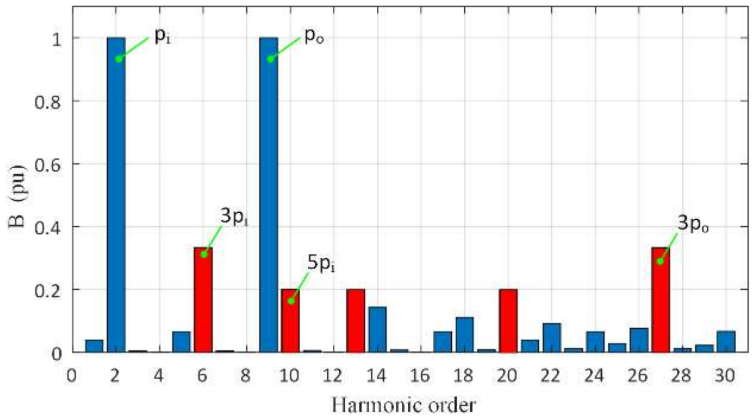

Figure III.30 - Harmonic spectrum of the magnetic flux density distribution in the modulation ring of the designed double-stage ferrite-based MaGT ($p_i = 2$, $p_o = 9$).

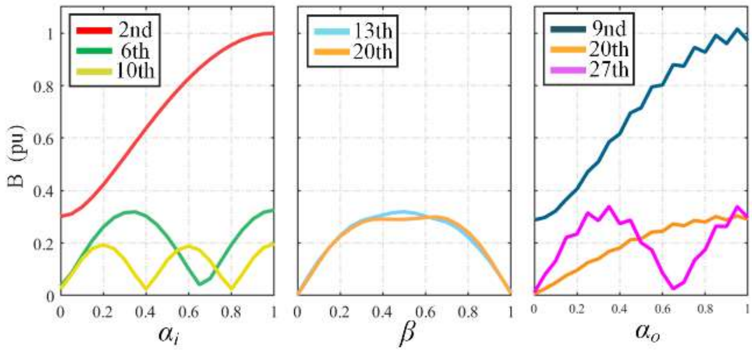

Figure III.31 - Evolution of the amplitudes of different harmonic components of the magnetic flux density in the inner air gap of the double-stage ferrite-based MaGT with the parameters α_i, β and α_o.

In conclusion, based on Figure III.31 and Figure III.32, it can be stated that α_i and α_o should be chosen in the range 0.65-0.8, while β can be set at a value between 0.4 and 0.6 in order to reduce the harmonic content of the magnetic flux density of the designed double-stage ferrite-based MaGT, thus optimizing its preliminary performances shown and discussed in section III.6. However, a proper performance assessment requires computing overall losses and efficiency of the MaGT, as detailed in the following section.

III.5.2 Losses and efficiency computation

MaGT is characterized by iron core losses in the high-speed rotor (P_{loss_i}), in the low-speed rotor (P_{loss_o}) and in the pole pieces of the modulation rings (P_{loss_pp}). The overall losses in the iron parts can be achieved as:

$$P_{loss} = P_{loss\_i} + P_{loss\_o} + P_{loss\_pp}\,. \tag{V.50}$$

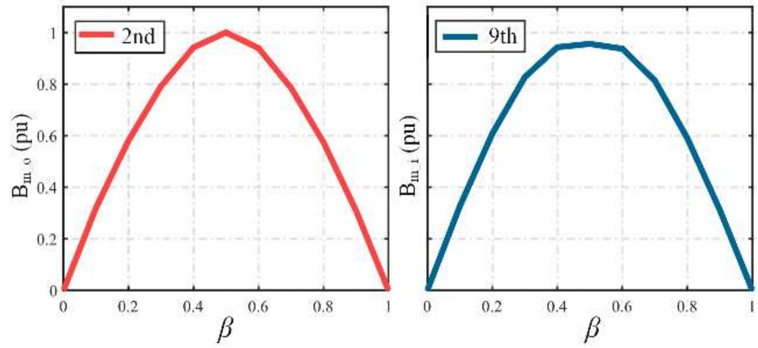

Figure III.32 - Evolution of the modulated part of the 2nd and 9th harmonic components of the MaGT magnetic flux distribution with the parameter β: modulation part due to PM outer rotor on the left; modulation part due to PM inner rotor on the right.

The losses evaluation can be made by post-processing the electromagnetic FEA results, which are achieved by means of the software FEMM, through the use of the MATLAB script provided by [60]. Particularly, the Improved General Steinmetz Equation (IGSE) method is applied. The analysis consists of the evaluation of the magnetic flux density value in multiple points of the iron parts, which represent the centre points of the mesh elements. The post-processor saves the values of the magnetic flux density at each point for different rotor positions in order to obtain the periodic evolution of the magnetic flux density in each mesh point with the rotor position.

The computation of (V.50) with the IGSE model requires just the knowledge of the frequency of the magnetic flux density in each MaGT iron part and the Steinmetz coefficients of the material. The frequency f_{el} in each part of the MaGT can be evaluated from (V.21) as:

$$f_{el} = \frac{\omega_i}{2\pi} p_i = \frac{p_o}{p_i} \frac{\omega_o}{2\pi} p_i = \frac{\omega_o}{2\pi} p_o \,. \tag{V.51}$$

Particularly, (V.51) defines the frequency of the magnetic flux density in the outer air gap accounting for the modulation effect. Thus, based on (V.51), it is clear that the inner rotor, the outer rotor and the ferromagnetic pole pieces exhibit the same frequency f_{el}. The Steinmetz coefficients of the material can be determined by a simultaneous curve fitting of the manufacturer's data for different frequencies using the general Steinmetz equation:

$$P_{iron\_loss} = k_e f^a \hat{B}^b \tag{V.52}$$

where P_{iron_loss} is the average power loss density for a sinusoidal waveform given by datasheet, which is a function of the excitation frequency f of the sinusoidal signal, of the peak value of the magnetic flux density ($\hat{B}$) and of the Steinmetz coefficients k_e, a and b. The values obtained by applying the IGSE model thus represent the loss density of each point (W/m^3). Consequently, the losses of the mesh element can be computed by the product between the loss density of each point and the corresponding element volume. The total losses are finally obtained by the sum of all element losses.

Once the overall losses have been determined, the MaGT efficiency can be achieved as:

$$\eta = \left(1 - \frac{P_{loss}}{P_n}\right) \cdot 100 \tag{V.53}$$

in which P_n is the rated power of the MaGT.

III.5.3 MaGT optimization results

Referring to the double-stage ferrite-based MaGT presented in section III.6 (first case in the following), the analytical and numerical formulations described in the previous sections have been employed for optimizing its design (second case in the following). In particular, based on both Figure III.31 and Figure III.32, the values of the parameters α_i, α_o and β have been set optimally, as shown in Table III.5. Figure III.33 highlights the comparison between the two cases in terms of per unit harmonic spectra of the radial component of the magnetic flux density in the inner and outer air gaps of the MaGT S1, which are computed by 2D FEA using the FEMM software. The figure shows that, in the second case, the 10th harmonic component completely disappears and the amplitude of the 6th and 27th harmonic components are reduced by more than 10% and 25% respectively compared to the first case. Furthermore, the amplitude of the fundamental harmonic components (the 2nd in the inner air gap and the 9th in the outer air gap) presents a value fairly close to that achieved in the first case, thus guaranteeing similar performances in terms of maximum torque capability. Furthermore, also the amplitudes of the 13th, 14th, 17th and 20th harmonic components are decreased in the second case compared to the first.

III.5.3.1 Iron losses results

The evolution of the estimated iron losses with the outer rotor speed in the different iron parts achieved for the second case are shown in Figure III.34, which are computed according to the method described in subsection III.5.2. These losses are evaluated at rated torque (12.7 Nm) and for different speeds of the outer rotor. Regarding the iron material, the Silicon laminated steel M235-35A manufactured by Sura has been selected because of its very low specific losses at different frequencies. The main properties of this material are reported in Table III.6. It can be seen in Figure III.34 that the losses increase highly with the rotor speed, especially in the outer iron yoke and in the pole pieces of the MaGT S1, in which the frequency is very high (up to 1 kHz). Furthermore, the S2 of the MaGT presents much lower losses than the S1 due to its lower frequency, as expected. By comparing the results presented in Table III.7 to each other, it can be noticed that the second case exhibits lower overall losses (–16%) than the first case, thus guaranteeing improved efficiency, as shown in Figure III.35.

Table III.5 - MaGT geometric parameters

Description	***Value***		
Parameter	***Symbol***	***1st case***	***2nd case***
Inner rotor pole arc-pitch ratio	α_i	1	0.8
Outer rotor pole arc-pitch ratio	α_o	1	0.7
Pole pieces pole arc-pitch ratio	β	0.5	0.6

Table III.6 - M235-35A main technical data

Description	***Unit***	***Value***
Mass density	kg/m^3	7600
a (Steinmetz parameter)	-	1.53
b (Steinmetz parameter)	-	2.02
k_e (Steinmetz parameter)	W/kg	0.0018

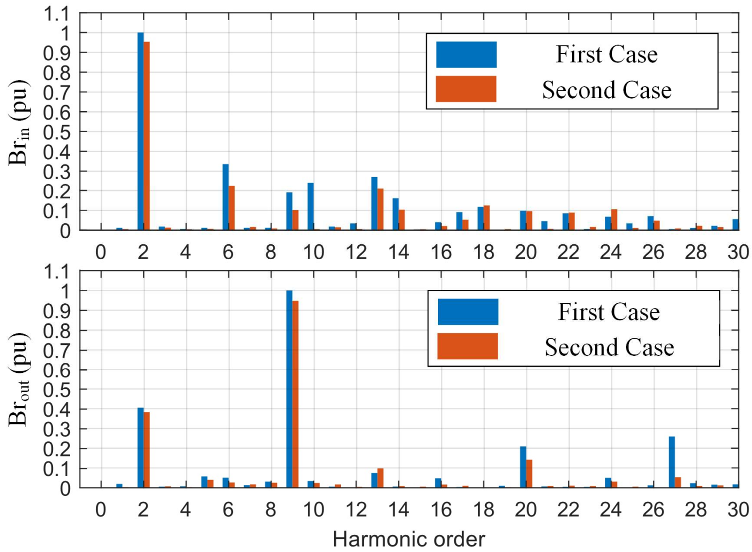

Figure III.33 - Harmonic spectra of the radial component of the magnetic flux density in the inner air gap (top) and outer air gap (bottom) of the S1 of the preliminary and improved double-stage ferrite-based MaGT configurations.

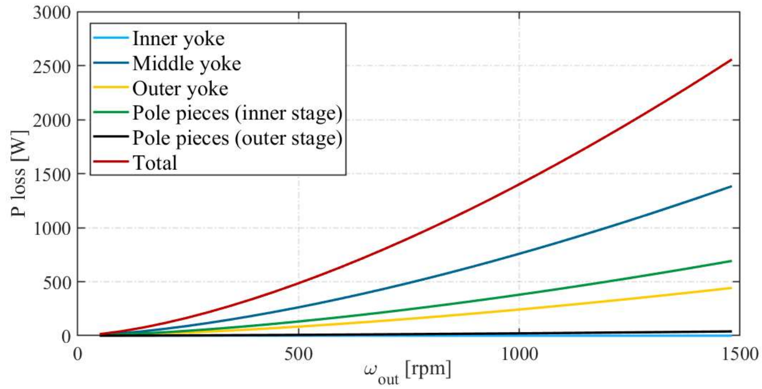

Figure III.34 - Evolution of the iron losses in the iron parts with the outer rotor speed for the double-stage ferrite-based MaGT (second case).

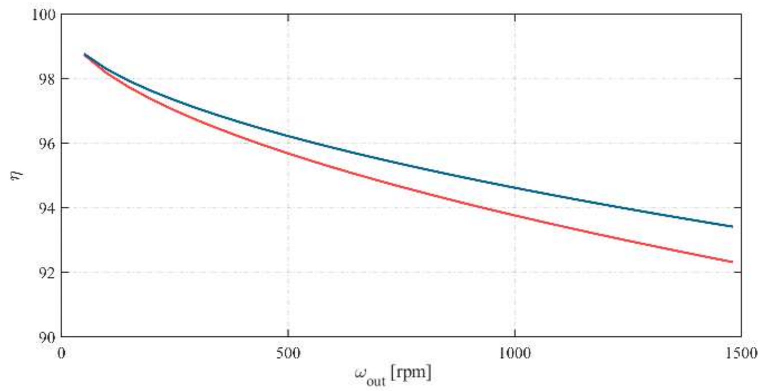

Figure III.35 - Evolution of the efficiency with the outer rotor speed for the double-stage ferrite-based MaGT: first case (red) and second case (blue).

Table III.7 - Losses comparison at the outer rotor maximum speed

Description		***Losses [W]***	
Parameter	***Symbol***	***1st case***	***2nd case***
Inner yoke	P_{loss_in}	15	8
Middle yoke	P_{loss_m}	1723	1384
Outer yoke	P_{loss_o}	448	442
Pole pieces S1	$P_{loss\_pp\_S1}$	847	692
Pole pieces S2	$P_{loss\_pp\_S2}$	48	39
Total	P_{loss}	3081	2565

III.5.3.2 Thermal analysis results

The distribution of temperature in each part of the double-stage ferrite-based MaGT for both the first and second case have been computed and compared to each other in order to validate the optimization of the double-stage ferrite-based MaGT proposed in the previous section. The same boundary conditions are used in both cases in order to enable a consistent comparison. In this regard, the natural and forced convection coefficients in the simulations are set at 10 W/(m^{2}K) and 100 W/(m^{2}K), respectively. Furthermore, the thermal conductivity coefficients for the different materials used in the simulations are set according to Table III.8, while the environmental temperature is set at 25 °C.

The simulations are carried out at the maximum torque (12.7 Nm) and at the inner rotor speed of 30 krpm by considering the power losses listed in Table III.7. Considering both Figure III.36 and Figure III.37, it is worth noting that the inner air gap of each case presents a higher thickness compared to the outer air gap due to the presence of a carbon fibre sleeve. These figures show that the main sources of heat for both cases are localized in the middle yoke and in the pole pieces of the S1. The maximum temperature is reached in the inner pole pieces and its value is approximately 115 °C for the first case and 95 °C for the second case. Such a large difference is mainly due to the lower losses characterizing the second case. In addition, the reduction of pole arc to pitch ratio of the PMs implemented in the second case means more iron yoke subject to air forced convection, which increases the heat dissipation in this part of MaGT, thus further decreasing the overall temperature.

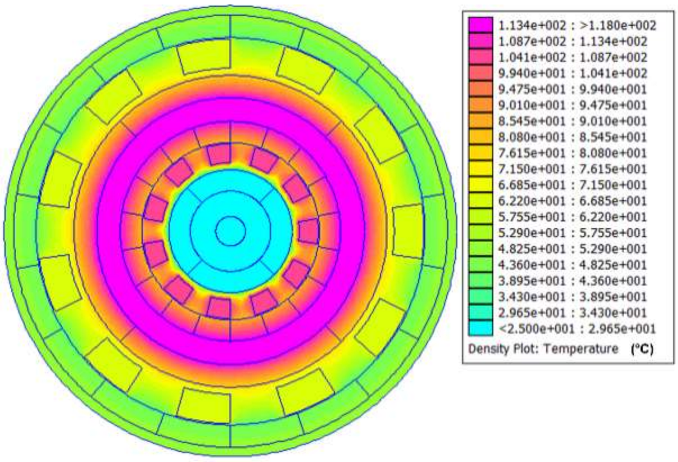

Figure III.36 - Temperature distribution achieved for the double-stage ferrite-based MaGT configuration at maximum torque and rated speed (first case).

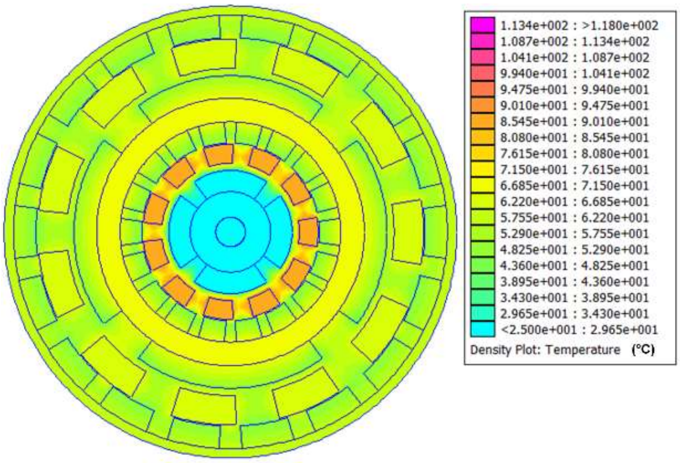

Figure III.37 - Temperature distribution achieved for the double-stage ferrite-based MaGT configuration at maximum torque and rated speed (second case).

Table III.8 - Material properties for thermal simulations

Material	***Thermal Conductivity [W/(mK)]***
Iron Steel	30
Ferrite Magnet	3

III.6 Simulation of the designed HS-EPS

In order to investigate the performance of the HS-EPS designed in this thesis, it has been modelled and simulated in MATLAB-Simulink using the SimDriveline Library, as already done for the other EPS configurations considered in Chapter 1. The HS-EPS consists of the HS-PMSM designed in Chapter 2, which is coupled with the optimised double-stage ferrite-based MaGT designed in Chapter 3; HS-PMSM and MaGT main parameters are reported in Table III.9 and Table III.10 respectively. Furthermore, vehicle main parameters are summarized again in Table III.11, which are the same already considered for all the cases analysed in Chapter 1. Similarly, the EPS overall efficiency has still been computed by means of (III.5), which is reported also in the following:

$$\eta_{EPS} = \eta_b \, \eta_c \, \eta_m \, \eta_t \qquad \text{(III.5)}$$

where η_b, η_c, η_m and η_t are the efficiencies of ESS, power electronic converters, EM and TS respectively. It is worth reminding that both η_b and η_c in (III.5) are assumed constant at 0.9, which should represent a reasonable and precautionary estimation. Furthermore, η_m is determined in accordance with suitable look-up tables, which have been computed by considering advanced modelling and vector control strategies of Permanent Magnet Brushless DC machine that guarantee an appropriate MTPA operation [61], [62]. In this regard, two different vector control approaches have been followed, which refer to different synchronous reference frames; one is developed in the *ft* reference frame [61], [63], which guarantees constant torque operation but a limited CPSR due to a relatively high voltage demand (*Case 4a*). The second approach refers instead to the $\varphi\tau$ reference frame [61], which guarantees a much wider CPSR but at the cost of some torque ripple (*Case 4b*). In both these cases, core losses have been modelled in accordance with the suggestions made for Permanent Magnet Brushless AC machine [64], namely by introducing suitable equivalent resistances in parallel with the back-emf voltage sources and whose values have been set in accordance with the core losses estimations achieved by FEA.

Regarding η_t, it has been estimated by considering the double stage MaGT efficiency evaluation obtained in previous subsection and reported in Figure III.35. It worth noting that the MaGT efficiency has been assumed constant and equal to 0.98 for the *Case 3* analysed and discussed in Chapter 1 (HS-PMSM with wide CPSR coupled with MaGT

Table III.9 - Designed HS-PMSM rated and maximum values

	Symbol	Unit	Value
Rated Power	P_n	kW	40
Rated Torque	T_n	Nm	12.7
Rated Speed	$\omega_{m,n}$	krpm	30
Maximum Speed	$\omega_{m,max}$	krpm	100

Table III.10 – Designed Double Stage ferrite-based MaGT parameters

Parameter	Symbol	Unit	Value
MaGT ratio	τ_{MaGT}	-	20.5
Final ratio	τ_{SGT}	-	4.2
MaGT efficiency	η_{MaGT}	%	0.99÷0.90

Table III.11 - Vehicle main parameters

Parameter	Symbol	Unit	Value
Base speed	V_b	km/h	36.5
Design maximum speed	V_{max}	km/h	125
Maximum gradeability (@ V_b)	α_{max}		30
Vehicle mass	m_v	kg	1130
Frontal area	A_f	m^2	2.06
Drag coefficient	C_d	-	0.29
Friction coefficient	C_{roll}	-	0.006
Wheel radius	r_w	m	0.28

and SGT), whereas it has been assumed more appropriately variable with the rotational speed in these new cases.

Simulation results achieved in *Case 4a* are presented in Figure III.38, which show the operating points of the designed HS-PMSM on the (ω_m,T_m) plane over each driving cycle. Furthermore, the overall energy consumptions are shown in Table III.12, while the HS-EPS overall losses are summarized in Table III.13. In particular, the results obtained for this new *Case 4a* has been compared with *Case 1* (LS-PMSM with wide CPSR and SGT) and *Case 3* (HS-PMSM with wide CPSR coupled with MaGT and SGT), both already analysed in Chapter 1. In this regard, the *Case 1* has still been assumed the reference case,

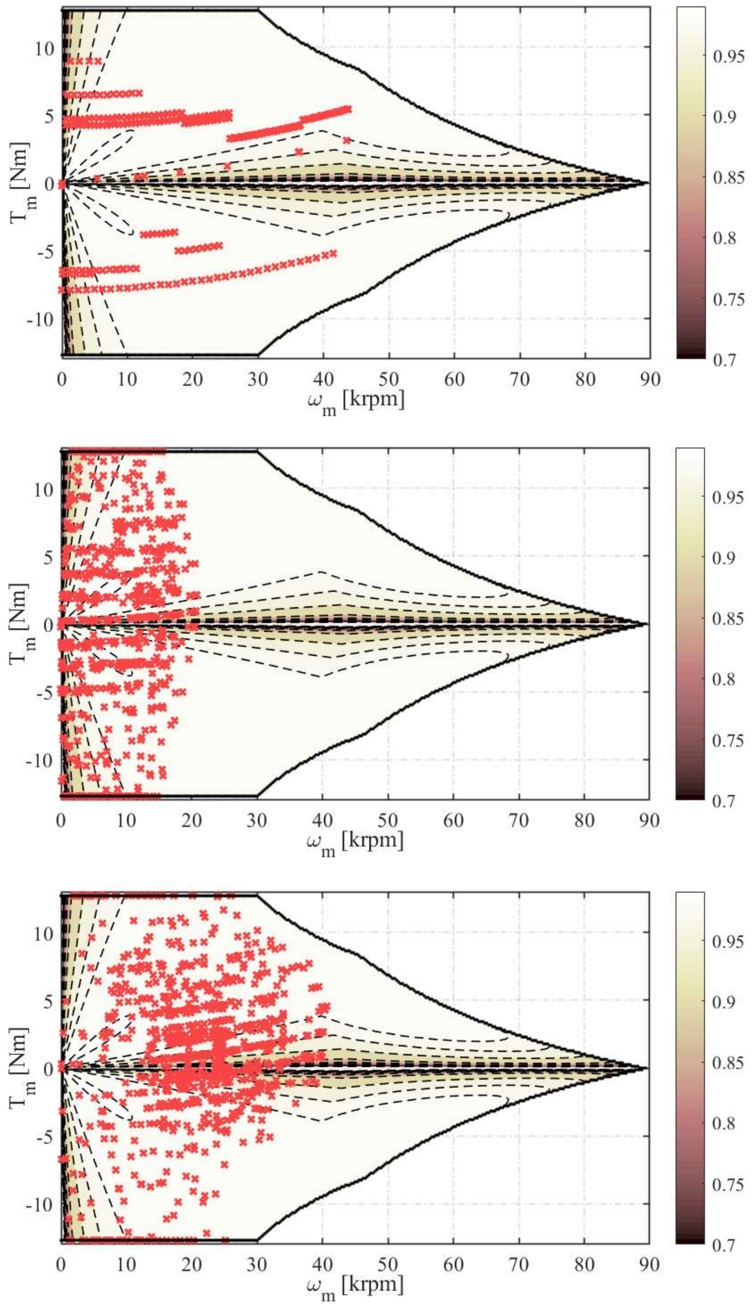

Figure III.38 – Operating points achieved over NEDC (up), ArtUrban (middle), ArtRoad (bottom), together with the HS-PMSM efficiency map (colormap) achieved for *Case 4a*.

as done in Chapter 1, while *Case 3* is the only one that concerns a HS-EPS. For these reasons, *Case 2* has not been considered further for this final comparison. In addition, Figure III.38 shows that the maximum operating speed of the designed EM has been limited to 45 krpm; this is because the CPSR of the designed HS-PMSM achievable in *Case 4a* goes from 30 krpm ($\omega_{m,n}$) to 45 krpm. Consequently, due to such a narrow CPSR, an additional SGT with a gear ratio of 1.8 is needed in order to guarantee the designed maximum speed of the vehicle reported in Table III.11.

Table III.12 - Overall energy consumption

Cycle		***Case 1 (Wh)***	***Case 3 (Wh)***	***Case 4a (Wh)***
NEDC	*Overall energy*	1247	1197	1093
	Total Losses	260	220	180
	Cycle Efficiency	79%	81%	83.5%
ArtUrban	*Overall energy*	750	742	674
	Total Losses	94	88	62
	Cycle Efficiency	87%	88%	91%
ArtRoad	*Overall energy*	2125	2061	1966
	Total Losses	350	295	258
	Cycle Efficiency	84%	86%	87%

Table III.13 - EPS losses

Cycle & Case		***EM losses [Wh]***	***TS Losses [Wh]***	***Total losses [Wh]***
NEDC	*1*	196 (75.3 %)	64 (24.7 %)	260
	3	139 (62.5 %)	83 (37.5 %)	222
	4a	101 (56.1%)	79 (43.9%)	180
ArtUrban	*1*	75 (79.9 %)	19 (20.1 %)	94
	3	54 (61.4 %)	34 (38.6 %)	88
	4a	26 (41.9%)	36 (58.1%)	62
ArtRoad	*1*	281 (80.3 %)	69 (19.7 %)	350
	3	191 (64.7 %)	104 (35.3 %)	295
	4a	123 (47.6%)	135 (52.4%)	258

Focusing on the NEDC cycle at first, it can be seen that *Case 4a* exhibits very good performance in terms of energy consumption compared to the other cases. This is due to the optimal trade-off between EM and TS losses. In particular, high performances are guaranteed due to the location of the HS-PMSM operating points, which corresponds to very high efficiency values, thus guaranteeing much lower EM losses, especially compared to *Case 1*.

Similar considerations apply to ArtUrban and ArtRoad driving cycle, which are characterized by rapid accelerations and braking. In particular, very good performance are achieved in *Case 4a* also over these driving cycles, which shows the competitiveness of the designed HS-EPS, especially if compared to *Case 1* (LS-PMSM with wide CPSR and SGT). Regarding MaGT, slightly higher losses are achieved in *Case 4a* compared to *Case 3*; however, it is worth reminding that *Case 3* is characterized by an MaGT with a constant and very high efficiency values (0.98), whereas the proposed HS-EPS refers to the more accurate MaGT losses assessment presented in the previous sections.

However, due to the narrow CPSR achieved, the choice of the single gear transmission system (MaGT + SGT) adopted in *Case 4a* presents some issues. In particular, a maximum gradeability of 13% is achieved to guarantee the designed vehicle maximum speed of 125 km/h, which is too low compared to the designed maximum gradeability of 30% at the base speed (Table III.11). This issues can be addressed by using a different vector control strategies of Permanent Magnet Brushless DC machine that refers to a different synchronous reference frame ($\varphi\tau$ instead of ft), leading to much wider CPSR (*Case 4b*) The results obtained for this new case are shown in Figure III.39, which highlights the operating points of the designed HS-PMSM on the (ω_m,T_m) plane over each driving cycle. It can be seen that, in this new case, the designed HS-PMSM presents a wide CPSR (beyond 90 krpm), which guarantee a very wide speed range of the vehicle. However, the maximum operating speed of the HS-PMSM has been limited to 60 krpm in accordance with the maximum operating speed achieved for the designed MaGT (Figure III.15). As a result, *Case 4b* guarantees higher vehicle performance than *Case4a*, especially in terms of maximum acceleration and gradeability.

In conclusion, a comparison between the overall energy consumptions and losses achieved in *Case 4a* and *Case 4b* over the considered driving cycle is reported in Table III.14 and Table III.15. It can be seen that the overall energy consumption for the two

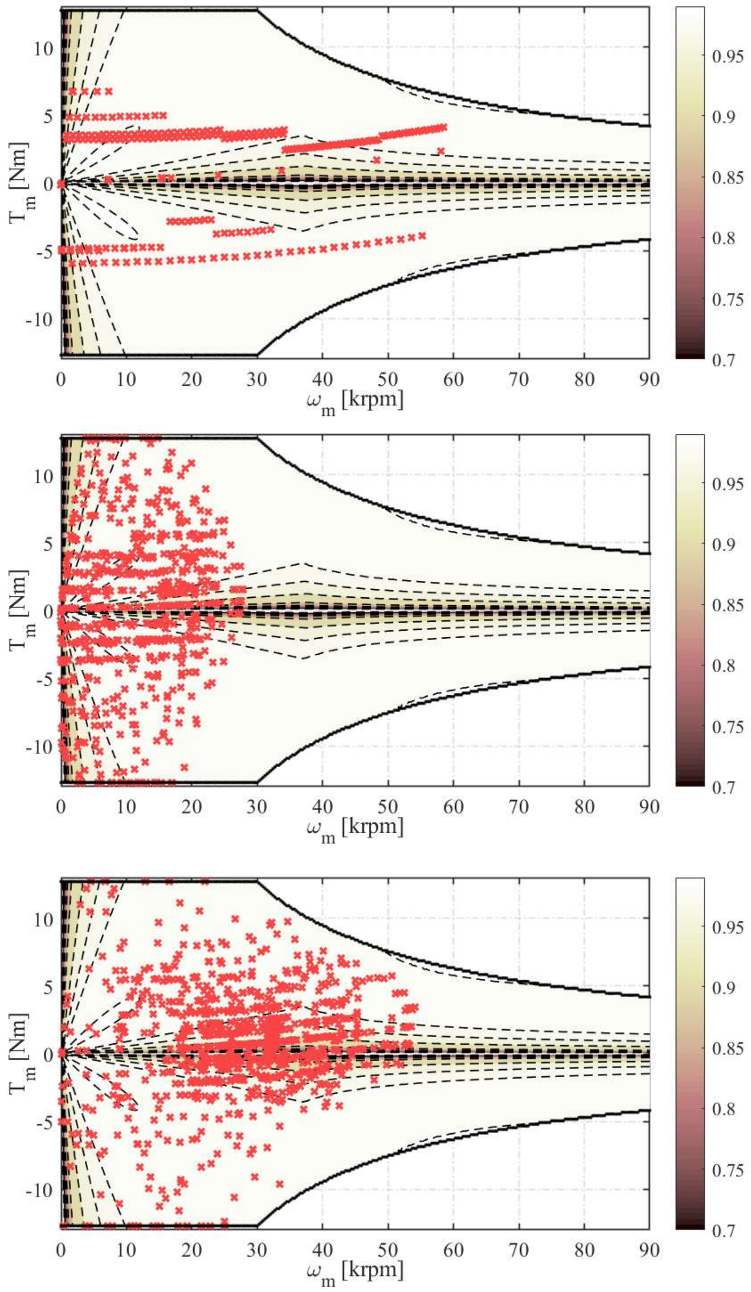

Figure III.39 – Operating points achieved over NEDC (up), ArtUrban (middle), ArtRoad (bottom), together with the HS-PMSM efficiency map (colormap) achieved for *Case 4b*.

cases is similar, as well as the HS-EPS losses, thus guaranteeing similar overall efficiency. However, it can be noticed that *Case 4b* presents slightly higher TS losses over all the driving cycles; this is due to the higher HS-PMSM average operating speeds of *Case 4b*, which determine higher losses in the MaGT, as shown in Figure III.34. On the other hand, HS-PMSM losses for the two cases are very similar to each other over all the driving cycles due to the very large HS-PMSM operating region characterized by a very high efficiency value. As a result, although *Case 4b* presents a slightly worse performance than *Case 4a* in terms of efficiency, they are still superior than those achieved in *Case 1* and *Case 3*. Furthermore, since Case 4b addresses the issue of limited gradeability properly, it represents the most suitable choice among the different EPS solutions considered for this final comparison.

Table III.14 - Overall energy consumption

Cycle		***Case 4a (Wh)***	***Case 4b (Wh)***
NEDC	*Overall energy*	1093	1129
	Total Losses	180	192
	Cycle Efficiency	83.5%	83%
ArtUrban	*Overall energy*	674	676
	Total Losses	62	63
	Cycle Efficiency	91%	90.6%
ArtRoad	*Overall energy*	1966	1990
	Total Losses	258	270
	Cycle Efficiency	87%	86%

Table III.15 - EPS losses

Cycle & Case		***EM losses [Wh]***	***TS Losses [Wh]***	***Total losses [Wh]***
NEDC	*4a*	101 (56.1%)	79 (43.9%)	180
	4b	104 (54%)	88 (46%)	192
ArtUrban	*4a*	26 (41.9%)	36 (58.1%)	62
	4b	24 (38%)	39 (62%)	63
ArtRoad	*4a*	123 (47.6%)	135 (52.4%)	258
	4b	123 (45.5%)	147 (54.5%)	270

Conclusion

This PhD dissertation has presented the modelling and design of a novel High-Speed Electric Propulsion System (HS-EPS) for a light-duty vehicle. In particular, a comparison among different EPS configurations has been presented in Chapter I in order to investigate the competitiveness of HS-EPS for automotive applications. All the EPS solutions considered in that chapter have been tested by means of a simulation study, which is performed in MATLAB-Simulink. Particularly, an efficiency assessment has been carried out by referring to three driving cycles in order to highlight the most suitable EPS configuration over different driving conditions. The analysis has shown that a HS-EPS consisting of a High-Speed Permanent Magnet Synchronous Machine (HS-PMSM) with a wide constant-power speed range coupled with a Magnetic Gear Transmission (MaGT) is a competitive solution, especially if compared with low-speed PMSM. Its competitiveness could be even higher if weight reduction related to the employment of HS-PMSM is considered, which has not been addressed in this dissertation.

Based on this outcome, the design of a novel ferrite-based HS-PMSM suitable for automotive application has been carried out, which is presented and discussed in Chapter II. A mechanical and electromagnetic modelling has been considered at first, based on which a novel multi-parameter analytical design procedure has been developed with the aim of achieving a preliminary machine design that takes into account both design targets and constraints. The proposed design approach has been validated through extensive simulation studies, which have been performed by Finite Element Analyses (FEAs) that regard both mechanical and electromagnetic aspects. The comparison between analytical and FEA results reveals a very good agreement between them, although some minor differences occur; these are related mainly to the assumptions made for achieving a simplified electromagnetic model of the HS-PMSM. However, these differences do not impair the effectiveness of the proposed procedure, which aims at achieving a rapid preliminary HS-PMSM design.

Subsequently, in order to couple the designed HS-PMSM to vehicle wheels properly, the design and optimization of novel configurations of MaGT suitable for this specific application has been addressed, which is presented and discussed in Chapter III. Starting from mechanical and magnetic modelling, a single-stage ferrite-based MaGT is design at first through a multi-parameter analytical design procedure similar to that used for the HS-PMSM design. However, this MaGT does not fulfil all the design targets imposed by the HS-PMSM, especially in terms of maximum speed. Consequently, the design of two double-stage MaGTs have been considered, which are characterized by different PM materials. These are able to achieve greater maximum speed values, resulting in more suitable solutions for coupling the HS-PMSM with vehicle wheels. Additionally, an optimization analysis aimed at reducing the harmonic content of the magnetic flux density occurring in the designed Ferrite based double-stage MaGT has been carried out, together with the computational of both iron core losses and temperature distribution in each part of the designed MaGT. The results obtained through the analytical models have been validated by means of accurate FEAs by using the Solidworks and FEMM software. A number of comparisons among the designed MaGTs have been also performed and reported in detail, which highlight the effectiveness of all the proposed design solutions.

The last section of Chapter III presents a performance comparison among the designed HS-EPS and the solutions already considered and analysed in Chapter I. The corresponding results highlight the competitiveness of the designed EPS solution, especially in terms of efficiency. As a result, it can be stated that the research activities carried out during the PhD studies and reported in this dissertation reveals HS-EPS as a very promising solution for electric vehicles. However, some aspects should be investigated further, particularly an accurate cost assessment should be performed that must account for all the auxiliary components required by high-speed operations (magnetic bearings, containments, etc.).

Appendix

A Mechanical analytical model

In subsection (II.1.1) and (III.2.2) a mechanical model has been introduced in order to determine both radial σ_r and tangential σ_θ stresses acting on the rotor in the HS-PSMS and in the MaGT. This model has been developed considering each rotor layer as a pressured rotating cylinder, which represents the base geometric structure of the rotor. The corresponding mathematical formulation based on the mechanical-elastic theory is reported in the following, which accounts for cylindrical symmetry and assumes a relative short axial length; consequently, the stress tensor acting on the rotor structure consists of just radial and tangential components (σ_r and σ_θ respectively) because the axial component (σ_z) can be considered negligible in the analytical mechanical model [32], [65].

A.1 Mechanical stress on generic cylinder

Referring to the schematic representation of a generic cylinder shown in Figure A.1, it could be assumed pressurized at $r = r_i$ and $r = r_o$, which represent the inner and outer radius of the cylinder, and rotating at the rotational speed ω: both these assumptions mean that the cylinder is subjected to internal stress. Equation Chapter 1 Section 1

In this regard, it is assumed that the shear stresses can be neglected due to symmetry; therefore, the internal stress consists of radial and tangential components only.

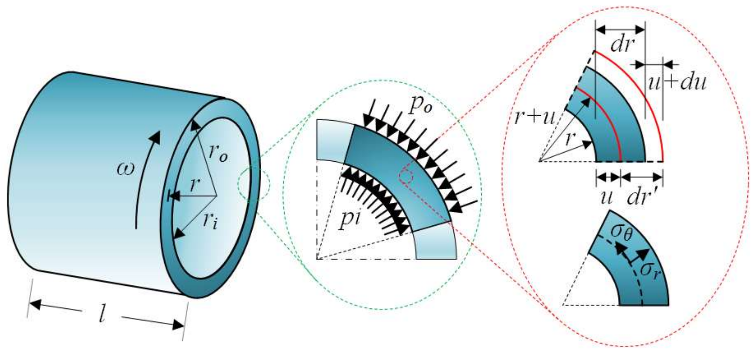

Figure A.1 - Representation of the rotating cylinder and of an its infinitesimal portion

Considering a generic infinitesimal portion of the cylinder, like the one shown in Figure A.1, the Hooke's Law for an orthotropic material can be expressed as:

$$\varepsilon_r = \frac{du_r}{dr} = \frac{1}{E_\theta}\left(k^2\sigma_r - \upsilon_\theta\sigma_\theta + E_\theta\alpha_r\Delta T\right) \tag{A.1}$$

$$\varepsilon_\theta = \frac{u_r}{r} = \frac{1}{E_\theta}\left(\sigma_\theta - k^2\upsilon_r\sigma_r + E_\theta\alpha_\theta\Delta T\right) \tag{A.2}$$

where ε_r and ε_θ are the tangential and radial strains due to the radial displacement u_r. Furthermore, σ_r and σ_θ denote the radial and tangential stresses, E_r and E_θ are the Young's modulus in the radial and tangential directions of the material, and υ_r and υ_θ are and Poisson's ratio in the radial and tangential directions respectively. Still referring to (A.1) and (A.2), α_r and α_θ are the thermal expansion coefficients in the radial and tangential direction of the material, which may determine additional strains depending on the difference between actual and environmental temperatures (ΔT). Furthermore, the parameter k occurring in (A.1) and (A.2) is expressed by:

$$k = \sqrt{\frac{E_\theta}{E_r}}\,. \tag{A.3}$$

Considering the volume of the infinitesimal portion of the cylinder ($r \cdot d\theta \cdot dr \cdot dz$), with a mass density ρ and constant rotating speed ω, the equation of motion in radial direction can be achieved as

$$\sum F_r = ma_r = \left(\rho r \cdot d\theta \cdot dr \cdot dz\right)\left(-r\omega^2\right) = -\rho\omega^2 r^2 \cdot d\theta \cdot dr \cdot dz\,. \tag{A.4}$$

In addition, by multiplying the stress by their respective area, the forces in the radial direction can be obtained as:

$$\sum F_r = (\sigma_r + d\sigma_r)(r + dr)d\theta dz - \sigma_r r d\theta dz - 2\sigma_\theta dr dz \sin\frac{d\theta}{2}. \tag{A.5}$$

By combining (A.4) with (A.5) the following equation is obtained:

$$\sigma_\theta = r\frac{d\sigma_r}{dr} + \sigma_r + \rho\omega^2 r^2 \tag{A.6}$$

in which the high-order term $d\sigma_r \cdot dr \cdot d\theta \cdot dz$ of (A.5) is neglected and sin($d\theta/2$) is approximated by $d\theta/2$ because $d\theta$ is infinitesimal. Differentiation of (A.6) with respect to r results in:

$$\frac{d\sigma_\theta}{dr} = r\frac{d^2\sigma_r}{dr^2} + 2\frac{d\sigma_r}{dr} + 2\rho\omega^2 r. \tag{A.7}$$

By solving equation (A.2) with respect to u_r and differentiating the result yields:

$$\frac{du_r}{dr} = \frac{1}{E_\theta}\left(r\frac{d\sigma_\theta}{dr} + \sigma_\theta - rk^2\upsilon_r\frac{d\sigma_r}{dr} - k^2\upsilon_r\sigma_r + E_\theta\alpha_\theta\Delta T + rE_\theta\alpha_\theta\frac{d\Delta T}{dr} \right). \tag{A.8}$$

By combining (A.1) and (A.8), the following relationship is achieved:

$$\begin{aligned} & r\frac{d\sigma_\theta}{dr} + \sigma_\theta + \upsilon_\theta\sigma_\theta - rk^2\upsilon_r\frac{d\sigma_r}{dr} - k^2\upsilon_r\sigma_r + \\ & + rE_\theta\alpha_\theta\frac{d\Delta T}{dr} - k^2\sigma_r - E_\theta\alpha_r\Delta T + E_\theta\alpha_\theta\Delta T = 0 \end{aligned}. \tag{A.9}$$

Then, by substituting (A.6) and (A.7) in (A.9) yields:

$$\begin{aligned} & r^2\frac{d^2\sigma_r}{dr^2} + \left(3 + \upsilon_\theta - k^2\upsilon_r\right) r\frac{d\sigma_r}{dr} + \left(1 - k^2 + \upsilon_\theta - k^2\upsilon_r\right)\sigma_r \\ & + \left(3 + \upsilon_\theta\right)\rho\omega^2 r^2 + E_\theta\left(r\alpha_\theta\frac{d\Delta T}{dr} - \alpha_r\Delta T + \alpha_\theta\Delta T \right) = 0 \end{aligned}. \tag{A.10}$$

In conclusion, considering the following relationship:

$$\frac{\upsilon_r}{E_r} = \frac{\upsilon_\theta}{E_\theta} \tag{A.11}$$

the following differential equation is achieved:

$$r^2\frac{d^2\sigma_r}{dr^2}+3r\frac{d\sigma_r}{dr}+\left(1-k^2\right)\sigma_r=-\left(3+\upsilon_\theta\right)\rho\omega^2r^2+ \\ -E_\theta\left(r\alpha_\theta\frac{d\Delta T}{dr}-\Delta T\left(\alpha_r+\alpha_\theta\right)\right). \tag{A.12}$$

In order to solve (A.12), the evolution of the temperature with radial displacement must be imposed. Therefore, a linear temperature distribution within the cylinder is assumed, as depicted in Figure A.2 and pointed out by the following equation:

$$\Delta T\left(r\right)=t_0+tr \tag{A.13}$$

where t_0 and t are defined as:

$$t=\frac{\Delta T_o-\Delta T_i}{r_o-r_i}\ ;\ t_0=\Delta T_o-\frac{\Delta T_o-\Delta T_i}{r_o-r_i}r_o \tag{A.14}$$

in which ΔT_o and ΔT_i are the difference between actual and reference temperatures in the inner and outer surface, respectively.

According to the superposition law, the general solution of (A.12) is the sum of the general solution σ_{r_0} and of a particular solution σ_{r_1}:

$$\sigma_r\left(r\right)=\sigma_{r\_0}+\sigma_{r\_1}. \tag{A.15}$$

In particular, σ_{r_0} is:

$$\sigma_{r\_0}\left(r\right)=c_1r^{k-1}+c_2r^{-k-1} \tag{A.16}$$

while σ_{r_1} can be achieved as:

$$\sigma_{r\_1}\left(r\right)=\frac{\left(3+\upsilon_\theta\right)\rho\omega^2r^2}{k^2-9}+\frac{E_\theta t\left(\alpha_r-2\alpha_\theta\right)}{4-k^2}r+\frac{E_\theta t_0\left(\alpha_r-\alpha_\theta\right)}{1-k^2}. \tag{A.17}$$

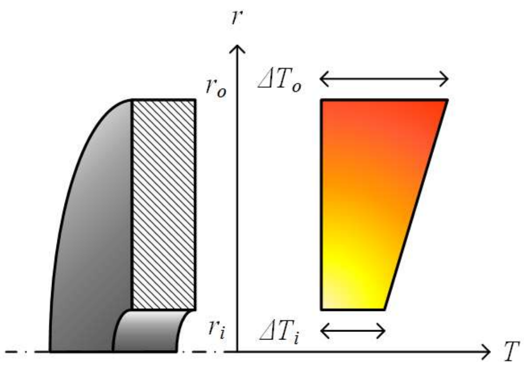

Figure A.2 - The cylinder temperature distribution.

Substituting (A.16) and (A.17) in (A.15), the distribution of radial stress in the cylinder is obtained:

$$\begin{aligned}\sigma_r(r) = c_1 r^{k-1} + c_2 r^{-k-1} - \frac{(3+\upsilon_\theta)\rho\omega^2 r^2}{9-k^2} + \\ - E_\theta\left(\frac{r(2\alpha_\theta-\alpha_r)t}{4-k^2} + \frac{(\alpha_\theta-\alpha_r)t_0}{1-k^2}\right)\end{aligned}. \tag{A.18}$$

Differentiating (A.18) and substituting the result and (A.18) in (A.6), the distribution of tangential stress in the cylinder is achieved:

$$\begin{aligned}\sigma_\theta(r) = kc_1 r^{k-1} - kc_2 r^{-k-1} - \rho\omega^2 r^2\left(\frac{3(3+\upsilon_\theta)}{9-k^2} - 1\right) + \\ - E_\theta\left(\frac{2r(2\alpha_\theta-\alpha_r)t}{4-k^2} + \frac{(\alpha_\theta-\alpha_r)t_0}{1-k^2}\right)\end{aligned} \tag{A.19}$$

in which c_1 and c_2 are arbitrary constants. The expressions of c_1 and c_2 can be obtained by imposing the following boundaries conditions:

$$\begin{aligned}\sigma_r(r_i) = p_i \\ \sigma_r(r_o) = p_o\end{aligned} \tag{A.20}$$

where p_i and p_o represent the internal and external pressure acting on the cylinder inner and outer surface, respectively. Substituting (A.20) in (A.19) results in:

$$\begin{cases} c_1 r_i^{k-1} + c_2 r_i^{-k-1} - \dfrac{(3+\upsilon_\theta)\rho\omega^2 r_i^2}{9-k^2} - \dfrac{E_\theta t(2\alpha_\theta-\alpha_r)}{4-k^2} r_i - \dfrac{E_\theta t_0(\alpha_\theta-\alpha_r)}{1-k^2} = p_i \\ c_1 r_o^{k-1} + c_2 r_o^{-k-1} - \dfrac{(3+\upsilon_\theta)\rho\omega^2 r_o^2}{9-k^2} - \dfrac{E_\theta t(2\alpha_\theta-\alpha_r)}{4-k^2} r_o - \dfrac{E_\theta t_0(\alpha_\theta-\alpha_r)}{1-k^2} = p_o \end{cases}. \tag{A.21}$$

Solving the linear system expressed by (A.21) yields:

$$\begin{aligned} c_1 = \frac{p_i\dfrac{r_o^{-k-1}}{r_i^{-k-1}} - p_o - \dfrac{(3+\upsilon_\theta)\rho\omega^2}{9-k^2}\left(r_o^2 - r_o^{-k-1}r_i^{3+k}\right)}{\left(r_i^{2k}r_o^{-k-1} - r_o^{k-1}\right)} + \\ + \frac{-\dfrac{E_\theta t(2\alpha_\theta-\alpha_r)}{4-k^2}\left(r_o - r_o^{-k-1}r_i^{k+2}\right) - \dfrac{E_\theta t_0(\alpha_\theta-\alpha_r)}{1-k^2}\left(1-\dfrac{r_o^{-k-1}}{r_i^{-k-1}}\right)}{\left(r_i^{2k}r_o^{-k-1} - r_o^{k-1}\right)}\end{aligned} \tag{A.22}$$

$$c_2 = \frac{p_i \frac{r_o^{k-1}}{r_i^{k-1}} - p_o - \frac{(3+\upsilon_\theta)\rho\omega^2}{9-k^2}\left(r_o^{\,2} - r_o^{\,k-1} r_i^{3-k}\right)}{\left(r_o^{\,k-1} r_i^{-2k} - r_o^{\,-k-1}\right)} + \\ + \frac{-\frac{E_\theta t(2\alpha_\theta - \alpha_r)}{4-k^2}\left(r_o - r_i^{2-k}\right) - \frac{E_\theta t_0(\alpha_\theta - \alpha_r)}{1-k^2}\left(1 - \frac{r_o^{k-1}}{r_i^{k-1}}\right)}{\left(r_o^{\,k-1} r_i^{-2k} - r_o^{\,-k-1}\right)}. \tag{A.23}$$

In conclusion, similar considerations can be made by considering an isotropic material. In this case, the following relationships can be used:

$$\begin{aligned} & k = 1 \\ & \upsilon_r = \upsilon_\theta = \upsilon \\ & E_r = E_\theta = E \\ & \alpha_r = \alpha_\theta = \alpha \end{aligned} \tag{A.24}$$

and the radial and tangential stress equation (A.18) and (A.19) become:

$$\sigma_r(r) = c_1 + \frac{c_2}{r^2} - \frac{(3+\upsilon)\rho\omega^2 r^2}{8} - \frac{tE\alpha}{3} r \tag{A.25}$$

$$\sigma_\theta(r) = c_1 - c_2 \frac{r}{r^2} - \frac{3(3+\upsilon)\rho\omega^2 r^2}{8} + \rho\omega^2 r^2 - 2\frac{tE\alpha}{3} r \tag{A.26}$$

in which the constant c_1 and c_2 are:

$$c_1 = \frac{p_i \frac{r_i^2}{r_o^{\,2}} - p_o - \frac{(3+\upsilon)\rho\omega^2}{8}\left(r_o^{\,2} - \frac{r_i^4}{r_o^{\,2}}\right) - \frac{Et\alpha}{3}\left(r_o - \frac{r_i^3}{r_o^{\,2}}\right)}{\left(\frac{r_i^2}{r_o^{\,2}} - 1\right)} \tag{A.27}$$

$$c_2 = \frac{p_i - p_o - \frac{(3+\upsilon)\rho\omega^2}{8}\left(r_o^{\,2} - r_i^2\right) - \frac{Et\alpha}{3}\left(r_o - r_i^2\right)}{\left(\frac{1}{r_i^2} - \frac{1}{r_o^{\,2}}\right)}. \tag{A.28}$$

B Magnetic analytical model

In subsection (III.2.1) a magnetic model has been introduced in order to compute the magnetic flux density distribution and torque in the MaGT. This model is based on the resolution of the Laplace and Poisson's equations in each subdomain of the MaGT in order to determine the distribution of the magnetic potential vector in two-dimensional polar coordinate plane in each subdomain using appropriate boundary conditions, as detailed in the following.

B.1 Problem description and assumptions

Considering the schematic representation of a Coaxial Magnetic Gear shown in Figure B.1, it consists of five different subdomains: the permanent magnet (PM) subdomains (Region I and V), the air-gap subdomains (Region II and IV) and the slot subdomain (Region III_j). The regions I, II, IV and V present a ring shape, while the region III_j present the shape shown in Figure B.1.

In order to compute the magnetic flux density distribution within all the regions previously defined, a magnetic potential vector in 2D polar coordinate system is taken into account. The following assumptions are considered:

- end effects are neglect;
- permeability of the iron is infinite;
- unity relative recoil permeability of the permanent magnets.

According to these assumptions, the magnetic potential vector *A* presents only the z-axis component and it depends on the polar coordinates *r* and *θ*. Hence, the following notations are used:

$$\begin{aligned}
A_I &= A_I\left(r,\theta\right)\cdot e_z \\
A_{II} &= A_I\left(r,\theta\right)\cdot e_z \\
A_{III_i} &= A_{III_i}\left(r,\theta\right)\cdot e_z \\
A_{IV} &= A_{IV}\left(r,\theta\right)\cdot e_z \\
A_V &= A_V\left(r,\theta\right)\cdot e_z
\end{aligned} \tag{B.1}$$

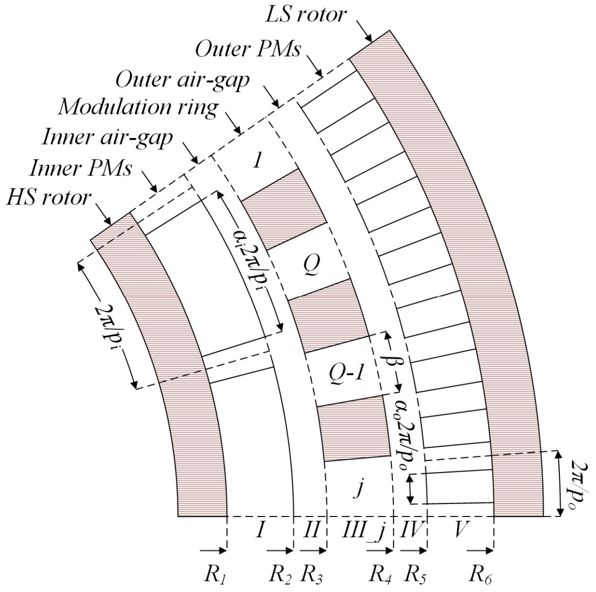

Figure B.1 - Coaxial Magnetic Gear general configuration.

where e_z represents the unity z-axis vector. Therefore, considering each subdomain, the solution of a partial differential equation must be obtained in order to achieve the corresponding A distribution, which also requires setting the boundary conditions properly. By using the variables separation method, the solution of Laplace's equation can be considered for slot and air gap subdomains, while the Poisson's equation is taken into account for the PM subdomains. The following notations is adopted in the following section for the sake of clarity:

$$\begin{aligned} P_w(u,v) &= \left(\frac{u}{v}\right)^w + \left(\frac{v}{u}\right)^w \\ E_w(u,v) &= \left(\frac{u}{v}\right)^w - \left(\frac{v}{u}\right)^w \end{aligned}. \tag{B.2}$$

B.2 Inner and outer PM Subdomains (Region I and V)

For the PM subdomains, reference is made to the Poisson's equation:

$$\frac{\partial^2 A_{I,V}}{\partial r^2} + \frac{1}{r}\frac{\partial A_{I,V}}{\partial r} + \frac{1}{r^2}\frac{\partial^2 A_{I,V}}{\partial \theta^2} = \frac{\mu_0}{r}\frac{\partial M_r^{I,V}}{\partial \theta} \tag{B.3}$$

where μ_0 is the permeability of vacuum and M_r is the PM radial magnetization. The latter can be further expressed as a Fourier series:

$$M_r^{I,V}=\sum_{n=1}^{+\infty} M_n^{I,V}\, sin\left(n\left(\theta-\varphi_{i,o}\right)\right)$$
$$M_n^{I,V}=\frac{4B_r p_{i,o}}{n\pi\mu_0},\ n=\left(2m-1\right)p_{i,o},\qquad m=1..+\infty \tag{B.4}$$

in which n represents the harmonic order and $\varphi_{i,o}$ is the angular displacement of the PM inner/outer polar axis referred to the reference position, as shown in Figure III.5. Furthermore, B_r is the residual magnetic flux density of the PMs and $p_{i,o}$ is the number of inner/outer rotor pole pairs.

Additionally, the following boundary conditions are considered:

$$\left.\frac{\partial A_I}{\partial r}\right|_{r=R1}=0,\ \left.\frac{\partial A_V}{\partial r}\right|_{r=R6}=0$$
$$A_I(R_2,0)=A_{II}(R_2,0),\ A_{IV}(R_5,0)=A_V(R_5,0) \tag{B.5}$$

According to the superposition law, the general solution of (B.3) is the sum of the general solution and of a particular solution, as pointed out in the following:

$$A_{I,V}\left(r,\theta\right)=\sum_{n=1}^{\infty}\left(A^{I,V}{}_n\frac{P_n\left(r,R_{1,5}\right)}{P_n\left(R_{2,6},R_{1,5}\right)}+X_{n\_i,o}\left(r\right)\cos\left(n\varphi_{i,o}\right)\right)\cos\left(n\theta\right)+$$
$$+\sum_{n=1}^{\infty}\left(C^{I,V}{}_n\frac{P_n\left(r,R_{1,5}\right)}{P_n\left(R_{2,6},R_{1,5}\right)}+X_{n\_i,o}\left(r\right)\sin\left(n\varphi_{i,o}\right)\right)\sin\left(n\theta\right) \tag{B.6}$$

where

$$X_{n\_i,o}\left(r\right)=\left(1+\frac{1}{n}\left(\frac{R_{1,5}}{r}\right)^{n+1}\right)\cdot f_{n\_i,o}\left(r\right)+$$
$$-\frac{P_n\left(r,R_{1,5}\right)}{P_n\left(R_{2,6},R_{1,5}\right)}\cdot\left(1+\frac{1}{n}\left(\frac{R_{1,5}}{r}\right)^{n+1}\right)\cdot f_{n\_i,o}\left(R_{2,6}\right) \tag{B.7}$$

$$f_{n\_i,o}\left(r\right)=\begin{cases}\dfrac{4B_r\cdot p_{i,o}}{\pi\left(1-n^2\right)}r\cdot\cos\left(\dfrac{n\pi}{2p}\left(1-\alpha_{i,o}\right)\right) & \text{if}\quad n=jp_{i,o}\quad j=1,3,5,...\\ \dfrac{2B_r}{\pi}r\ln r\cdot\cos\left(\dfrac{\pi}{2}\left(1-\alpha_{i,o}\right)\right) & \text{if}\quad n=p_{i,o}=1\\ 0 & \text{otherwise}\end{cases} \tag{B.8}$$

Considering both (B.7) and (B.8), n is a positive integer, $\alpha_{i,o}$ is the pole arc to pole pitch ratio of the inner and outer PM rotor, respectively. Furthermore, the coefficients $A^{I,IV}{}_n$ and $C^{I,IV}{}_n$ are determined by a Fourier series expansion of $A_{II,IV}(R_{2,5},\ \theta)$ within the interval [0, 2π]:

$$\begin{aligned} A^{I,V}{}_n &= \frac{1}{\pi}\int_0^{2\pi} A_{II,IV}\left(R_{2,5},\theta\right)\cdot\cos\left(n\theta\right)\cdot d\theta \\ C^{I,V}{}_n &= \frac{1}{\pi}\int_0^{2\pi} A_{II,IV}\left(R_{2,5},\theta\right)\cdot\sin\left(n\theta\right)\cdot d\theta \end{aligned}. \tag{B.9}$$

B.3 *Inner and outer air gap subdomains (Region II and IV)*

For the air gap subdomains, the magnetic potential vector can be computed by using the Laplace's equation:

$$\frac{\partial^2 A_{II,IV}}{\partial r^2}+\frac{1}{r}\frac{\partial A_{II,IV}}{\partial r}+\frac{1}{r^2}\frac{\partial^2 A_{II,IV}}{\partial \theta^2}=0. \tag{B.10}$$

For these subdomains the continuity of the tangential component of the magnetic field is taken into account:

$$\left.\frac{\partial A_{II}}{\partial r}\right|_{r=R_2}=\left.\frac{\partial A_{I}}{\partial r}\right|_{r=R_2},\quad \left.\frac{\partial A_{IV}}{\partial r}\right|_{r=R_5}=\left.\frac{\partial A_{V}}{\partial r}\right|_{r=R_5}. \tag{B.11}$$

In addition, the following boundary conditions are considered:

$$\left.\frac{\partial A_{II}}{\partial r}\right|_{r=R_3}=f_i\left(\theta\right),\quad \left.\frac{\partial A_{IV}}{\partial r}\right|_{r=R_4}=f_o\left(\theta\right) \tag{B.12}$$

in which:

$$f_{i,o}\left(\theta\right)=\begin{cases} \left.\dfrac{\partial A_{III\_j}}{\partial r}\right|_{r=R_{3,4}} & \forall\theta\in\left[\theta_j,\theta_j+\beta\right] \\ 0 & \text{elsewhere} \end{cases}. \tag{B.13}$$

Considering (B.13), $A_{III\_j}(r,\theta)$ is the magnetic potential vector in the j-th slot and θ_j is the angular position of the j-th slot, which is defined by:

$$\theta_j = -\frac{\beta}{2} + \frac{2j\pi}{Q} + \theta_0 \quad \text{with } 1 \le j \le Q \tag{B.14}$$

where θ_0 is the initial angular position of the pole-pieces ring, β is the slot opening angle and Q the number of slots.

The general solution of (B.10) is obtained by the Sturm-Liouville problem in an ring and it can be written as:

$$\begin{aligned}
&A_{II,IV}(r,\theta) = A^{II,IV}{}_0 + \\
&\sum_{n=1}^{\infty}\left(A^{II,IV}{}_n \frac{R_{2,4}}{n} \frac{P_n(r,R_{3,5})}{E_n(R_{2,4},R_{3,5})} + B^{II,IV}{}_n \frac{R_{3,5}}{n} \frac{P_n(r,R_{2,4})}{E_n(R_{3,5},R_{2,4})} \right)\cos(n\theta) + . \\
&+\sum_{n=1}^{\infty}\left(C^{II,IV}{}_n \frac{R_{2,4}}{n} \frac{P_n(r,R_{3,5})}{E_n(R_{2,4},R_{3,5})} + D^{II,IV}{}_n \frac{R_{3,5}}{n} \frac{P_n(r,R_{2,4})}{E_n(R_{3,5},R_{2,4})} \right)\sin(n\theta)
\end{aligned} \tag{B.15}$$

Furthermore, the coefficient $A^{II,IV}{}_n$, $B^{II,IV}{}_n$, $C^{II,IV}{}_n$ and $D^{II,IV}{}_n$ are determined by a Fourier series expansion of $A_{I,V}(R_{2,5}, \theta)$ and $f_{i,o}(\theta)$ within the interval [0, 2π]:

$$\begin{aligned}
A^{II,IV}{}_n &= \frac{1}{\pi}\int_0^{2\pi} \left.\frac{\partial A_{I,IV}}{\partial r}\right|_{R_{2,5}} \cdot \cos(n\theta)\cdot d\theta \\
B^{II,IV}{}_n &= \frac{1}{\pi}\int_0^{2\pi} f_{i,o}(\theta)\cdot \cos(n\theta)\cdot d\theta \\
C^{II,IV}{}_n &= \frac{1}{\pi}\int_0^{2\pi} \left.\frac{\partial A_{I,IV}}{\partial r}\right|_{R_{2,5}} \cdot \sin(n\theta)\cdot d\theta \\
D^{II,IV}{}_n &= \frac{1}{\pi}\int_0^{2\pi} f_{i,o}(\theta)\cdot \sin(n\theta)\cdot d\theta
\end{aligned} . \tag{B.16}$$

B.4 The i-th slot subdomain (Region III_j)

For the j-th slot subdomain the problem of finding the magnetic vector potential distribution can be solved using the Laplace's equation:

$$\frac{\partial^2 A_{III\_j}}{\partial r^2} + \frac{1}{r}\frac{\partial A_{III\_j}}{\partial r} + \frac{1}{r^2}\frac{\partial^2 A_{III\_j}}{\partial \theta^2} = 0 . \tag{B.17}$$

For this subdomain, the continuity of the radial component of the magnetic flux density between the j-th slot and the air gap subdomains is taken into account:

$$
\begin{aligned}
A_{III\_j}\left(R_3,\theta\right) &= A_{II}\left(R_3,\theta\right) \\
A_{III\_j}\left(R_4,\theta\right) &= A_{IV}\left(R_4,\theta\right)
\end{aligned}
. \tag{B.18}
$$

In addition, the following boundary condition is considered:

$$
\left.\frac{\partial A_{III\_j}}{\partial r}\right|_{\theta=\theta_j} = 0 \ , \ \left.\frac{\partial A_{III\_j}}{\partial r}\right|_{\theta=\theta_j+\beta} = 0 \, . \tag{B.19}
$$

According to the superposition law, the general solution of (B.17) can be written as:

$$
\begin{aligned}
A_{III\_j} &= A^{III\_j}{}_0 + B^{III\_j}{}_0 \ln r + \\
&+ \sum_{k=1}^{\infty}\left(A^{III\_j}{}_0 \frac{E_{k\pi/\beta}\left(r,R_4\right)}{E_{k\pi/\beta}\left(R_3,R_4\right)} - B^{III\_j}{}_0 \frac{E_{k\pi/\beta}\left(r,R_4\right)}{E_{k\pi/\beta}\left(R_3,R_4\right)} \right)\cdot \cos\left(\frac{k\pi}{\beta}\left(\theta-\theta_j\right)\right)
\end{aligned}
\tag{B.20}
$$

in which k is a positive coefficient, while the coefficients $A^{III\_j}{}_0$, $B^{III\_j}{}_0$, $A^{III\_j}{}_k$, and $B^{III\_j}{}_k$ are determined referring to a Fourier series expansion of $A_{II}(R_3, \theta)$ and $A_{IV}(R_4, \theta)$ within the interval $[\theta_j, \theta_j+\beta]$:

$$
\begin{aligned}
A^{III\_j}{}_0 + B^{III\_j}{}_0 \ln R_3 &= \frac{1}{\beta}\int_0^{\theta_i+\beta} A_{II}\left(R_3,\theta\right)\cdot d\theta \\
A^{III\_j}{}_0 + B^{III\_j}{}_0 \ln R_4 &= \frac{1}{\beta}\int_0^{\theta_i+\beta} A_{IV}\left(R_4,\theta\right)\cdot d\theta \\
A^{III\_j}{}_k &= \frac{2}{\beta}\int_0^{\theta_i+\beta} A_{II}\left(R_3,\theta\right)\cos\left(\frac{k\pi}{\beta}\left(\theta-\theta_j\right)\right)\cdot d\theta \\
B^{III\_j}{}_k &= \frac{2}{\beta}\int_0^{\theta_i+\beta} A_{IV}\left(R_4,\theta\right)\cos\left(\frac{k\pi}{\beta}\left(\theta-\theta_j\right)\right)\cdot d\theta
\end{aligned}
. \tag{B.21}
$$

References

[1] A. Emadi, *Advanced Electric Drive Vehicles*, 1 edition. CRC Press, 2014.

[2] G. Pellegrino, A. Vagati, P. Guglielmi, and B. Boazzo, 'Performance Comparison Between Surface-Mounted and Interior PM Motor Drives for Electric Vehicle Application', *IEEE Trans. Ind. Electron.*, vol. 59, no. 2, pp. 803–811, Feb. 2012, doi: 10.1109/TIE.2011.2151825.

[3] M. S. R. Mousavi, A. Pakniyat, and B. Boulet, 'Dynamic modeling and controller design for a seamless two-speed transmission for electric vehicles', in *in Proc. of IEEE Conference on Control Applications (CCA 2014)*, Nice (France), 2014, pp. 635–640, doi: 10.1109/CCA.2014.6981411.

[4] T. Hofman and C. H. Dai, 'Energy efficiency analysis and comparison of transmission technologies for an electric vehicle', in *Proc. of IEEE Vehicle Power and Propulsion Conference (VPPC 2010)*, Lille (France), 2010, pp. 1–6, doi: 10.1109/VPPC.2010.5729082.

[5] Q. Ren, D. A. Crolla, and A. Morris, 'Effect of transmission design on Electric Vehicle (EV) performance', in *Proc. of IEEE Vehicle Power and Propulsion Conference (VPPC 2009)*, Dearborn (USA), 2009, pp. 1260–1265, doi: 10.1109/VPPC.2009.5289707.

[6] J. de Santiago *et al.*, 'Electrical Motor Drivelines in Commercial All-Electric Vehicles: A Review', *IEEE Trans. Veh. Technol.*, vol. 61, no. 2, pp. 475–484, Feb. 2012, doi: 10.1109/TVT.2011.2177873.

[7] M. Ehsani, Y. Gao, and A. Emadi, *Modern Electric, Hybrid Electric, and Fuel Cell Vehicles: Fundamentals, Theory, and Design, Second Edition*, 2 edizione. Boca Raton: CRC Press, 2009.

[8] D. Gunji and H. Fujimoto, ‘Efficiency analysis of powertrain with toroidal continuously variable transmission for Electric Vehicles’, in *Proc. of 39th Annual Conference of the IEEE Industrial Electronics Society (IECON 2013)*, 2013, pp. 6614–6619, doi: 10.1109/IECON.2013.6700226.

[9] X. Li, M. Cheng, K. T. Chau, and W. Hua, ‘Comparison of magnetic-geared permanent-magnet machines’, *Prog. Electromagn. Res.*, vol. 133, pp. 177–198, Oct. 2012.

[10] D. Fodorean, ‘Study of a High-Speed Motorization With Improved Performances Dedicated for an Electric Vehicle’, *IEEE Trans. Magn.*, vol. 50, no. 2, pp. 921–924, Feb. 2014, doi: 10.1109/TMAG.2013.2279240.

[11] K. H. Kim, H. I. Park, S. M. Jang, and J. Y. Choi, ‘Comparison of Characteristics of Double-Sided Permanent-Magnet Synchronous Motor/Generator According to Magnetization Patterns for Flywheel Energy Storage System Using an Analytical Method’, *IEEE Trans. Magn.*, vol. 51, no. 3, pp. 1–4, Mar. 2015, doi: 10.1109/TMAG.2014.2358791.

[12] F. Martin, A. Belahcen, and M. E. H. Zaïm, ‘Effect of magnet materials on optimal design of a high speed PMSM’, in *Proc. of 18th International Conference on Electrical Machines and Systems (ICEMS 2015)*, Pattaya (Thailand), 2015, pp. 661–667, doi: 10.1109/ICEMS.2015.7385117.

[13] D. Fodorean, *State of the Art of Magnetic Gears, their Design, and Characteristics with Respect to EV Application*. InTech, 2016.

[14] A. Damiano, A. Floris, I. Marongiu, M. Porru, and A. Serpi, ‘Efficiency assessment of Electric Propulsion Systems for electric vehicles’, in *2016 International Symposium on Power Electronics, Electrical Drives, Automation and Motion (SPEEDAM)*, 2016, pp. 1232–1237, doi: 10.1109/SPEEDAM.2016.7525934.

[15] A. Damiano, A. Floris, G. Fois, I. Marongiu, M. Porru, and A. Serpi, ‘Design of a High-Speed ferrite-based Brushless DC Machine for electric vehicles’, in *2016 XXII International Conference on Electrical Machines (ICEM)*, 2016, pp. 715–721, doi: 10.1109/ICELMACH.2016.7732605.

[16] D. J. Evans and Z. Q. Zhu, ‘Influence of design parameters on magnetic gear’s torque capability’, in *Proc. of IEEE International Electric Machines Drives Conference (IEMDC 2011)*, Niagara Falls (Canada), 2011, pp. 1403–1408, doi: 10.1109/IEMDC.2011.5994813.

[17] M. G. Tehrani, J. Kelkka, J. Sopanen, A. Mikkola, and K. Kerkkanen, ‘Transmission configuration effect on total efficiency of Electric Vehicle powertrain’, in *2014 16th European Conference on Power Electronics and Applications (EPE’14-ECCE Europe)*, 2014, pp. 1–9, doi: 10.1109/EPE.2014.6910780.

[18] N. E. Anderson and S. H. Loewenthal, ‘Effect of Geometry and Operating Conditions on Spur Gear System Power Loss’, *J. Mech. Des.*, vol. 103, no. 1, pp. 151–159, Jan. 1981, doi: 10.1115/1.3254854.

[19] F. Concellón, P. J, and S. Baselga Ariño, ‘Analysis of power losses on spur gears using the design of experiments theory’, *Rev. Fac. Ing. Univ. Antioquia*, no. 72, pp. 203–216, Sep. 2014.

[20] X. Zhang and C. Mi, *Vehicle Power Management*. London: Springer London, 2011.

[21] A. Nair and K. R. Rajagopal, ‘Generic model of an electric vehicle for dynamic simulation and performance prediction’, in *in Proc. of International Conference on Electrical Machines and Systems (ICEMS 2010)*, Songdo Convensia Incheon (South Korea), 2010, pp. 753–757.

[22] R. R. Moghaddam, ‘High speed operation of electrical machines, a review on technology, benefits and challenges’, in *Proc. of IEEE Energy Conversion Congress and Exposition (ECCE 2014)*, Pittsburgh (USA), 2014, pp. 5539–5546, doi: 10.1109/ECCE.2014.6954160.

[23] W. Gengji, Q. Qinglei, W. Ping, and W. Xiaoyuan, ‘Analysis of the rotor loss in a high speed permanent magnet motor for flywheel energy storage system’, in *Proc. of 18th International Conference on Electrical Machines and Systems (ICEMS 2015)*, Pattaya (Thailand), 2015, pp. 2040–2044, doi: 10.1109/ICEMS.2015.7385376.

[24] Z. Kolondzovski, A. Arkkio, J. Larjola, and P. Sallinen, ‘Power Limits of High-Speed Permanent-Magnet Electrical Machines for Compressor Applications’, *IEEE Trans. Energy Convers.*, vol. 26, no. 1, pp. 73–82, Mar. 2011, doi: 10.1109/TEC.2010.2089459.

[25] N. Bianchi, S. Bolognani, and F. Luise, ‘Potentials and limits of high-speed PM motors’, *IEEE Trans. Ind. Appl.*, vol. 40, no. 6, pp. 1570–1578, Nov. 2004, doi: 10.1109/TIA.2004.836173.

[26] C. Zwyssig, M. Duerr, D. Hassler, and J. W. Kolar, ‘An Ultra-High-Speed, 500000 rpm, 1 kW Electrical Drive System’, in *2007 Power Conversion Conference - Nagoya*, 2007, pp. 1577–1583, doi: 10.1109/PCCON.2007.373174.

[27] C. Zwyssig, J. W. Kolar, W. Thaler, and M. Vohrer, ‘Design of a 100 W, 500000 rpm permanent-magnet generator for mesoscale gas turbines’, in *Fourtieth IAS Annual Meeting. Conference Record of the 2005 Industry Applications Conference, 2005.*, Hong Kong, China, 2005, vol. 1, pp. 253–260, doi: 10.1109/IAS.2005.1518318.

[28] T. Noguchi and M. Kano, ‘Development of 150000 r/min, 1.5 kW Permanent-Magnet Motor for Automotive Supercharger’, in *2007 7th International Conference*

on Power Electronics and Drive Systems, 2007, pp. 183–188, doi: 10.1109/PEDS.2007.4487698.

[29] A. Tenconi, S. Vaschetto, and A. Vigliani, 'Electrical Machines for High-Speed Applications: Design Considerations and Tradeoffs', *IEEE Trans. Ind. Electron.*, vol. 61, no. 6, pp. 3022–3029, Jun. 2014, doi: 10.1109/TIE.2013.2276769.

[30] A. Rezzoug and M. E.-H. Zaim, Eds., *Non-conventional Electrical Machines*, 1 edition. Wiley-ISTE, 2013.

[31] A. Binder, T. Schneider, and M. Klohr, 'Fixation of buried and surface-mounted magnets in high-speed permanent-magnet synchronous machines', *IEEE Trans. Ind. Appl.*, vol. 42, no. 4, pp. 1031–1037, Jul. 2006, doi: 10.1109/TIA.2006.876072.

[32] W. Zhong, S. Song, G. Chen, X. Huang, and P. Huang, 'Stress field of orthotropic cylinder subjected to axial compression', *Appl. Math. Mech.*, vol. 31, no. 3, pp. 305–316, Mar. 2010, doi: 10.1007/s10483-010-0304-z.

[33] F. Zhang, G. Du, T. Wang, G. Liu, and W. Cao, 'Rotor Retaining Sleeve Design for a 1.12-MW High-Speed PM Machine', *IEEE Trans. Ind. Appl.*, vol. 51, no. 5, pp. 3675–3685, Sep. 2015, doi: 10.1109/TIA.2015.2423659.

[34] D. Gerada, A. Mebarki, N. L. Brown, C. Gerada, A. Cavagnino, and A. Boglietti, 'High-Speed Electrical Machines: Technologies, Trends, and Developments', *IEEE Trans. Ind. Electron.*, vol. 61, no. 6, pp. 2946–2959, Jun. 2014, doi: 10.1109/TIE.2013.2286777.

[35] M. Kimiabeigi *et al.*, 'High-Performance Low-Cost Electric Motor for Electric Vehicles Using Ferrite Magnets', *IEEE Trans. Ind. Electron.*, vol. 63, no. 1, pp. 113–122, Jan. 2016, doi: 10.1109/TIE.2015.2472517.

[36] I. Boldea, L. N. Tutelea, L. Parsa, and D. Dorrell, 'Automotive Electric Propulsion Systems With Reduced or No Permanent Magnets: An Overview', *IEEE Trans. Ind. Electron.*, vol. 61, no. 10, pp. 5696–5711, Oct. 2014, doi: 10.1109/TIE.2014.2301754.

[37] Tianyu Wang, Fengxiang Wang, Haoran Bai, and Junqiang Xing, 'Optimization design of rotor structure for high speed permanent magnet machines', in *2007 International Conference on Electrical Machines and Systems (ICEMS)*, 2007, pp. 1438–1442.

[38] R. C. Juvinall and K. M. Marshek, *Fundamentals of Machine Component Design*, 5 Har/Psc edizione. Hoboken, NJ: John Wiley & Sons Inc, 2011.

[39] P. Moreno-Torres, M. Lafoz, M. Blanco, and J. R.Arribas, 'Passenger Exposure to Magnetic Fields in Electric Vehicles', in *Modeling and Simulation for Electric Vehicle Applications*, InTech, 2016, pp. 47–71.

[40] U.S. Department of Energy (DOE), 'Vehicle Technologies Office: 2015 Electric Drive Technologies Annual R&D Progress Report | Department of Energy', 2015.
[41] 'Cogent Power - Part of the Tata Steel Group'. [Online]. Available: https://cogent-power.com/. [Accessed: 12-Dec-2019].
[42] 'Eclipse Magnetics | Work Smart With Magnets'. [Online]. Available: https://landbot.io/u/H-198514-UGQMII5C2SZYLGPC/index.html. [Accessed: 12-Dec-2019].
[43] G. Gatto, I. Marongiu, A. Perfetto, and A. Serpi, 'Three-Phase Operation of Brushless DC Motor Drive Controlled by a Predictive Algorithm', in *IECON 2006 - 32nd Annual Conference on IEEE Industrial Electronics*, 2006, pp. 1166–1170, doi: 10.1109/IECON.2006.347565.
[44] N. Niguchi and K. Hirata, 'Cogging Torque Analysis of Magnetic Gear', *IEEE Trans. Ind. Electron.*, vol. 59, no. 5, pp. 2189–2197, May 2012, doi: 10.1109/TIE.2011.2159357.
[45] K. Atallah, S. D. Calverley, and D. Howe, 'Design, analysis and realisation of a high-performance magnetic gear', *IEE Proc. - Electr. Power Appl.*, vol. 151, no. 2, pp. 135–143, Mar. 2004, doi: 10.1049/ip-epa:20040224.
[46] A. Rotondale, M. Villani, and L. Castellini, 'Analysis of high-performance magnetic gears for electric vehicle', in *2014 IEEE International Electric Vehicle Conference (IEVC)*, 2014, pp. 1–6, doi: 10.1109/IEVC.2014.7056165.
[47] P. M. Tlali, R. J. Wang, and S. Gerber, 'Magnetic gear technologies: A review', in *2014 International Conference on Electrical Machines (ICEM)*, 2014, pp. 544–550, doi: 10.1109/ICELMACH.2014.6960233.
[48] S. Gerber, 'Evaluation and design aspects of magnetic gears and magnetically geared electrical machines', Thesis, Stellenbosch : Stellenbosch University, 2015.
[49] A. A. Faysal and S. M. Haris, 'Development of Magnetic Gears: A Review', p. 8.
[50] Y. Wang, M. Filippini, N. Bianchi, and P. Alotto, 'A Review on Magnetic Gears: Topologies, Computational Models, and Design Aspects', *IEEE Trans. Ind. Appl.*, vol. 55, no. 5, pp. 4557–4566, Sep. 2019, doi: 10.1109/TIA.2019.2916765.
[51] F. T. Jorgensen, *Design and Construction of Permanent Magnetic Gears*. Institute of Energy Technology, Aalborg University, 2010.
[52] K. T. Chau, *Electric Vehicle Machines and Drives: Design, Analysis and Application*. Singapore: John Wiley & Sons, Singapore Pte. Ltd, 2015.
[53] K. Atallah and D. Howe, 'A novel high-performance magnetic gear', *IEEE Trans. Magn.*, vol. 37, no. 4, pp. 2844–2846, Jul. 2001, doi: 10.1109/20.951324.

[54] T. Lubin, S. Mezani, and A. Rezzoug, 'Analytical Computation of the Magnetic Field Distribution in a Magnetic Gear', *IEEE Trans. Magn.*, vol. 46, no. 7, pp. 2611–2621, Jul. 2010, doi: 10.1109/TMAG.2010.2044187.

[55] B. McGilton, R. Crozier, A. McDonald, and M. Mueller, 'Review of magnetic gear technologies and their applications in marine energy', *IET Renew. Power Gener.*, vol. 12, no. 2, pp. 174–181, Feb. 2018, doi: 10.1049/iet-rpg.2017.0210.

[56] T. Lubin, S. Mezani, and A. Rezzoug, 'Experimental and Theoretical Analysis of Axial Magnetic Coupling under Steady-State and Transient Operation', p. 11.

[57] T. Lubin, S. Mezani, and A. Rezzoug, 'Exact Analytical Method for Magnetic Field Computation in the Air Gap of Cylindrical Electrical Machines Considering Slotting Effects', *IEEE Trans. Magn.*, vol. 46, no. 4, pp. 1092–1099, Apr. 2010, doi: 10.1109/TMAG.2009.2036257.

[58] X. Zhang, X. Liu, C. Wang, and Z. Chen, 'Analysis and Design Optimization of a Coaxial Surface-Mounted Permanent-Magnet Magnetic Gear', *Energies*, vol. 7, no. 12, pp. 8535–8553, Dec. 2014, doi: 10.3390/en7128535.

[59] M. Filippini and P. Alotto, 'Coaxial Magnetic Gear Design and Optimization', *IEEE Trans. Ind. Electron.*, vol. 64, pp. 9934–9942, 2017, doi: 10.1109/TIE.2017.2721918.

[60] K. Venkatachalam, C. R. Sullivan, T. Abdallah, and H. Tacca, 'Accurate prediction of ferrite core loss with nonsinusoidal waveforms using only Steinmetz parameters', in *2002 IEEE Workshop on Computers in Power Electronics, 2002. Proceedings.*, Mayaguez, Puerto Rico, 2002, pp. 36–41, doi: 10.1109/CIPE.2002.1196712.

[61] A. Serpi, G. Fois, M. Porru, A. Damiano, and D. Loi, 'Flux-Weakening Space Vector Control Algorithm for Permanent Magnet Brushless DC Machines', 2018, doi: 10.1109/VPPC.2018.8604971.

[62] A. Serpi, M. Porru, G. Fois, and A. Damiano, 'Design of Flux-Weakening Space Vector Control Algorithms for Permanent Magnet Brushless DC Machines on Suitable Synchronous Reference Frames', *IET Electr. Syst. Transp.*, vol. 9, Sep. 2019, doi: 10.1049/iet-est.2018.5108.

[63] A. Serpi, G. Fois, M. Porru, A. Damiano, and I. Marongiu, 'Space vector control of permanent Magnet Brushless DC Machines', in *2016 XXII International Conference on Electrical Machines (ICEM)*, 2016, pp. 1194–1200, doi: 10.1109/ICELMACH.2016.7732676.

[64] R. Krishnan, *Permanent Magnet Synchronous and Brushless DC Motor Drives*. New York: CRC Press, 2010.

[65] R. G. Budynas, *Advanced Strength and Applied Stress Analysis*, 2 edizione. Boston: McGraw-Hill Higher Education, 1998.

Publications

- Damiano, A. Floris, G. Fois, M. Porru, and A. Serpi, ‘*Modelling and design of PM retention sleeves for High-Speed PM Synchronous Machines*’, in 2016 6th International Electric Drives Production Conference (EDPC), 2016.
- M. Porru, A. Serpi, A. Floris, and A. Damiano, ‘*Modelling and real-time simulations of electric propulsion systems*’, in 2016 International Conference on Electrical Systems for Aircraft, Railway, Ship Propulsion and Road Vehicles International Transportation Electrification Conference (ESARS-ITEC), 2016.
- A. Damiano, A. Floris, G. Fois, I. Marongiu, M. Porru, and A. Serpi, ‘*Design of a High-Speed Ferrite-Based Brushless DC Machine for Electric Vehicles*’, IEEE Trans. Ind. Appl., vol. 53, no. 5, pp. 4279–4287, Sep. 2017, doi: 10.1109/TIA.2017.2699164.
- G. Fois, A. Floris, A. Serpi, M. Porru, and A. Damiano, ‘*Design Criteria for Ferrite-Based High-Speed Permanent Magnet Synchronous Machines*’, in Proc. of 7th International Electric Drives Production Conference (EDPC 2017), Wurzburg (Germany), 2017.
- Floris, A. Serpi, M. Porru, G. Fois, and A. Damiano, ‘*Design of a Double-Stage Magnetic Gear for High-Speed Electric Propulsion Systems*’, in 2018 XIII International Conference on Electrical Machines (ICEM), 2018.
- Floris, A. Serpi, M. Porru, and A. Damiano, ‘*A Comparative Analysis of Different Double-Stage Magnetic Gear Transmission Systems with High Gear Ratio*’, in Proc. of 8th International Electric Drives Production Conference (EDPC 2018), Schweinfurt (Germany), 2018.
- A.Floris, A. Serpi, A. Damiano, I. Hahn, “*Torque Harmonics Minimization of Double-Stage Magnetic Gear Transmission System*,” in Proc. of 45th Annual Conference on IEEE Industrial Electronics (IECON 2019), 2019.